First Pass Pharmacokinetic Modelling in Dynamic Contrast-Enhanced Magnetic Resonance Imaging : Application in Human Oncology

A thesis submitted to the University of Manchester for the degree of

Doctor of Philosophy (PhD)

in the Faculty of Medicine, Dentistry, Nursing and Pharmacy

2004

HAMIED AHMAD HAROON

Division of Imaging Science and Biomedical Engineering

CONTENTS

LIST OF FIGURES AND TABLES

ABSTRACT

We present the technical aspects of a First Pass Leakage Profile pharmacokinetic model (denoted FP) applied to the analysis of T_1-weighted dynamic contrast-enhanced (DCE) magnetic resonance imaging (MRI) data, for the characterisation of vasculature in human tumours. This has major implications for the investigation of angiogenesis, tumour growth and the development of therapeutic agents. The FP model was originally proposed by Li et al. in 2000 and uses time course data during the first passage of a bolus of contrast agent to provide its estimate of the trans-endothelial transfer constant K^{trans} – denoted K_{fp} – and (cerebral) blood volume – denoted CBV_{T_1} or BV_{T_1}.

In a group of 23 patients with cerebral gliomas we compared the estimates of K^{trans} between a modified version of a conventionally established pharmacokinetic model (yielding K_{TK}) and the FP method's K_{fp}. We found that K_{TK} and K_{fp} produce similar biologic information within voxels not dominated by vascular tissue. The FP method avoids erroneous overestimation of K^{trans} in areas of significant intravascular contrast. Findings are in keeping with previously published mathematical simulations.

In a larger cohort of 39 cerebral glioma patients we examined the relationship between K_{fp} and histopathological WHO grade (II, III and IV). Median values of $K_{fp,}$ CBV_{T_1} and of the 95th-centile (95%) of the distribution (K_{fp}(95%) and CBV_{T_1}(95%)) were calculated. Discriminant analysis showed an independent relationship between both CBV_{T_1} and K_{fp}(95%) and grade, and the canonical function produced a diagnostic sensitivity and specificity higher than 90%.

We compared parametric maps, measured tumour values and value distributions of CBV_{T_1} maps and conventional CBV maps from T_2*-weighted DCE data (CBV_{T_2*}) in patients with intraaxial tumours. Leakage-free CBV_{T_1} maps correlate well with conventionally generated CBV_{T_2*} maps, both in terms of median measurements from tumour tissue and visual distribution of blood vessels. CBV_{T_1} maps do not suffer from the susceptibility artefacts seen in CBV_{T_2*} maps and offer higher through plane spatial resolution.

We applied the FP method to a group of 14 patients with hepatic neoplasms. The FP method is unique in allowing breath-hold image acquisition because of the short time-course of DCE data it requires. Mapping of the arrival time (T_0) of contrast medium allowed identification of tissue supplied by the hepatic arteries and portal vein. Hepatic tumours all showed typical hepatic arterial enhancement. Repeated K_{fp} and BV_{T_1} maps in five patients showed excellent reproducibility.

Twenty patients with progressive solid tumours were treated with HuMV833, a humanised form of a mouse monoclonal anti-VEGF antibody, at various doses (0.3, 1, 3, or 10 mg/kg) in a phase I trial. As part of the trial DCE-MRI and the FP model were used to measure K_{fp}, which was strongly heterogeneous between and within patients and between and within individual tumours. All tumours showed a reduction in K_{fp} 48 hours after the first treatment.

We have shown that the FP method can provide accurate, reliable and reproducible information for the *in vivo* characterisation of vasculature in human tumours. The short acquisition required makes it ideal for routine clinical use. We recommend its further development to enable measurement of blood flow as an independent parameter.

DECLARATION

I hereby declare that no portion of the work referred to in this thesis has been submitted in support of an application for another degree or qualification of this or any other university or other institute of learning

COPYRIGHT STATEMENT

(1) Copyright in text of this thesis rests with the Author. Copies (by any process) either in full, or of extracts, may be made **only** in accordance with instructions given by the Author and lodged in the John Rylands University Library of Manchester. Details may be obtained from the Librarian. This page must form part of any such copies made. Further copies (by any process) of copies made in accordance with such instructions may not be made without the permission (in writing) of the Author.

(2) The ownership of any intellectual property rights which may be described in this thesis is vested in the University of Manchester, subject to any prior agreement to the contrary, and may not be made available for use by third parties without the written permission of the University, which will prescribe the terms and conditions of any such agreement.

(3) Further information on the conditions under which disclosures and exploitation may take place is available from the Head of the Division of Imaging Science and Biomedical Engineering.

بسم الله الرحمن الرحيم

IN THE NAME OF ALLAH, THE MOST GRACIOUS, THE EVER MERCIFUL

"Read: In the Name of thy Lord Who createth,
Createth man from a clot of blood.
Read: And thy Lord is the Most Bounteous,
Who teacheth by the pen,
Teacheth man that which he knew not."
[The Holy Qur'an, 96:1-5]

"… and say, "O my Lord! Advance me in knowledge."
[The Holy Qur'an, 20:114]

DEDICATIONS

WITH THE BLESSINGS OF ALLAH,
THE ALL-KNOWING, THE MOST WISE

I dedicate this thesis to my dearest and most beloved
parents,
the most precious of Almighty ALLAH's Gifts to me

"… and say, "O my Lord! Bestow on them Thy Mercy even as they cherished me in childhood."
[The Holy Qur'an, 17:24]

ACKNOWLEDGEMENTS

All Praises and Thanks belong to ALLAH, Lord of all the worlds.
May Salutations, Peace and the Blessings of ALLAH be upon His Noble Messenger, Muhammad, and upon his family and his companions, until the Day of Judgement.
May Peace be upon all the Messengers and Prophets of ALLAH and may His Pleasure and Mercy be upon all the people who follow them, until the end of Time.

I have so many people to thank. I'm sure I won't have mentioned everyone. My deepest thanks are expressed to all who have contributed to my time on my PhD programme.

My sincerest appreciation and gratitude go to my PhD supervisor, Professor Alan Jackson. I am indebted to him for all the support, understanding, patience and guidance he has given me over the past 5 years – I will never forget it. Prof Jackson's deep knowledge and experience of science, statistics and software programming, while being a radiologist by profession, makes him unique in the world. This is evident at conferences when I say that my supervisor is Prof Jackson people become very impressed. His kind recommendation earned me the offer of a job with Harvard Medical School's Beth Israel Deaconess Medical Centre. I have an enormous amount of respect and admiration for Prof Jackson, and I want to thank him for everything he did to allow me to begin my PhD programme and for everything he did for me since. I have enjoyed every meeting I have had with Prof Jackson and every project I have worked on with him. His enthusiasm and constructive advice has been a great source of encouragement and determination for me. Prof Jackson has afforded me so many opportunities to take part in cutting-edge research and to work with so many distinguished people and by this I have gained so much experience and acquaintances. In this way he has helped me to overcome all the physical impairments I have to achieve my best with my mind. I hope to have the opportunity to work with Prof Jackson again. I wish him continued success in the future and the happiness and joy of seeing his young children grow into great people.

My appreciation and gratitude also go to my second PhD supervisor, Professor Steve Williams. I am sincerely grateful to him for his support, especially when it came to finding funding for my PhD fees. Without his help I would not have been able to continue after my first year. I want to thank him for being available whenever I have needed his advice and for being a figure of encouragement at conferences.

I want to express my deepest thanks to Anne Russell, Prof Jackson's academic secretary, for the kindness and assistance she has shown me whenever I have approached her. Her efficiency and cheerful nature make everything seem so much better. Anne makes sure that Prof Jackson keeps running smoothly and is a great friend to all the people who work with him.

I want to say a big "Thank you" to my great friend Shelagh Stedman (*aka Nasti*), PA to Prof Williams, for all the moral support and encouragement she has given me over all these years. She has never let me feel any worse than anyone else. I'll never forget the pains she went through typing meeting notes for me. I wish her every happiness and good in her life.

I owe a big "Thank you" to my great friend Linda Foxley, Prof Jackson's clinical secretary, for all the assistance she has given me and for all the moral support and encouragement. Her kind and helpful nature have always been a source of strength for me.

Her sleeve-folding technique is second-to-none. I wish her every happiness and good in her life.

I would like to thank Angela Castledine, Christine Cummings, Brian Atherton, James Cleary, Zoe Lees, David Shaw, Chis Clapham, Debbie Fitton, Warren Mittoo, Ari Kuuka, Jermaine Gilmore, David Burke, David Ellard and Andy Yu for all their support and kindness.

People who have been my mentors include Dr Pawel Tokarczuk, Dr Tony Lacey, Dr David Buckley, Dr Neil Thacker, Dr Geoff Parker and Dr David Williamson to whom I am most grateful for all they taught me, for their time and their patience with me. I am particularly grateful to Geoff Parker for realising my potential and for offering me a job in ISBE, and for kindly allowing me the time to complete my PhD thesis.

My special thanks go to Yvon Watson, David Clark, Debbie Sinclair and Barry Whitnall, MR radiographers, for everything they taught me and for their patience with my demanding requests.

I would like to extend my appreciation to everybody else in ISBE, particularly my colleagues and friends, who have made my time so enjoyable. Also to those who came from abroad for a while to work with us, including my dear friend Dr Judith Harrer, and to those who I have know since I started my PhD, including my great friend Katherine Lymer.

I would like to thank all the distinguished people I have worked with, particularly Dr Gordon Jayson, Dr Peter Julyan, Dr Amit Herwadkar, Dr Scott Rutherford, Dr Graham Dow, Marietta Scott and Karl Embleton. I especially would like to show my gratitude to Professor Danielle Balériaux of Brussels, Belgium, and her colleagues, for visiting us and collaborating with us with such enthusiasm.

My special thanks go to Dr Tufail Patankar, Neuroradiologist, who I have worked with closely for most of my research projects, and from whom I have learnt so much. I wish him every success in his career and happiness and joy with his family.

I also extend a special thanks to Dr Xiaoping Zhu and Dr Kaloh Li for writing the analysis software I used and for answering all my queries with efficiency and diligence, even after moving to the USA.

I would like to extend a very sincere appreciation to the Snowdon Award Scheme and the University of Manchester Annual Fund for their kind generosity in covering my PhD programme fees. I must thank all the people who supported my application and granted me the awards. I'd like to thank the Faculty of Medicine, the Disability Support Office and the University of Manchester as a whole for all the facilities and support they have offered me to reach my goal.

I would like to take this opportunity to express my gratitude to Ron Brown for the many years he worked with me as my personal care assistant at the University and for all the great times we had together. I would also like to thank Ron's boss, Glyn Melling, for his friendship and continued encouragement, for accompanying me to all of my conferences abroad, for putting my needs above his own business and for all the great discussions we had.

All my brothers (in faith) at the Mosque have been a great source of spiritual strength for me, particularly Sheikh Habib, and my great friends Usman, Muhammad Tahar, Karim, Sarfraz, Ijaz, Mushtaq, Ehab Hamza, Muhammad Hammad, Hilal, Shaheer, Dr Ahmad, Khalid, Waleed, Ameen, Moeen, Sulayman, Mahmood, Mustafa, Mahir, Haitham, Noor, Anas and others whom I have not named. May ALLAH, The Most Holy and The Most Exalted, Bless them all with great success in all good things, in this life and more so in the Hereafter.

Last, but by no means the least, my heartfelt gratitude is due to my family without who's support I could not have got so far. May ALLAH, The Most High, Bless and Reward my dearest mother and father immensely, in this world and more so in the next, for their untiring support and encouragement and for everything they have done for me and continue to do for me. Their prayers have helped me to achieve so much. May Almighty ALLAH reward my brother Majeed and sisters Hajera and Fatema greatly for putting up with my mood swings and incessant demands on my parents' attention during the course of my studies. May ALLAH, The Most Exalted, Bless them always and Grant them the best of successes in their futures. We are all looking forward to the arrival of my beloved wife (in waiting), Humaira, from Pakistan in the near future, so that we can enjoy the anticipated celebration and our time ahead with her in our family. May ALLAH, The Most Kind, Bless her always and Grant her the best of rewards for her patience with me.

LIST OF ABBREVIATIONS

α	Flip angle for a Gradient Echo MRI sequence
CBV_{T_1}, CBV_{T1}, T_1-CBV, BV_{T_1}, BV_{T1}	CBV/BV estimate from (the FP method using) T_1-weighted DCE-MRI data
CBV_{T_2*}, CBV_{T2*}, T_2*-CBV	CBV estimate from T_2*-weighted DCE-MRI data
C, C(t)	Contrast concentration (at a time t)
CA	Contrast Agent
CBV, BV, rBV	(Relative) (cerebral) blood volume
C_e, $C_e(t)$	Contrast concentration in the EES (at a time t)
C_p, $C_p(t)$	Contrast concentration in plasma (at a time t)
CT	(X-ray) Computed Tomography
C_t, $C_t(t)$	Contrast concentration in tissue (at a time t)
DCE	Dynamic Contrast Enhanced
DRCE	Dynamic Relaxivity Contrast Enhanced
DSCE	Dynamic Susceptibility Contrast Enhanced
E	Initial extraction ratio
EES	Extravascular extracellular space
EF	Extraction-flow product
F, BF	Blood flow per unit mass of tissue
FLASH	Fast Low Angle Shot MRI sequence
FP	First Pass Leakage Profile pharmacokinetic method/model
Gd	Gadolinium
Gd-DTPA	Gadopentate dimeglumine (trade name Magnevist)
Gd-DTPA-BMA	Gadodiamide (trade name Omniscan)

IAUC	Initial Area Under Curve method
K_{fp}	K^{trans} from the FP method
K_{TK}	K^{trans} from the TK model
K^{trans}	Volume transfer constant between blood plasma and EES
MR	Magnetic Resonance
MRI	Magnetic Resonance Imaging
P	Total permeability of capillary wall
PET	Positron Emission Tomography
PS	Permeability-surface area product
r_1	T_1 relaxivity of water protons (dependent of factors including field strength, temperature and contrast agent)
R_1	Relaxation rate
R_{10}	Pre-contrast, baseline R_{10}
S	
S, S(t)	MR signal intensity (at a time t)
T_{10}	Pre-contrast, baseline T_1
TE	Echo time (MR sequence parameter)
TK	Tofts and Kermode’s pharmacokinetic model/method
TR	Repetition time (MR sequence parameter)
v_e	Volume of EES per unit volume of tissue
VEGF	Vascular Endothelial Growth Factor
v_p	Blood plasma volume per unit volume of tissue

PREFACE

Medical Physics is a field that I have wanted to make a career in since finding out about it in sixth-form physics class. My childhood ambition to enter the field of Medicine became an impractical option for me, so Medical Physics gave me an alternative route into Medicine as a scientist. By the Grace and Mercy of Almighty God, in retrospect I believe I have accomplished so much more in this field than I might have if I had become a physician.

I graduated with a BSc (Hons) in Physics from the University of Manchester Institute of Science and Technology (UMIST) in 1998. I then gained an MSc in Medical Physics in the Division of Imaging Science & Biomedical Engineering (ISBE) at the University of Manchester, and started my degree programme for a PhD here in 2000. Since the principles of Magnetic Resonance Imaging are based on pure physics it strikes me as the most exciting and versatile subject in Medical Physics offering the widest scope for novel developments. The expertise and facilities for advanced Magnetic Resonance technology in Manchester are amongst the best and well-renowned in the world.

It would be impossible for the work presented in the experimental Chapters of this Thesis to be that of a sole person. Each one required and involved multi-disciplinary collaboration, often on international scales. Collaborators included radiologists, oncologists, surgeons, pathologists, radiographers, physicists, computer scientists and software programmers. The software and MRI protocol that we have used in all of our studies was originally written, and is continually being developed, by Dr Xiaoping Zhu and Dr Kaloh Li. Dr Zhu and Dr Li proposed their technique when they were at our centre with Professor Alan Jackson, but in 2001 they moved to the University of California at San Francisco where they currently work.

I have gained so much experience and knowledge from all our work, which I have enjoyed thoroughly. My part in all these experimental studies has been

- organising data collection, including setting up our MR protocol at new sites
- communicating with collaborators
- receiving acquired MR data and patients' clinical information
- checking data for analysis suitability

- understanding the physics behind the physiological models we have used
- explaining the physiological modelling principles to clinicians
- modifying analysis code when necessary, especially to handle data in different formats
- obtaining radiologists' expertise to take measurements from specific pathologic, anatomic and vascular regions
- running analysis software on acquired data and generating parametric maps in the appropriate way
- showing clinicians how to run the analysis software to help them understand the practical aspects and so that they could eventually implement it independently in the clinic
- writing software to record measurements, statistics and histogram value-ranges from regions of interest
- carrying out mapping and graphical comparisons and statistical analysis on the parametric measurements to establish relationships
- understanding the meaning and significance of our findings
- presenting the results of our studies and writing papers for publication

The experimental Chapters have all been presented at scientific conferences around the world and either submitted or accepted for publication in major scientific journals in the field. Chapters 2 and 3 were presented in their preliminary stages at the International Society for Magnetic Resonance in Medicine (ISMRM) Scientific Meeting in Honolulu, Hawai'i, USA in May 2002 and then at the European Society for Magnetic Resonance in Medicine and Biology (ESMRMB) Annual Meeting in Cannes, France in August 2002. Chapter 4 was presented in its preliminary stages at the ESMRMB Annual Meeting in Rotterdam, The Netherlands in September 2003. The study that Chapter 6 is based on was presented at the American Society of Clinical Oncology (ASCO) in San Francisco, California, USA in May 2001, by Dr Gordon Jayson. Chapter 2 is a reproduction of a published paper (*J Magn Reson Imaging*, 2004; **19**(5):527-536) on which I am first author, Chapter 5 is a reproduction of a published paper (*NMR in Biomed*, 2002; **15**:164-173) on which I am second author to my supervisor and Chapter 6 is based on a major international, inter-disciplinary published paper (*J Natl Cancer Inst*, 2002; **94**(19):1484-1493). Chapters 3 and 4 have been submitted for publication but have not been accepted yet. Therefore all the Chapters in this Thesis appear as independent, publishable articles and repetition will be found between their Introduction and Materials & Methods sections.

The various parametric data gained from the same acquired patient datasets have been used in different aspects, from brain tumour patients, across Chapters 2-4, and from abdominal tumour patients, between Chapters 5 and 6. Most of the patient datasets used in Chapter 4 were acquired at our centre before I started on my PhD research programme and appear in published work (Zhu XP et al., *J Magn Reson Imaging*, 2000; **11**:575-585, and Li KL et al., *J Magn Reson Imaging*, 2000; **12**:347-357). Chapter 4's patient datasets have also been included in the patient datasets for Chapter 2, and Chapter 2's patient datasets have been included in the patient datasets for Chapter 3. The patient datasets used for the reproducibility study in Chapter 5 were from tumour patients who also took part in the antibody trial in Chapter 6. Grateful acknowledgement is made to all the patients (posthumously in some cases) who willingly participated in our research studies for the essential data they provided to address our questions.

I would like to take this opportunity to extend my gratitude to all my colleagues who contributed to the work presented in this Thesis. It has been a great privilege and pleasure to work with them all. I very much hope our work will have real, beneficial implications for Medicine in the near future.

HAMIED A HAROON
September 2004

CHAPTER 1 :

GENERAL INTRODUCTION

1.1 AIMS, OBJECTIVES AND STRUCTURE OF THIS THESIS

In the last 40 years it has been recognised that angiogenesis – the 'creation of new blood vessels' – plays a vital role in the growth of tumours [1-3]. There has therefore been a surge of novel anti-angiogenic treatment strategies undergoing clinical trial [4, 5]. Concomitant advances in non-invasive imaging and pharmacokinetic modelling have enabled the quantitative study of tumour vasculature, using the time course of intravascular contrast agent uptake to derive physiological parameters such as blood volume, microvascular endothelial permeability and blood flow [6, 7]. The ability to estimate these parameters offers a potential method for directly assessing the biological effectiveness of anti-angiogenic treatments in suppressing tumour growth *in vivo*. Magnetic resonance imaging (MRI) is a non-ionising imaging modality permitting repeated cross-sectional and volumetric contrast-enhanced imaging without the risks associated with radiation dosage [8], making it ideal for longitudinal studies in clinical trials.

The research presented in this Thesis deals with the technical aspects and application of pharmacokinetic modelling to the analysis of dynamic contrast-enhanced (DCE) MRI data for the characterisation of vasculature in human tumours. This is a complex and growing field, which has implications for the investigation of angiogenesis, tumour growth and the development of therapeutic agents. Specifically, the pharmacokinetic model we have concentrated our studies on is a First Pass Leakage Profile model (denoted as FP), which was proposed in 2000 by Li et al [9]. We have investigated the accuracy of this model in comparison to an established model, determined its value in assessing tumour grade in gliomas, studied its reproducibility and have included it as part of the clinical trial of a novel anti-angiogenic antibody. We have concentrated our DCE-MRI studies on:

1) brain tumours, particularly cerebral gliomas, for the first three experimental chapters; and
2) liver metastases, and abdominal and pelvic tumour deposits, for the last two

The introduction to this Thesis will give a very brief description of the brain and liver, and then give a brief overview of tumour biology and angiogenesis, concentrating on gliomas. The process of a clinical trial will also be briefly illustrated, so as to give some background to the part our study played in a clinical trial. These sections will be at a relatively superficial level as this suffices for understanding the biological aspects of this Thesis. The majority of this introduction will be a technical overview of dynamic contrast-enhanced MR imaging and pharmacokinetic models that have been proposed to analyse this data. The experimental chapters that follow will build on this technical background in detail.

The experimental chapters are presented as independent publishable papers and are as follows:

1. A Comparison of K^{trans} Measurements Obtained with Conventional and First Pass Pharmacokinetic Models in Human Gliomas
2. Is The Volume Transfer Coefficient (K_{fp}) Related to Histological Grade in Human Gliomas?
3. Comparison of Cerebral Blood Volume Maps Generated from T_2*- And T_1-Weighted MRI Data in Intra-Axial Cerebral Tumours

4. Breath-hold Perfusion and Permeability Mapping of Hepatic Malignancies using Magnetic Resonance Imaging and a First Pass Leakage Profile Model

5. Dynamic Contrast-Enhanced Magnetic Resonance Imaging in the Evaluation of HuMV833 Anti-VEGF Antibody

1.2 OVERVIEW OF ONCOLOGY

Neuro-oncology

The human brain is the centre of control and the most complex and powerful processing system amongst all living organisms. It is the most critical organ for vital physiological and sensory functions and adaptations. Being encased in the protective skull it is the most inaccessible organ of the human body and the most compromised in terms of acute volume changes. Although all sensations in the body are perceived by the brain, there is no mechanism for sensations in the brain itself. Therefore an obtrusive and potentially fatal object such as a tumour can go undetected for a substantial time, silently becoming more malignant as time progresses, until symptoms appear as the tumour interferes with important neuronal functions (such as vision, hearing or coordination). At the current time the management of malignant cerebral tumours particularly high grade gliomas is poor with a 50% survival less than 2 years. The development and application of new therapies demands concomitant development of improved imaging techniques to identify, characterise and grade tumours, non-invasively and *in vivo*. There is also a need for new techniques to classify tumours, to identify likely non-responders to specific therapies and to monitor the response to therapy at an early stage.

The Liver

The liver is the largest organ of the body, and is responsible for metabolism, digestion, detoxification and elimination of waste substances from the body. It has two major blood supplies: the hepatic artery, branching from the descending aorta, and the hepatic portal vein, carrying nutrients from the intestine. Through these blood supplies and the extensive lymphatic network through the liver, it is common for cancer to metastasise to the liver from almost every other organ in the body, such as colon cancer, breast cancer and ovarian cancer. Hepatic metastases are much more common than primary liver cancer or hepatocellular carcinoma.

1.2.1 Tumour Growth

Almost all cells in every tissue of the body replicate by the process of mitosis (cell division), to enable tissue growth and to replace old, dead or damaged cells. This is normally a well controlled and ordered process occurring throughout life. If the mechanisms of controlling cell division are interfered with, such as a defect in a cell's genetic code for reproduction, cells can start dividing and proliferating without any control or order and can develop into a tumour (see Figure 1.1) [10].

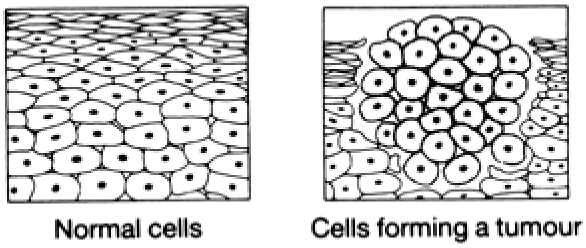

Figure 1.1. Diagram of normal cells and the formation of a tumour [10].

Tumours can be benign, remaining in the locality where they originated, generally not being life-threatening and can commonly be cured by resection. The growth of benign tumours can cause increasing pressure on surrounding tissue and therefore have adverse effects on physiology and/or function. Malignant tumours tend to be progressive, invading or infiltrating surrounding tissue and often metastasising to other organs. Severe morbidity and death are common. Tumour cells increasing in malignancy demonstrate reversion to primitive and dedifferentiated forms, known as anaplasia, becoming distinct from normal tissue [11].

1.2.2 Tumour Origins and Biology – concentrating on gliomas

Since tumours develop due to the breakdown of controlled cell division, they occur predominantly in tissues that normally undergo regular cell division.

Every human being is born with around 40 billion neurones making up their brain, which do not regenerate [11]. Thus it is rare to find nerve cells themselves becoming tumours. The nervous tissue of the brain is supported, nourished and protected by a network of glia (or neuroglia) cells (see Figure 1.2). There are different types of glial tissue including astrocytes (maintain K^+ balance), oligodendrocytes (produce myelin sheath), microglia (macrophages of the nervous system) and ependymal cells (ciliated and lining spaces in the brain) [11]. Glial cells do not conduct electrical impulses, providing insulation between neurones. Like most other cells of the body, these cells undergo regular cell division, growth and replacement. It is glial cells that most commonly transform into brain tumours known as gliomas [11].

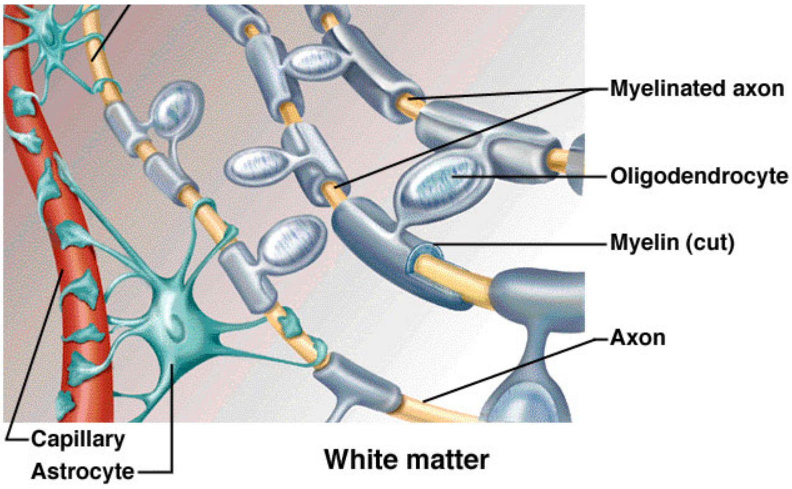

Figure 1.2. Idealised illustration of the structure and position of glial cells [12].

Astrocytomas are the most frequent primary brain tumour in adults, and are a major cause of morbidity and mortality [11]. Brain tumours are the third or fourth most frequent cause of cancer-related deaths in middle-aged males and the second commonest cause of cancer deaths in children [11].

1.2.3 Classification System – WHO

Since 1829 there have been various classification schemes for the histogenic and, later, the histological grading of central nervous system (CNS) tumours [11]. In 1993 the World Health Organisation (WHO) published the revised *WHO Histological Typing of Tumours of the Central Nervous System* [13], which has been subsequently updated in 2000 by Kliehues and Cavenee [14]. This classification system grades glial tumours on a scale from grade I, being benign, to grade IV, being malignant, as has been established in previous WHO typings. It is based more upon survival data than histopathologic features (such as nuclear atypia, mitoses, endothelial cell proliferation, and necrosis), and is therefore more of a "malignancy scale" [11]. The 1993 WHO histopathology-based Classification of Tumours of the Central Nervous System for gliomas is shown in Table 1.1 [11]:

WHO Grade	*Histopathologic features:*	Nuclear atypia	Mitotic activity	Endothelial proliferation / necrosis
I	Juvenile pilocytic astrocytoma	▨	▨	▨
II	Astrocytoma variants • Fibrillary • Protoplasmic • Gemistocytic	✓	▨	▨
III	Anaplastic astrocytoma	✓	✓	▨
IV	Glioblastoma variants • Giant cell • Gliosarcoma	✓	✓	✓

Table 1.1. The 1993 WHO histopathology-based classification for gliomas originating from astrocytes [11].

The tumours described in Table 1.1 originate from astrocytes making up the majority of gliomas. Neoplasms originating from oligodendrocytes comprise approximately a third of intracranial gliomas [11]. The WHO system for oligodendroglial tumours is [11]:

WHO Grade	
II	Oligodendroglioma
III	Anaplastic oligodendroglioma

Table 1.2. The 1993 WHO histopathology-based classification for gliomas originating from oligodendrocytes [11].

Since these grades are based on survival data, the grading of an individual patient’s glioma should relate to the prognosis for that patient. The administering of suitable treatment is dependent on the grade of the tumour: what may be effective therapy for a grade III tumour may not have any curative effect on a tumour of grade IV.

There are no classification systems for the grading of liver tumours. They are defined as primary (originating in the hepatic cells) or secondary (having metastasised from another organ). Hepatocellular carcinoma is the most common form of primary liver tumour, which is the most common form of cancer in the world today being more prevalent in men and in the Orient [15, 16]. Hepatocellular carcinoma is strongly associated with liver cirrhosis, and causes involve viruses and chemical agents [15, 16]. Hepatitis B and C are the most important causes around the world, along with alcohol-induced liver damage and poisoning by some toxins, iron and arsenic [15, 16]. Liver tumours are highly malignant and can be fatal even before metastasising outside of the liver. The chances of survival if the disease is caught at a late stage, as usual, are minimal [16, 17]. The liver is a common site for metastasis from primary tumours in almost any organ of the body, via the lymph and vascular systems [18]. Common sites of origin are breast, colon/rectum, stomach, ovaries, kidney, skin (melanin), oesophagus, testis, and placenta [18].

1.3 OVERVIEW OF ANGIOGENESIS

1.3.1 What is Angiogenesis?

This sub-section is based on [19].

Angiogenesis is the “creation of new blood vessels”, and is a naturally occurring process in the body, both in health and disease. In the healthy body angiogenesis occurs to heal wounds and for restoring blood flow to tissues after injury or insult.

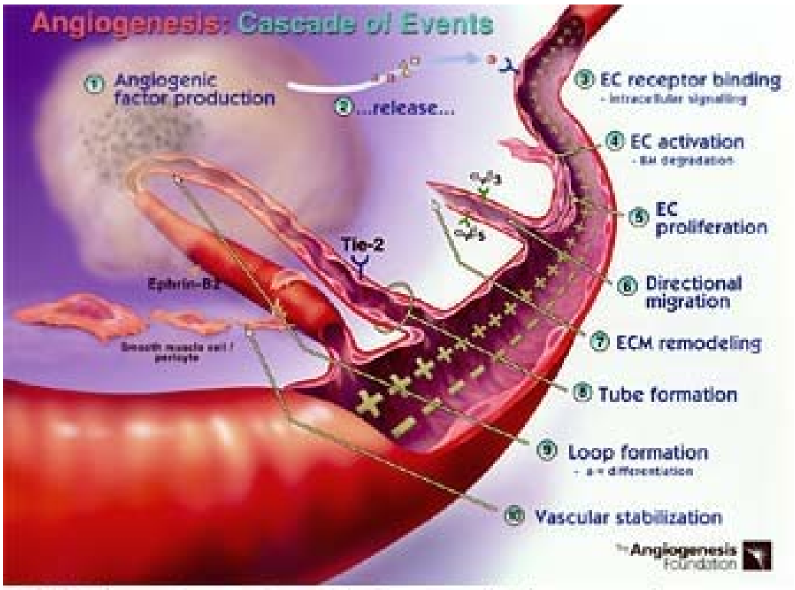

© 2000 The Angiogenesis Foundation, Inc. All rights reserved.

Figure 1.3. Depiction of the stages involved in angiogenesis [19].

The healthy body controls angiogenesis through a series of "on" and "off" switches. The main "on" switches are the *angiogenesis-stimulating growth factors* and the main "off" switches are the *angiogenesis inhibitors*. When angiogenic growth factors are produced in excess of angiogenesis inhibitors, the balance is tipped in favor of blood vessel growth. When inhibitors are present in excess of stimulators, angiogenesis is stopped. The normal, healthy body maintains a balance of angiogenesis modulators. In general, angiogenesis is "turned off" by the production of more inhibitors than stimulators. In many serious disease states, the body loses control over angiogenesis. Angiogenesis-dependent diseases result when new blood vessels either grow excessively or insufficiently.

In the early stages of a tumour's growth it can be sustained by passive diffusion of nutrients and oxygen. However, this only remains efficient for a volume of less than 1 mm^3, after which a tumour requires its own blood supply to sustain its growth. Under hypoxic and hypoglycaemic conditions a tumour initiates the process of angiogenesis by releasing angiogenesis-stimulating cytokines. Vascular endothelial growth factor (VEGF), also known as vascular permeability factor (VPF), is the most common of these angiogenesis-promoting cytokines secreted by tumour tissue.

The process of angiogenesis occurs as an orderly series of events (see Fig. 1.3) [19]:

1. Diseased or injured tissues produce and release angiogenic growth factors (proteins) that diffuse into the nearby tissues
2. The angiogenic growth factors bind to specific receptors located on the endothelial cells (EC) of nearby preexisting blood vessels
3. Once growth factors bind to their receptors, the endothelial cells become activated. Signals are sent from the cell's surface to the nucleus. The endothelial cell's machinery begins to produce new molecules including enzymes
4. Enzymes dissolve tiny holes in the sheath-like covering (basement membrane) surrounding all existing blood vessels
5. The endothelial cells begin to divide (proliferate), and they migrate out through the dissolved holes of the existing vessel towards the diseased tissue (tumour)
6. Specialised molecules called adhesion molecules, or integrins (avb3, avb5) act like grappling hooks to help pull the sprouting new blood vessel sprout forward
7. Additional enzymes (matrix metalloproteinases, or MMP) are produced to dissolve the tissue in front of the sprouting vessel tip in order to accommodate it. As the vessel extends, the tissue is remolded around the vessel
8. Sprouting endothelial cells roll up to form a blood vessel tube
9. Individual blood vessel tubes connect to form blood vessel loops that can circulate blood

10. Finally, newly formed blood vessel tubes are stabilized by specialized muscle cells (smooth muscle cells, pericytes) that provide structural support. Blood flow then begins.

Unlike mature vasculature, the endothelia of microcapillaries produced by angiogenesis are not well formed and gaps remain between their endothelial cells making them characteristically permeable or “leaky”.

1.3.2 Inhibiting Angiogenesis

This sub-section is based on [20].

It has been shown that angiogenesis plays a vital role in the growth and spread of tumours. Before the 1960s, cancer researchers believed that the blood supply reached tumours simply because pre-existing blood vessels dilated. But later experiments showed that angiogenesis is necessary for tumours to keep growing and for cancers to spread [21]. In animal experiments, when tumour cells were implanted in areas isolated from blood vessels the tumour only grew to a size of 1 mm in diameter and then stopped even with the availability of nutrients. However when tumour cells were implanted in areas of the animal near to blood vessels angiogenesis occurred allowing the tumour to grow larger [22]. Among more than a dozen different proteins and several smaller molecules that have been found to activate angiogenesis, two proteins have been found to be the most important for sustaining tumour growth: vascular endothelial growth factor (VEGF) [23, 24] and basic fibroblast growth factor (bFGF). Although many tumours produce angiogenic molecules such as VEGF and bFGF, their presence is not enough to begin blood vessel growth. For angiogenesis to begin, these activator molecules must overcome a variety of angiogenesis inhibitors. Almost a dozen naturally occurring proteins can inhibit angiogenesis. Among this group of molecules, proteins called angiostatin, endostatin, and thrombospondin appear to be especially important. A finely tuned balance, between the concentration of angiogenesis inhibitors and of activators, determines whether a tumour can induce the growth of new blood vessels.

The discovery of angiogenesis inhibitors raises the question of whether such molecules might therapeutically halt or restrain a tumour's growth. Researchers have addressed this question in numerous animal experiments. In one striking study, mice with several different kinds of cancer were treated with injections of endostatin. After a few cycles of treatment, the initial (primary) tumour formed at the site of the injected cancer cells almost disappeared, and the animals did not develop resistance to the effects of endostatin after repeated usage.

Almost two dozen angiogenesis inhibitors are currently being tested in cancer patients. The inhibitors being tested fall into several different categories, depending on their mechanism of action. Some inhibit endothelial cells directly, while others inhibit the angiogenesis signaling cascade or block the ability of endothelial cells to break down the extracellular matrix.

One class of angiogenesis inhibitors being tested in cancer patients are molecules that directly inhibit the growth of endothelial cells. Included in this category is endostatin, the naturally occurring protein known to inhibit tumour growth in animals. Another drug, combretastatin A4, causes growing endothelial cells to undergo apoptosis. Other drugs, which interact with a molecule called integrin, also can promote the destruction of proliferating endothelial cells.

A second group of angiogenesis inhibitors being tested in human clinical trials are molecules that interfere with steps in the angiogenesis signalling cascade. Included in this category are anti-VEGF antibodies that block the VEGF receptor from binding with the growth factor. Another agent, interferon-alpha, is a naturally occurring protein that inhibits the production of bFGF and VEGF, preventing these growth factors from initiating the signalling cascade. Also, several synthetic drugs capable of interfering with endothelial cell receptors are currently being tested in cancer patients. One property of VEGF is promotion of neovascular endothelial permeability, so that inhibiting VEGF would be expected to cause a reduction in permeability that could be measured using DCE-MRI. Physiological parameters related to microvascular endothelial permeability are derived by the application of pharmacokinetic modelling to DCE-MRI, and hence DCE-MRI data collected before and after treatment with an anti-VEGF antibody can allow the assessment of the antibody's action by measuring the change in the permeability-related parameter. The choice of pharmacokinetic model in this context is of paramount consideration. The permeability-related estimates obtained must be accurate, reliable and independent from other physiological factors (such as blood volume) so that the true and specific affect of the anti-VEGF antibody can be evaluated.

A third group of angiogenesis inhibitors are directed against one of the initial products made by growing endothelial cells, namely, the MMPs, enzymes that catalyze the breakdown of the extracellular matrix. Because breakdown of the matrix is required before endothelial cells can migrate into surrounding tissues and proliferate into new blood vessels, drugs that target MMPs also can inhibit angiogenesis. Several synthetic and naturally occurring molecules that inhibit the activity of MMPs are currently being tested to see if interfering with this stage in the process of angiogenesis will prolong the survival of cancer patients.

1.3.3 What is involved in Clinical Drug Trial Studies?

This sub-section is based on [20]

Clinical trial studies are carried out with tumour patients to find out whether promising approaches to cancer prevention, diagnosis, and treatment are safe and effective. DCE-MRI and pharmacokinetic modelling have a crucial role to play in clinical trials of anti-angiogenic agents for the direct, non-invasive, *in vivo* measurement of their effectiveness. Since the physiological parameters (such as blood volume and microvascular endothelial permeability) are associated with angiogenic activity, changes in their value over a course of treatment is directly related to the action of the agent. All drugs undergo a long and careful research process which concludes with a clinical drug trial. The use of DCE-MRI must therefore conform to the current drug development and efficacy system. This is extremely demanding, in terms of how it is done, what methods should be used, and other considerations.

The different types of clinical trials are as follows [20]:

- *Treatment trials* test new treatments (like a new cancer drug, new approaches to surgery or radiation therapy, new combinations of treatments, or new methods such as gene therapy).
- *Prevention trials* test new approaches, such as medicines, vitamins, minerals, or other supplements that doctors believe may lower the risk of a certain type of cancer. These trials look for the best way to prevent cancer in people who have never had cancer or to prevent cancer from coming back or a new cancer occurring in people who have already had cancer.
- *Screening trials* test the best way to find cancer, especially in its early stages.
- *Quality of Life trials* (also called *Supportive Care trials*) explore ways to improve comfort and quality of life for cancer patients.

Most clinical research that involves the testing of a new drug progresses in an orderly series of steps, called phases. This allows researchers to ask and answer questions in a way that results in reliable information about the drug and protects the patients. Clinical trials are usually classified into one of three phases [20]:

- Phase I trials: These first studies in people evaluate how a new drug should be given (by mouth, injected into the blood, or injected into the muscle), how often, and what dose is safe. A phase I trial usually enrols only a small number of patients, sometimes as few as a dozen, and looks for markers of toxicity, biological activity and pharmacokinetics.
- Phase II trials: A phase II trial continues to test the safety of the drug, and begins to evaluate how well the new drug works. Phase II studies usually focus on a particular type of cancer.
- Phase III trials: These studies test a new drug, a new combination of drugs, or a new surgical procedure in comparison to the current standard. A participant will usually be assigned to the standard group or the new group at random. Phase III trials often enroll large numbers of people and may be conducted at many doctors' surgeries, clinics, and cancer centres nationwide.

In chapter 6 we discuss in detail the application of pharmacokinetic modelling and DCE-MRI in a phase I study of an anti-VEGF antibody.

1.4 OVERVIEW OF DCE-MRI TECHNIQUES (T_1 AND T_2*) AND ANALYSIS

1.4.1 Clinical uses of Magnetic Resonance Imaging

The excellent contrast of soft tissue provided by MRI makes it ideal for routine clinical use. Unlike X-ray Computed Tomography (CT) or Nuclear Medicine, MRI incurs no radiation dose, so MR images can be acquired repeatedly, and unlike Ultrasound or Positron Emission Tomography (PET), MR images offer excellent anatomical detail and therefore MRI has taken a prominent role in surgical and radiotherapy guidance. MR images can be acquired and reconstructed in any profile, cross sectional position and angular orientation, and schemes exist for volumetric acquisition and acquiring a series of slices with overlap, interleave or gaps in between to allow improved coverage with consideration of signal-to-noise and/or scan time. These properties make MRI a very versatile imaging modality for clinical purposes.

One of the major values of MRI is the ability to derive images using a number of different contrast mechanisms. These are based on different systems of energy transfer occurring within the tissue which include

PD - proton density
T_1 - spin-lattice/longitudinal relaxation following RF excitation
T_2 - spin-spin/transverse relaxation following RF excitation
T_2* - shortened, effective T_2 because of magnetic field inhomogeneities

The inherent relaxation properties of hydrogen protons in different tissues causes the image contrasts shown in Table 1.3 for the normal brain.

	Relaxation time		Image contrast		
	T_1	T_2	T_1	T_2	PD
Cerebral spinal fluid	Long	Long	Dark	Bright	Bright
Grey matter	Intermediate	Intermediate	Grey	Grey	Isointense
White matter	Short	Short	Bright	Grey	Bright
Fat	Short	Intermediate	Bright	Grey	Bright
Air	-	-	Dark	Dark	Dark
Fast-Flowing blood	Long	Short	Dark*	Dark*	Dark*
Oedema	Long	Long	Dark	Bright	Bright

Table 1.3. Relative relaxation times and image contrast of tissues in the normal brain. *Fast-flowing blood appears dark on spin-echo acquisitions but appears bright on gradient-echo acquisitions.

A typical clinical MRI examination would include T_1-weighted, T_2-weighted and a fluid-suppressed acquisition (such as fluid attenuated inversion recovery (FLAIR) [25]) to image anatomy. A combination of these acquisitions with differing tissue contrasts is valuable for tissue characterisation (such as identifying tumour core and oedema) and tissue segmentation (such as separation of grey matter, white matter and CSF).

The remainder of this sub-section is taken from [26], which has been written at our centre.

As in CT and Ultrasound, exogenous contrast media can be used to enhance the contrast in conventional anatomical MR imaging. In the brain, with brake-down of the blood-brain barrier, uptake of contrast agent clearly differentiates vasculature from surrounding tissue and accumulation of leaked contrast agent increases the sensitivity of detecting and delineating tumour tissue, in a static image. Also, similarly to PET and Nuclear Medicine, contrast agent can be employed as a tracer and its distribution in the body over time can provide quantitative physiological information with dynamic imaging. There are significant differences between the mode of action of MR contrast agents and those used in, for example, X-ray imaging. The paramagnetic ion, usually gadolinium, included in the contrast agent pharmaceutical compound actually acts upon the surrounding water by changing local field strength. MR signal is not observed from the contrast medium itself, only its effect is observed indirectly. MR contrast agents “catalyse” proton relaxation – like a transient chemical bonding between water protons and the paramagnetic ion. The degree of relaxation enhancement, the relaxivity of the ion, can be interpreted as being related to the number of these bonds that can form and the time scale over which they occur. This relaxivity can be harnessed, through shortening of relaxation times (T_1 and T_2) in tissue, to estimate contrast agent concentrations *in vivo*. In addition to this catalysis effect water protons are also influenced by the bulk magnetic susceptibility (BMS) shift due to the contrast agent. Local magnetic field variations induced by an inhomogeneous distribution of paramagnetic ions produce a relatively long range heterogeneous magnetic field which shortens T_2 and T_2*. This effect can dominate the relaxivity effect when superparamagnetic or ferromagnetic substances (ions with some degree of magnetic ordering) are employed or when compartmentalisation of the contrast agent occurs [27]. This effect can be harnessed for dynamic susceptibility contrast MRI. Contrast agent studies using susceptibility contrast MRI and conventional T_1-weighted (relaxivity enhanced) MRI techniques both measure the influence of the same MR contrast agent through its affect on relaxation times. However, the susceptibility effect is long range in nature and results from compartmentalisation of the contrast agent. Thus a small amount of contrast agent restricted to the vascular spaces in the brain (occupying only a few percent of the brains volume) can produce a long range effect (stretching beyond the vessel walls) that dominates any relaxivity effect seen in the water of the vascular spaces. Conversely, if the brain’s blood-brain barrier is compromised and the contrast agent leaves the blood vessels, the BMS effect is significantly reduced but short-range relaxivity effects are extended into the interstitial spaces. These two effects may be differentiated through the appropriate choice of imaging sequence. A T_2*-weighted sequence is sensitive to BMS effects and is chosen to monitor contrast agent behind an intact blood brain barrier. A T_1-

weighted sequence may be an inappropriate choice for such a situation since the short-range T_1 effects influence such a small proportion of the overall tissue signal that only very small signal changes result from contrast agent administration. However, once the blood brain barrier is compromised and contrast agent enters the large water pool of the interstitial spaces these T_1 effects become much larger. For the same reasons T_1-weighted acquisitions are generally favoured for monitoring the distribution of MR contrast agents in tumours at all anatomical locations, as it is generally the case that tumours do not possess a mechanism for preventing contrast agent leakage from the blood pool, particularly in the brain because of the breakdown of the blood-brain barrier.

1.4.2 Contrast media employed for DCE-MRI

This sub-section is taken from [28, 29].

MR contrast media either act predominantly on T_1 relaxation which results in signal enhancement (“positive” contrast) on T_1-weighted acquisitions, or on T_2 relaxation which results in signal reduction (“negative” contrast) on T_2- or T_2*-weighted acquisitions.

The positive contrast agents are typically small molecular weight compounds containing as their active element gadolinium (Gd), manganese (Mn) or iron (Fe), all of which have unpaired electron spins in their outer shells and long relaxivities which make them good T_1 relaxation agents. Haemoglobin also belongs to this group of agents and is an intrinsic MR contrast medium, the paramagnetic T_2* properties of which are used in the BOLD (blood oxygen level dependent) effect. The other group of agents are small particulate aggregates often termed superparamagnetic contrast medium. These agents produce predominantly T_2 (and T_2*) relaxation effects, but very small particles smaller than 300 nm also produce substantial T_1 relaxation. A final group, the perfluorocarbons, are negative contrast agents because their presence excludes the hydrogen atoms responsible for the signal in MR imaging.

The use of MR contrast media depends on the chemical formulation of the contrast medium. In a manner analogous to nuclear imaging, agents have been developed which have a certain degree of tissue affinity. However, an MR contrast medium has to be given in concentrations 10^4 - 10^6 higher than the radiopharmaceuticals to produce effects visible in the images. The clinically introduced substances are either renally or hepatically excreted media, which stay in the intravascular/extracellular tissue compartment. Compounds under development have affinity to certain organs or even tumours; the paramagnetic particles have affinity for the RES (reticuloendothelial system) or they stay in the intravascular space for a prolonged period. Contrast media are also used to contrast the bowel against the surrounding abdominal tissues. A selection of MR contrast media that are currently licenced for use in neuroradiology and whole body studies are shown in Table 1.4 [28]:

Name of Compound	*Central Moiety*	*Distribution*	*Trade Mark*
Gadopentate dimeglumine, Gd-DTPA	Gd^{3+}	intravascular, extracellular	Magnevist
Gadoterate meglumine, Gd-DOTA	Gd^{3+}	Intravascular, extracellular	Dotarem
Gadodiamide, Gd-DTPA-BMA	Gd^{3+}	Intravascular, extracellular	Omniscan
Gadoteridol, Gd-HP-DO3A	Gd^{3+}	Intravascular, extracellular	Prohance

Table 1.4. A selection of Gadolinium-based MR contrast media currently licenced for clinical use.

There are many other contrast agents that are undergoing clinical trials or have been approved for sale. The design objectives for the next generation of MR contrast agents are likely to focus on prolonging intravascular retention, improving tissue targeting, and accessing new contrast mechanisms. Macromolecular paramagnetic contrast agents are being tested worldwide. Preclinical data shows that these agents demonstrate great promise for improving the quality of MR angiography and myocardial perfusion.[29]

1.4.3 Measuring contrast passage

This sub-section is taken from [26], which has been written at our centre.

To monitor the kinetic behaviour of a contrast agent *in vivo* it is necessary to link the changes in concentration to changes seen in MR images. Since most agents are known to alter both the spin-lattice and spin-spin relaxation rates of tissues it should be possible to infer their distribution by observing the influence on the MR signal. Due to the Solomon-Bloembergen equation the concentration of Gd ions is known to be directly proportional to the change in $1/T_1$. Provided that the BMS shift is negligible, the relationship between relaxation rate ($1/T_1$ and $1/T_2$) and contrast agent concentration can be predicted [30]:

$$\frac{1}{T_1} = \frac{1}{T_{10}} + r_1[Gd] \tag{1.1}$$

$$\frac{1}{T_2} = \frac{1}{T_{20}} + r_2[Gd] \tag{1.2}$$

where r_1 and r_2 are the spin-lattice and spin-spin relaxivity constants respectively and T_{10} and T_{20} are the T_1 and T_2 values respectively in the absence of contrast material. These relationships have both been confirmed *in vitro* [31, 32] [33] and for T_1 *in vivo* [34] across a range of concentrations. Relaxivity is dependent upon field strength and the chemical structure of the contrast agent [27].

Using these relationships, a series of measurements of the T_1 of a tissue as a contrast agent distributes within it could be used to monitor the changes in contrast agent concentration. Since the changes in T_1 will also alter the signal intensity of a T_1-weighted imaging sequence, it should also be possible to monitor contrast agent concentration using signal intensity.

The choice of pulse sequence to monitor contrast agent kinetics must satisfy the following criteria: (1) The rate of measurement of contrast agent concentration should be sufficient to monitor the most rapid changes occurring within the tissue. (2) The relationship between concentration of contrast agent and the measuring function should be monotonic and minimally affected by small changes in the imaging parameters. (3) The sequence should provide acceptable spatial resolution and tissue coverage. T_1-weighted sequences offer many advantages over T_2-weighted sequences, as T_2-weighted images tend to take more time to collect and the effect of contrast agent on signal intensity is negative (i.e. reducing the signal-to-noise ratio). The relationship between the contrast agent concentration and the relative increase in signal intensity can be derived from the Bloch equations [35] for any imaging sequence. The signal intensity obtained from the commonly used gradient echo sequence with spoiling of the transverse magnetisation (FLASH) is described below:

$$S = g.\rho.\frac{\sin(\alpha).\left(1-\exp\left(-\frac{TR}{T_1}\right)\right)}{\left(1-\cos(\alpha).\exp\left(-\frac{TR}{T_1}\right)\right)}.\exp\left(-\frac{TE}{T_2{}^*}\right) \qquad \textbf{1.3}$$

where ρ is the proton density, α is the flip angle, and g is a constant determined by system receiver and image reconstruction settings. If we assume that Gd ions have no effect on ρ and that the TE is so short as to be able to neglect the influence of T_2* (or more importantly changes in T_2* during the time series), then the Gd ions influence signal intensity via their effect on T_1 alone. As α approaches 90° and TR/T_1 becomes small the relationship between signal intensity and $1/T_1$ is approximately linear:

$$S \approx \frac{g.\rho.TR}{T_1} \qquad \textbf{1.4}$$

This relationship remains approximately valid across a range of values for TR/T_1 and α. The constant of proportionality is a function of TR, g, ρ, and, as the flip angle decreases, α. The difficulty in comparing this constant between studies is the sensitive nature of g. The loading of the coil, receiver settings at the MR console and image reconstruction parameters alter the intensity of the signal in the image. Hence, it is necessary to relate the signal intensity to an internal standard. One option is to relate the signal intensity post-contrast to that pre-contrast. This has the advantage of maintaining the position of the standard in relation to the enhancing structure and requires no prior positioning. However, the use of pre-contrast signal intensity also introduces the pre-contrast T_1 of the structure into the analysis. If we assume signal intensity is proportional to $1/T_1$, then;

$$\frac{S_{Gd} - S_0}{r.\rho.TR} \approx \left(\frac{1}{T_{1Gd}} - \frac{1}{T_{10}}\right) = r_1[Gd] \qquad \textbf{1.5}$$

where S_0 and S_{Gd}, and T_{10} and T_{1Gd} are the signal intensities and spin-lattice relaxation times before and following administration of contrast agent respectively and r_1 is the relaxivity of contrast agent. Dividing by the pre-contrast signal we obtain:

$$\frac{S_{Gd} - S_0}{S_0} \approx r_1 T_{10}[Gd] \qquad \textbf{1.6}$$

Therefore the relative increase of signal intensity following administration of contrast agent is related to both the spin-lattice relaxivity of contrast agent and the pre-contrast T_1 of the tissue. This linear relationship between signal intensity and contrast agent concentration is only approximately true over a limited range of contrast agent concentration. Unfortunately, the measurement of T_1 *in vivo* is a non-trivial problem and, importantly, accurate measures of T_1 are often time consuming to obtain. The more common methods of measuring T_1 using MR images fall broadly into two categories:

1. Inversion/saturation recovery prepared imaging sequences, and
2. Variable saturation techniques.

Each technique may be accomplished using a number of imaging sequences including; spin echo, EPI, or gradient-echo imaging with the appropriate additional pulses and subsequent processing algorithms.

A) Inversion or saturation recovery techniques

An inversion pulse [36] or a series of saturation pulses [37] provides T_1-weighted preparation of the signal dependent upon the subsequent delay prior to acquisition of a normal imaging sequence. Using a series of images, each obtained with a different delay, the T_1 of the sample may be estimated [36]. While this is perhaps the most precise method of obtaining an estimate of T_1, and the precision increases with the number of delay times used, it can be very time consuming. Precise estimates of longer T_1 values requires the use of a longer maximum TI and consequently, TR. The time required for such measurements can be reduced significantly by the use of snapshot-FLASH [36] or EPI-based approaches [30] to sample an entire image at each TI, although these methods can be degraded by severe point spread function artefacts [37]. Further time savings can be made using Look-Locker techniques [38], although there is a limitation on the number of slices that may be acquired per unit time.

B) Variable saturation techniques

T_1 may be estimated using the ratio of two spin echo images collected with different TRs, but again imaging times can become prohibitive. A similar approach is to use gradient echo images with variable flip angles [39]. The signal intensity obtained using a FLASH sequence has been described above. Rearranging this equation yields:

$$Y = \exp\left(-\frac{TR}{T_1}\right).X - g.\rho.\left(1-\exp\left(-\frac{TR}{T_1}\right)\right).\exp\left(-\frac{TE}{T_2*}\right) \qquad \mathbf{1.7}$$

where $Y = \frac{S_\alpha}{\sin(\alpha)}$ and $X = \frac{S_\alpha}{\tan(\alpha)}$, and S_α is the signal measured using a flip angle α (from eq. 1.3). Hence a plot of Y against X for a range of flip angles will result in a straight line, and T_1 may be calculated from the slope. Wang et al. [40] have described the optimal sequence parameters for minimisation of the error in the calculated T_1 when only two flip angles are used. With a given T_1 two flip angles can be chosen which provide a greater precision in T_1 estimate than a comparable spin echo pair. It may, however, be difficult to choose an appropriate pair of flip angles if the sample contains an unknown or large range of T_1 values. Here the use of a number of equally spaced flip angles may be employed. However, in this case it may be advantageous to use a more computationally intensive non-linear fit using the original FLASH equation (eq. 1.3) if the precision is to be improved [40].

In the field of DCE-MRI it is common to measure T_1 using variable flip angle gradient echo acquisitions, usually while keeping TR constant. Such techniques require only relatively short acquisition times, which allows good temporal resolution, and may be used in multi-slice [41] or 3D volume modes to provide tissue coverage [42, 43]. A simple protocol for a quantitative DCE-MRI study utilises a single heavily proton density-weighted (PD-weighted) acquisition, acquired prior to contrast agent administration, followed by numerous T_1- weighted acquisitions over time (for example [9, 44, 45]). This could be achieved by using a low flip angle for the PD-weighted acquisition, and a higher flip angle for each of the dynamic T_1-weighted acquisitions, whilst keeping TR short to maintain temporal resolution. Note that the PD-weighted acquisition is obtained only once; T_1 is always estimated by comparing the signal intensity of the T_1-weighted acquisitions (before or after contrast agent administration) with this single PD-weighted acquisition. Such a strategy allows T_1 to be estimated rapidly throughout the time course of signal enhancement.

Selection of an imaging methodology begins with a series of basic choices such as an appropriate RF coil, imaging plane and sequence to avoid issues such as flow artefacts and field of view aliasing. Subsequently, the choice of T_1-weighted sequence for bolus tracking must fulfil a long list of both generic and study-specific criteria and a wide range of methods have been used in the field. High in the list of generic criteria are: temporal resolution, T_1 sensitivity and dynamic range, spatial coverage, and resolution; each of these competes against noise for the limited MR signal. Perhaps the principal decision to be made when selecting a T_1-weighted sequence for bolus tracking is whether or not an arterial input function (AIF) will be measured.

There are several approaches described for measurement of an AIF (using FLASH or gradient echo imaging), but there are general problems with obtaining an ideal AIF. In practice, it is very difficult to find the feeding artery for measuring the AIF and so a surrogate vessel has to be used. Feeding arteries tend to be small and an AIF measured from them will have partial volume effects. Arteries contain fast flowing blood which will cause in-flow effects and aliasing, resulting in distortion of the measured signal. Also due to the high blood flow in arteries high temporal resolution imaging is required to follow the course of contrast agent in them. Therefore a large imaging volume containing the feeding artery, with no partial volume effects, collected with a very high temporal resolution would allow measurement of an ideal AIF.

1.4.4 Pre-analysis procedures

Modern computational techniques allow the generation of parametric estimates on a pixel-by-pixel basis so that "parametric maps" can be formed from dynamic images. Therefore it is imperative that the spatial information matches exactly in each image through the dynamic course. Any shift in the imaging matrix in relation to the imaged sampled during the time course will result in the pixelwise processing giving spurious parametric estimates. Therefore dynamic images must be checked before analysing for any motion, because of breathing or general movement. Shifted images within a dynamic series can be realigned using registration algorithms and then analysed. The reference image for realigning to has to be chosen with care because of differences in spatial contrast from one image to the next. It would be best to use a rigid registration technique in this case. However, if the motion, due to breathing or vascular pulsation, occurs during acquisition of a dynamic image then there is no practical option for restoring the spatial information in the pixels affected, and the results of analysis will be erroneous. DCE-MRI studies in areas of the body prone to motion, such as the abdomen, require a carefully designed scheme employing post-acquisition registration technique or minimising motion using a pattern of breath-holds. We have used a breath-hold technique for acquiring DCE-MRI data and generating pixel-by-pixel maps of K^{trans} and blood volume *in vivo* in liver metastases, and this is presented in Chapter 5.

In-flow artefacts can also have a detrimental effect on the analysis of DCE-MRI data, particularly when measuring the AIF. In-flow effects are caused by some water protons in blood not being RF saturated and flowing into blood that has been saturated.

1.4.5 Subjective analysis techniques

This sub-section is taken from [46], which has been written at our centre.

Perhaps the simplest method for providing reliable and reproducible information that has a bearing on the kinetics of contrast agent accumulation is an integration of the concentration of the agent observed in the tissue of interest over time (the initial area under curve (*IAUC*), units mMols) [44]. The value of *IAUC* obtained in a tumour is dependent on the period over which integration is performed; typically this will be from the time point representing contrast agent administration or arrival in the tissue to a time *t*, typically 60 s – 120 s after the start time. $IAUC_t$ may then be defined as

$$IAUC_t = \int_0^t [CA](t')dt' \tag{1.8}$$

where $[CA](t')$ represents the concentration of contrast agent measured in the tissue at time t'.

Other approaches to quantification of the general shape of the contrast agent concentration time course include measurement of the peak concentration, gradient of concentration increase, time of contrast agent arrival, and time to maximum enhancement. Whilst some of these parameters are perhaps simpler still to estimate than *IAUC*, they are in general more prone to the effects of data noise, and are therefore expected to be less reproducible than *IAUC*.

Subjective analysis methods aim to provide indices related to contrast agent accumulation that are easy to derive and relatively reproducible. The major disadvantage in using such parameters is the difficulty in their interpretation and failure to isolate potentially useful tissue properties, such as blood volume and microvascular endothelial permeability.

Similarly, measures such as the gradient of contrast agent uptake, and the peak concentration during the time course are influenced by a number of physiological parameters in generally intractable proportions.

1.5 OVERVIEW OF PHARMACOKINETIC MODELS

This section is taken from [46], which has been written at our centre.

To allow us to attempt to quantify the observed contrast agent kinetics in terms of physiologically meaningful parameters we first need to define the elements of the tumour or tissue structure and the functional processes that affect the distribution of the tracer (the contrast agent). It is customary to represent tissue as comprising 3 or 4 compartments, each of which is a bulk tissue characteristic (that is, we are unable to observe these compartments at their natural microscopic scale, but we can observe their aggregate effects at the image voxel scale or in a region of interest). These compartments are the vascular plasma space, the extracellular extravascular space (EES), and the intracellular space [7]. A fourth tissue component forms a catch-all for all the other microscopic tissue components, such as membranes, fibrous tissues, etc. All clinically utilised MRI contrast agents, and most experimental agents, do not pass into the intracellular space of the tissue, due to their size, inertness, and non-lipophilicity, making the intracellular space inaccessible to probe using DCE-MRI; for this reason, the intracellular and ‘other’ volumes are usually combined as a loosely defined “intracellular space”. These three compartments may be expressed either in absolute terms (units ml per ml tissue or ml per g tissue if tissue density is known) or as fractions of tissue volume. In the latter case,

$$\begin{aligned} v_e + v_p + v_i &= 1 \\ v_p &= (1 - \mathrm{Hct})v_b \end{aligned} \qquad \mathbf{1.9}$$

where v_e is the fractional EES, v_p is the fraction occupied by blood plasma, v_i is the fraction occupied by the 'intracellular' space, v_b is the fraction occupied by whole blood, and Hct is the haematocrit (typically 0.45).

The functional parameters, or delivery mechanisms, that influence contrast agent distribution in the intravascular space and the EES are usually assumed to be restricted to blood flow F (units ml blood (g tissue)$^{-1}$ min^{-1}) and the endothelial permeability-surface area product PS (units ml g^{-1} min^{-1}), which describes how 'leaky' a capillary wall is. In reality there are additional functional parameters that may affect contrast agent distribution, including the rate of lymphatic drainage, the rate or degree of contrast agent mixing within compartments, and the degree of tracer diffusion in regions without an effective blood supply (e.g. areas of necrosis or oedema). Whilst some modelling approaches attempt to consider some of these factors explicitly, they are in general viewed as confounding factors in the kinetic analysis of DCE-MRI data, and a simplified model of diffusive transport is generally assumed.

1.5.1 Early Models

The kinetic modelling of contrast agent distribution has a basis in the simple rate equation describing diffusive flux across a permeable membrane [47-49]. The diffusive transport of a dissolved substance across a permeable membrane is determined by the difference in concentration of that substance between the two compartments that it separates and the freedom with which the membrane allows molecules to diffuse from one side to the other. The amount of substance per unit time that diffuses through the membrane, or diffusive flux Φ_d, may be defined as:

$$\Phi_d = PA(C_1 - C_2) \qquad \textbf{1.10}$$

where P is the trans-membrane permeability coefficient (units m min^{-1}), A is the cross-sectional area of the membrane through which transport is occurring (m^2), and C_1 and C_2 are the concentrations of permeant on each side of the membrane (mMol). The process outlined by eq. 1.10 governs the transport of lipophilic molecules across intact membranes. Small polar molecules, such as water, are also subject to such diffusive transport across membranes, but to a lesser extent than lipid-soluble molecules. A second transport mechanism is important in this case; through 'pores' or channels in the membrane. The rate of transport due to this effect is influenced by pressure differences across the membrane or partial pressure differences induced by an osmotic potential.

The system that is being probed using contrast agents *in vivo* is far more complex than a single membrane, and the simple rate equation of eq. 1.10 is overly simplistic. In addition to multiple possible transport mechanisms the model of a single membrane is obviously naive (as noted above, contrast agent molecules do not readily diffuse through intact lipid bilayer membranes), and the true situation that we wish to probe, the tissue capillary wall, is one of multiple cell membranes, basement membranes, and gaps of varying sizes. Fortunately, we can still utilise eq. 1.10 with the aid of two basic assumptions [50]. Firstly, we assume that multiple transport mechanisms via a given obstacle (e.g. diffusive transport and osmotic transport across a single membrane) may be treated as a system of n diffusive permeabilities in parallel, leading to a total permeability for a given obstacle of γ:

$$\gamma = \sum_i^n P_i \qquad \textbf{1.11}$$

Secondly, we assume that multiple obstacles to transport (e.g. overlapping membranes) may be treated as N permeabilities in series:

$$\frac{1}{P_T} = \sum_{i}^{N} \frac{1}{\gamma_i} \qquad \textbf{1.12}$$

We can therefore relate the total flux of a molecular species Φ_T to the overall permeability:

$$\Phi_T = P_T S(C_1 - C_2) \qquad \textbf{1.13}$$

where S is the *effective* surface area of, in our case, the capillary wall. As well as providing a means for combining the effects of more than one transport mechanism occurring via a set of obstacles at the capillary scale, this result also allows us to define permeability to a first order as a bulk, or volume averaged, quantity. This therefore allows us to make use of eq. 1.13 in data analysis of imaging voxels or volumes of interest that are large relative to the scale of the phenomenon of interest, as long as we are aware that our estimates of *PS* and other parameters are always bulk parameters. It should also always be remembered that (for the purposes of this chapter, at least) all transport processes are being modelled as diffusive transport.

Low molecular weight contrast media available for clinical MRI studies, such as gadopentetate dimeglumine (Gadolinium diethylenetriaminepentaacetic acid or Gd-DTPA, molecular weight approx 500 Daltons [51]) and medium weight experimental molecules, transfer between the blood pool and the extravascular extracellular space (EES) of the tissue or tumour at a rate determined by the blood flow to the tissue, the permeability of the blood vessel walls, and the surface area of the perfusing vessels. The contrast agent does not cross cell membranes and its volume of distribution is therefore effectively the EES.

On T_1-weighted images, T_1 relaxation time shortening caused by the contrast agent in the interstitial space is the dominant mechanism of enhancement seen, although a variable contribution from contrast agent in the blood vessels, especially in highly vascular tumours, may also be observed. The early phase of contrast enhancement (often referred to as the first pass in bolus injection studies) involves the arrival of the contrast medium in the tissue of interest via the arterial supply, and lasts a number of cardiac cycles. In the presence of well-perfused and leaky vessels contrast medium immediately begins to pass into the EES, in a manner similar to that predicted by eq. 1.13. Over a period lasting many hours, the contrast agent is removed from the blood stream by renal excretion, and it therefore washes out of the EES, again in a manner similar to that predicted by eq. 1.13.

Equation 1.13 may be modified to account for contrast agent kinetic parameters that are more familiar to those working with DCE-MRI. The rate of accumulation and wash-out of an extracellular contrast medium in the EES, under the assumption that contrast agent is well-mixed in the vascular plasma space, v_p, and in the EES, can be described by a modified general rate equation (see for example [48]):

$$v_e \frac{dC_e(t)}{dt} = K^{\text{trans}}(C_p(t) - C_e(t)) \qquad \textbf{1.14}$$

where C_e is the concentration of agent in v_e, C_p is the concentration of agent in v_p, and K^{trans} is the volume transfer constant between v_p and v_e [7].

The study of contrast agent kinetics using MRI has seen a range of compartmental modelling approaches suggested (for example [9, 52-54]). Most of these have been shown to be theoretically compatible, after some manipulation, with the general compartmental contrast agent kinetic equation given in eq. 1.16 [7, 55]. However, there have historically often been significant differences in the assumptions used in the application of each model. The determination of an arterial input function (AIF) to define $C_p(t)$ is an example where differences frequently occur. The early model proposed by Tofts [52] used an assumed AIF of biexponential form drawn from literature regarding elimination of Gd-DTPA in the normal population [56]. The model originally proposed by Brix [53] attempted to define an exponentially decaying AIF on a patient-by-patient basis by including this as a free fitting parameter. The approach proposed by Larsson [54] utilised an AIF measured from blood samples drawn from the brachial artery at intervals of 15 s during the DCE-MRI data acquisition [54]. Often such differences may be traced to the fact that the development of many analysis methods has proceeded in tandem with a specific data acquisition programme, and the modelling assumptions frequently reflect limitations imposed by the data. Care must therefore be taken in applying these methods in settings other than those originally intended and in comparing apparently compatible results from different studies using different models and/or data acquisitions. Modern scanning protocols often provide the possibility of explicit determination of an AIF from the imaging data.

1.5.2 Development of models along with scanner speed and computational capability

If the delivery of contrast medium to the tissue is ample (meaning that the rate of extraction of contrast agent via the leaky capillary wall is small compared with the rate of replenishment via perfusion), K^{trans} is equal to the product of the capillary wall permeability and the (effective) capillary wall surface area per unit volume, $PS\rho$. PS is the permeability surface area product per unit mass of tissue (ml g^{-1} min^{-1}), and ρ is the tissue density (g ml^{-1}). However, if the delivery of the contrast medium to a tissue is insufficient, blood perfusion will be the dominant factor determining contrast agent kinetics, and K^{trans}

approximates $F\rho$(1-Hct), where F is blood flow (units ml blood (g tissue)$^{-1}$ min^{-1}). Thus in regions with a poor blood supply, low transfer coefficient values may be observed despite high intrinsic vessel permeability [57, 58]. Consideration of a general mixed perfusion- and permeability-limited regime leads to K^{trans} being equal to $EF\rho$(1-Hct) [7], where E is the extraction fraction of the tracer (i.e. the fraction of tracer that is extracted from v_p into v_e in a single capillary transit) [47]:

$$E = 1 - \exp\left(- \frac{PS}{F\left(1 - \text{Hct}\right)} \right) \qquad \textbf{1.15}$$

The relationships described above form the basis of the models used to describe contrast agent kinetics by a number of researchers, and the conventions for the names and symbols used are now generally accepted [7]. In normal tissues, the vascular volume is a small fraction of the total tissue volume (approximately 5 %, although it can be considerably higher in some tissues), and it is sometimes assumed (largely as a matter of convenience) that the tracer concentration in the tissue as a whole, C_t, is not influenced to a large degree by the concentration in the vessels (i.e. that $C_t \approx v_e C_e$) [52]. Whilst this assumption is acceptable in abnormalities with no large increase in blood volume that are situated in tissues with a relatively low normal blood volume, it is invalid in many contexts, especially as blood volume can increase markedly in tumours. Models of additional sophistication are required to allow these cases to be described, and a number of investigators (see for example [7, 55, 59-62]) have attempted to incorporate the effects of a significant vascular signal. Perhaps the most straightforward approach is to extend eq. 1.14 to include the concentration of contrast agent in the blood plasma, giving $C_t = v_p\, C_p + v_e\, C_e$. Using this relationship and by rearrangement of eq. 1.14 we then have

$$C_t(t) = v_p C_p(t) + K^{\text{trans}} \int_0^t C_p(t') \exp\left(\frac{-K^{\text{trans}}(t - t')}{v_e} \right) dt' \qquad \textbf{1.16}$$

which may be re-expressed as

$$C_t(t) = v_p C_p(t) + C_p(t) \otimes H(t) \qquad \textbf{1.17}$$

where $H(t)$ is the impulse response (or residue) function,

$$H(t) = K^{\text{trans}} \exp\left(-\frac{K^{\text{trans}} t}{v_e} \right) \qquad \textbf{1.18}$$

and ⊗ represents the convolution operation.

It has been noted that the special case of analysis only of the first passage of a contrast agent bolus is amenable to a simplified form of kinetic model [9, 55, 63]. It is assumed that during the first passage of a bolus of contrast agent through a tissue (a period that lasts up to approximately 1 minute), that the flux of contrast agent from the vascular compartment into the interstitial space, v_e, will not be enough to make the concentration of contrast agent in v_e significant when compared with the extremely large concentrations seen in the vascular space during this period (that is $C_p(t) >> C_e(t)$). Under these conditions, it can be shown that [9, 64]:

$$C_t(t) = v_p C_p(t) + K^{\text{trans}} \int_0^t C_p(t')dt' \qquad \textbf{1.19}$$

This model variant is therefore attractive in situations where a limited period of acquisition is either necessary or desirable. This may include the study of restless patients or studies in regions that may benefit from the use of a breath-hold (for example lung or liver tumours) [65]. Note that this convenience is achieved at the expense of determining the parameter v_e, and that for situations where the ratio K^{trans}/v_e (eq. 1.16) is large the assumptions underlying this approach break down.

Tofts, Brix and Larsson use DCE-MRI time courses acquired over a relatively long duration to estimate K^{trans}, v_e etc., and use exponential-type functions to describe the AIF, which has been found to seriously underestimate intravascular contrast concentration in the first pass of contrast bolus. Since Li et al.'s model only concentrates on the DCE-MRI time course data up to the end of the first pass of contrast bolus to calculate $\mathrm{K}^{\mathrm{trans}}$, blood volume, etc., it uses a gamma-variate shape to parameterise the AIF. The gamma-variate fits the first pass peak well, thereby giving a much better estimate of intravascular contrast concentration for subsequent analysis.

We have compared an earlier pharmacokinetic model – that of Tofts and Kermode [52] with technical modifications – with the later method of Li et al [9]. This is presented in Chapter 2.

1.5.3 Description of the First Pass Leakage Profile Method

Li et al. [66] give a full description of the First Pass Leakage Profile (FP) method, which this sub-section is based on.

Assuming that backflow during the first pass of contrast agent bolus is negligible ($C_e(t) << C_p(t)$), we obtain from eq. 1.19

$$C_e(t) = K_{fp} \int_0^t C_p(t')dt' \qquad \mathbf{1.20}$$

where K_{fp} is the estimate of K^{trans} from data collected during the first passage of contrast agent bolus. This equation states that the interstitial component of the total tissue concentration is proportional to the integral of the vascular input curve, which has been termed the "leakage profile" (LP)). $C_v(t)$, the intravascular component of the intravoxel contrast agent concentration time-course, can be derived by subtraction of $C_e(t)$ from $C_t(t)$ as given by eq. 1.19. The FP technique uses an iterative approach to improve estimates of the decomposition of the total tissue concentration, $C_t(t)$, into its interstitial and intravascular components, $C_e(t)$ and $C_v(t)$ respectively, using a time-course shape analysis.

The analysis technique for T_1-weighted dataset is graphically represented by the flowchart in Figure 1.4, and the individual steps are described in detail as follows [66].

(a) The T_1-weighted gradient recall echo (T1W-GRE) images acquired with variable flip angles are used to derive 3D parametric intrinsic tissue R_{10} using a Lavenberg-Marquardt non-linear least square fitting routine.

(b) 4D parametric maps of $C_t(t)$ are calculated using the 3D R_{10} and the 4D T1W-GRE dynamic series.

(c) $C_p(t)$ curves are obtained for each patient from voxels (usually in the vertical part of the superior sagittal sinus (SSS)). Details of the 3D R_{10} mapping and the acquisition of the plasma contrast agent concentration time-curve function (PCCF) are described in [43].

(d) The ratio of steady state $C_p(t)$, marked by the beginning of the recirculation of the contrast agent bolus, to the peak value of $C_p(t)$, which is termed the "recirculation to peak ratio" (RPR), is measured from the PCCF curve. This value is employed later in the analysis process.

(e) Measured $C_p(t)$ curves are used to calculate the tumour LP using eq. 1.21 below. Practically, LP time course curves (LP(t)) are calculated from data that includes two sampling points after the onset of recirculation, to ensure computational stability. Only calculation of LP(t) uses these additional time points to avoid erroneous undersampling of the first pass bolus.

$$\mathrm{LP}(t) = \int_0^t C_p(t')dt' \qquad \mathbf{1.21}$$

where $0 \le t \le T_{\mathrm{rR}}$. T_{rR} is the time of the beginning of the recirculation phase identified from the PCCF.

(f) The $C_p(t)$ data is fitted with a gamma-variate density function concatenated with a steady state concentration. The extended first pass LP is then calculated using a five point Newton-Cotes numerical integration method.

(g) Voxelwise automatic decomposition of the tissue residue function into intravascular and extravascular components is then performed using the following steps (see Fig. 1.4).

Step 1. An initial estimate of tumour volume transfer constant between blood plasma and extravascular extracellular space, $K_{\mathrm{fp,i=0}}$, is obtained by fitting the calculated leakage profile to the $C_t(t)$ of the tumour voxel (equal to the tissue residue function) based on eq. 1.20. The Lavenburg-Marquardt non-linear least square routine is employed to fit the leakage profile to the data. In order to minimise the effects on the fitting process of intravascular contrast agent bolus passage, the individual standard deviation array used in the Lavenberg-Marquardt routine is weighted to ensure that the points at which the vascular input function comes into steady state dominated the fitting. The $C_t(t)$ illustrated in Fig. 1.4 shows that the weighting given to the sampling points in the time series effectively eliminates the impact of the first pass effects on the fitting procedure.

Step 2. An initial estimate of the intravascular component of $C_t(t)$, $C_v(t)_{\mathrm{i=0}}$, can be obtained simply by subtracting the initial estimate of the interstitial component derived in step 1 from $C_t(t)$,

$$C_v(t)_{i=0} = C_t(t) - K_{fp,i=0}\mathrm{LP} \qquad \mathbf{1.22}$$

The peak value of $C_v(t)_{\mathrm{i=0}}$, $P_{v,\mathrm{i=0}}$, is measured and the recirculation of the intravascular component estimated as the product of $P_{v,\mathrm{i=0}}$ multiplied by RPR, based upon the assumption that all vessels will exhibit the same RPR.

Step 3. $\mathrm{K_{fp}}$ is estimated by subtracting the contribution of recirculation of contrast agent through the intravascular compartment, calculated in step 2, from $C_t(t)$ and refitting the resulting curve ($C_t(t)_{\mathrm{d}}$). This fitting was also weighted to allow the steady state part of $C_t(t)$, after the onset of recirculation of contrast agent bolus, to dominate the fit:

$$C_t(t)_d = C_t(t) - P_v\mathrm{RPR} \qquad \mathbf{1.23}$$

where P_v is the peak value of the intravascular contrast agent concentration time course curve for each voxel.

Step 4. Steps 2 and 3 are repeated in an iterative fashion to optimise the separation of intravascular and extravascular contrast agent effects. The criterion for convergence is that the interval of two successive estimations of $\mathrm{K_{fp}}$ is smaller than a predefined threshold value, ε (= 10^{-4} min^{-1} usually).

Step 5. Voxelwise relative cerebral blood volume (rCBV) maps, corrected for the effects of contrast agent leakage into the interstitial space ($\mathrm{rCBV_{T1,corrected}}$), are then calculated by

$$\mathrm{rCBV_{T1,corrected}} = \int_0^{t=T_{rR}} C_v(t)dt \qquad \mathbf{1.24}$$

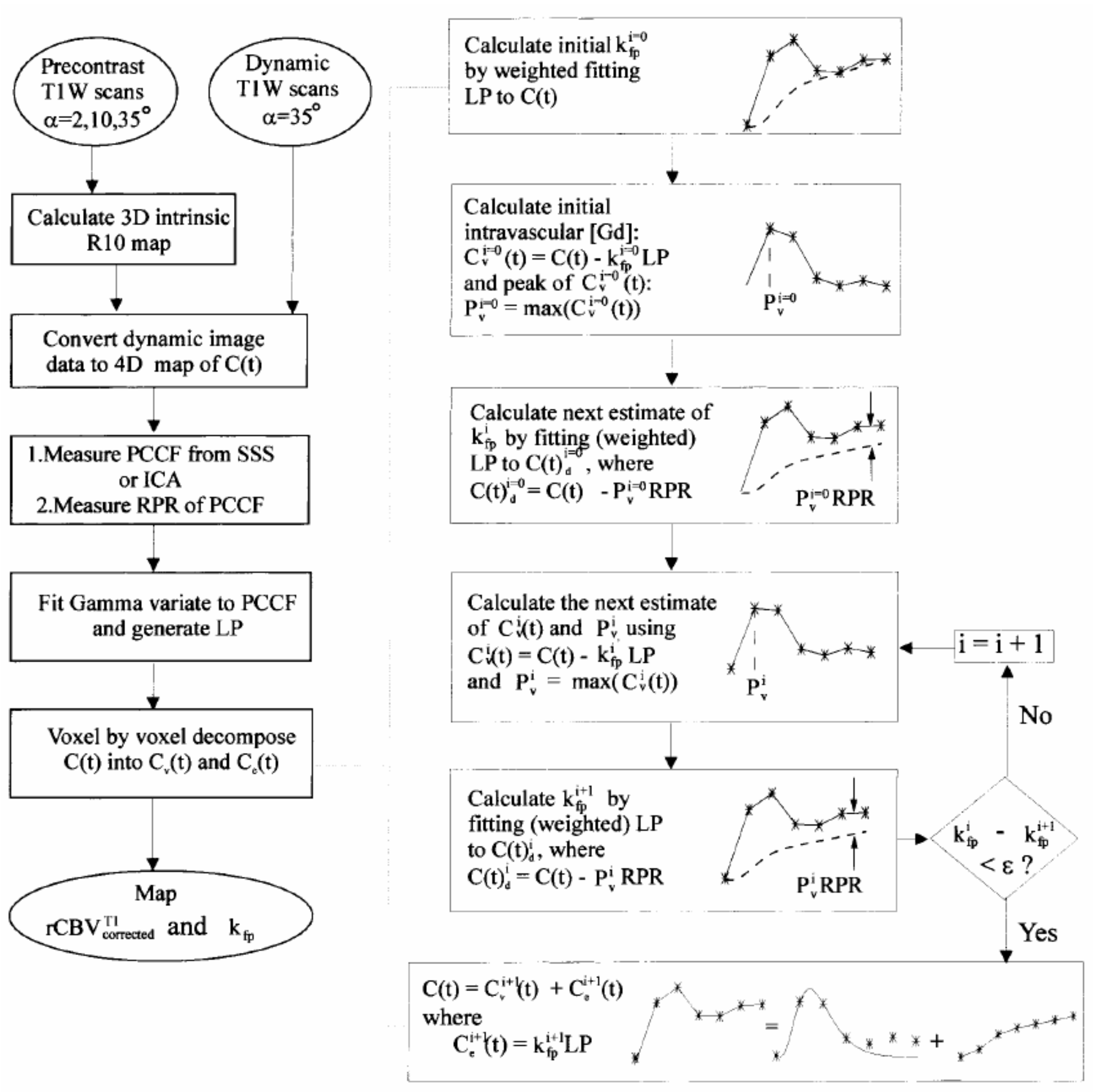

Figure 1.4. Flowchart showing the algorithmic treatment of the data to derive maps of blood volume and trans-endothelial volume transfer constant. To the right is an enlargement showing the decomposition of contrast agent concentration curves in detail. Abbreviations: CA = Contrast agent; $C(t)$ = Intravoxel CA concentration time-course curve; $C_e(t)$ = Interstitial component of $C(t)$; $C_v(t)$ = Intravascular component of $C(t)$; $C(t)_d$ = $C(t)$ with recirculation contribution removed; $C_p(t)$ = Plasma CA concentration time-course curve in a large blood vessel (≡ PCCF); $k_{\mathrm{fp}} \equiv K_{\mathrm{fp}}$; LP = Leakage profile (≡ LP(t), integral of $C_p(t)$); $\mathrm{rCBV}^{\mathrm{T_1}}_{\mathrm{corrected}}$ = Relative cerebral blood volume calculated from T_1-weighted (T1W) dynamic images corrected for extravascular CA leakage; PCCF = Plasma contrast concentration function; P_v = Peak value of $C_v(t)$; RPR = Ratio of the magnitude of steady state $C_p(t)$ to the peak value of $C_p(t)$; SSS = Superior sagittal sinus. Taken from [66].

1.6 ROLE OF DCE-MRI AND MODELLING IN ONCOLOGY MANAGEMENT AND DRUG DEVELOPMENT

1.6.1 Why correlations may exist between histological grading and pharmacokinetic parameters

Histopathological grading, according to WHO, is related to malignancy [11]. It is recognised that angiogenesis is generally more potent in more malignant tumours. Since microvascular endothelial permeability is promoted by VEGF, which stimulates angiogenesis, then it is expected that more malignant tumours will exhibit microvasculature with high endothelial permeability. But is this biological link necessarily true? More malignant tumours have clearly reached their state through angiogenic processes to support their nutrient and gas exchange requirements to sustain their size (when over 1 mm in diameter) and continued growth. Thus, a grade IV glioma may no longer need to release as much VEGF to stimulate angiogenesis as would a grade III or grade II glioma that was becoming more aggressive.

Measurement of blood volume on the other hand may give a direct index to the grade of a tumour. This is because blood volume is related to microvascular density. The more malignant a tumour is the more vessels it will have had to produce to support its development to that aggressive stage. Therefore measured blood volume may be expected to reflect malignancy and therefore may reflect histological grade.

Basically microvascular endothelial permeability measurement may be considered as snapshot of a tumour's present angiogenic state whereas blood volume measurement gives a history of how angiogenic the tumour has been. We have looked in detail at the relationship between permeability and blood volume and histological grade in Chapter 3.

1.6.2 Extra information gained from parametric maps as compared to histological biopsy samples

Biopsy samples taken from tumours for histopathological grading are prone to many errors. One error concerns the actual grading of the tumour. The biopsy sample taken may not be representative of the most malignant part of the tumour, and therefore histological grading may be underestimated leading to inappropriate treatment for the tumour. Another error arises in the histopathological grading of the sample itself. Grading a tumour sample is a very subjective technique, with the result that different pathologists can give variable gradings to the same sample. Also different centres have different standards for doing this.

Whereas taking a biopsy sample is a very invasive and risky procedure, MR imaging is not. Physiologically related parameters can be generated as cross-sectional maps from DCE-MRI data, allowing the assessment of a tumour's condition *in vivo* and non-invasively. With some derivable parameters, such as blood volume, showing a correlation with histological grade, parametric maps could be used to actually grade tumours based on the highest grade present, and guide surgical resection and/or radiotherapy beams so that the most aggressive tumour areas are targeted.

We have looked at the use of blood volume maps for surgical and therapy planning procedures and our study is presented in Chapter 4.

1.6.3 Function of DCE-MRI and parametric mapping in evaluations of anti-tumour drugs

This sub-section is based on [26], which has been written at our centre.

Whilst quantification of contrast agent kinetics in absolute physical terms apparently promises inter-study comparability, in practice this is rarely the case, although intra-study and, to a lesser degree, same-model inter-study comparisons are more likely to be valid. For example, a transfer coefficient K derived by a particular model will rarely be directly comparable to K derived using another. There is also a wide range of data-imposed limitations that can lead to differences in results, including temporal resolution [61], T_1 contrast dynamic range [67] and spatial resolution (this can lead to differences in partial volume averaging, which may be a significant issue in very heterogeneous tumours). Therefore, results derived with the same model but under different image acquisition conditions may not be comparable. Perhaps the most significant data-related influences on model output are the ability to quantify T_1 [44, 67, 68] and the ability to measure the arterial input function non-invasively for each patient [45, 68, 69]. Although these measurements are today more practical than previously, due to sequence and hardware improvements, they are still technically challenging to perform accurately and reproducibly.

We have addressed these problems to enable a multi-centre trial of an anti-VEGF anti-body, HuMV833, using DCE-MRI to measure its effectiveness *in vivo* in patients with abdominal tumours. This is presented in Chapter 6.

CHAPTER 2 :

COMPARISON OF K^{trans} MEASUREMENTS OBTAINED WITH CONVENTIONAL AND FIRST PASS PHARMACOKINETIC MODELS IN HUMAN GLIOMAS

This Chapter is a reproduction of [70].

2.1 INTRODUCTION

In the initial stages of a tumour's growth passive diffusion is an adequate mechanism for supplying the metabolites it requires. However, once the tumour reaches a volume of approximately 1 mm^3, passive diffusion becomes inadequate and a blood supply is required to support further tumour growth. Under the influence of hypoxia and hypoglycaemia tumour cells and other tissues secrete cytokines that stimulate the growth of new blood vessels (microcapillaries) – a process known as angiogenesis [3, 71].

Angiogenic neovasculature characteristically exhibits large inter-cellular endothelial fenestrae during the early stages of development resulting in high endothelial permeability and allowing the passage of large molecules and even cells into and from the tumour. This increase in permeability partly reflects vascular immaturity but is largely a direct response to the permeability enhancing properties of angiogenic cytokines [72]. The most active permeability promoter currently described is the angiogenic cytokine Vascular Endothelial Growth Factor (VEGF) [23].

The increased permeability of neoangiogenic vessels allows extravasation of intra-vascular contrast agents (CA) which will be related to the concentration gradient across the endothelial membrane, their molecular size, the surface area of the vascular endothelium to which they are exposed and the endothelial permeability. Rapid imaging of the distribution of contrast media between the intra and extra-vascular spaces using magnetic resonance imaging has been extensively used to establish quantitative techniques for the measurement of contrast agent leakage. In practice it is possible only to measure the transfer coefficient K^{trans} for the passage of contrast from the vessel into the extravascular extracellular space (EES) [7]. Estimation of K^{trans} is based on analysis of temporally acquired contrast enhanced dynamic data using a series of assumptions derived from a pharmacokinetic model of contrast distribution. A number of such pharmacokinetic models have been proposed and applied and the properties of the measured K^{trans} depend on the pharmacokinetic model used in the analysis [52-55]. Typically K^{trans} will be affected by the endothelial permeability surface area product (PS) but will also be flow limited. This means that in circumstances where the supply of blood is adequate to maintain intravascular CA concentrations, despite the leakage of contrast into the EES, K^{trans} will reflect PS. Where blood flow is low, the amount of CA that leaks into the EES will depend principally on the rate at which it is supplied to the endothelium and K^{trans} will reflect blood flow. A further problem with many conventional pharmacokinetic analyses is the assumption that the signal change in each voxel reflects only contrast leakage into the EES. In fact many voxels will contain considerable intravascular CA. Where the intravascular CA contribution to signal change is not directly modelled then anomalously high measurements of K^{trans} will be obtained, an artefact which has been referred to as "pseudo-permeability" [43].

In this study we have compared two pharmacokinetic models for the calculation of K^{trans}. The first, a conventionally and widely applied model, is that described by Tofts and Kermode (abbreviated as 'TK', [52]). The second is a more recently described method based on the distribution of contrast during the first passage of the bolus through the enhancing tissue, known as the First Pass Leakage Profile method (abbreviated as 'FP', [9]). Both provide estimates of the volume transfer constant (K^{trans}) but these estimates can be expected to differ due to the differences in the analytical models employed ([73]). The aim of this study is to compare calculated values of K^{trans} using these two alternative pharmacokinetic analyses in a group of patients with cerebral glioma and to compare the differences in the derived measures with those which have been previously predicted by mathematical modelling techniques ([73]).

2.2 MATERIALS AND METHODS

2.2.1 Modelling Theories

A single voxel of enhancing tissue is made up of intravascular plasma space (v_p %), extracellular extravascular space (v_e %) and intracellular space (v_i %), so that $v_p + v_e + v_i = 100\%$. The molecular size of gadolinium-based contrast agents commonly used in magnetic resonance imaging prevents them from passing through the cell membrane. The concentration of contrast in the voxel $C_t = v_p C_p + v_e C_e$ where C_p is the CA concentration in the intravascular plasma space and C_e the concentration in the EES. The general equation for the transfer of contrast agent from the intravascular space to the extracellular space is given by:

$$v_e \frac{dC_e(t)}{dt} = \mathrm{K}^{\mathrm{trans}}\left(C_p(t) - C_e(t)\right) \qquad \mathbf{2.1}$$

Where $\mathrm{K}^{\mathrm{trans}}$ is the volume transfer constant. In normal brain parenchyma $\mathrm{K}^{\mathrm{trans}} \approx 0$, due to the presence of the blood-brain barrier.

Solutions of eq. 2.1 for $\mathrm{K}^{\mathrm{trans}}$ depend on the collection of accurate contrast concentration time course (CCTC) measurements in tissue and an appropriate artery (as a measure of $C_p(t)$). We will use the notation of $\mathrm{K}^{\mathrm{trans}}$ to represent the generic $\mathrm{K}^{\mathrm{trans}}$ measurement as opposed to estimates of it using different models.

A) Tofts and Kermode

The pharmacokinetic model proposed by Tofts and Kermode in 1991 [52] has become the most widely accepted and implemented for estimating $\mathrm{K}^{\mathrm{trans}}$. The factors for this may include the length of time it has been established, the low dependence on scanner hardware performance and the number of parameters it can estimate. However, this model was originally developed for use in multiple sclerosis (MS) lesions where v_p is very small and leakage of contrast from the intravascular to the extravascular extracellular space is much slower without first pass effects, when compared to vascular tumours. Nevertheless this model is used extensively in vascular tumours.

Based on tracer concentration measurements taken from blood samples in earlier work [56], a biexponential decay is assumed to describe the plasma CCTC ($C_p(t)$), such that

$$C_p(t) = D\left[a_1 \exp\left(-m_1 t\right) + a_2 \exp\left(-m_2 t\right)\right] \qquad \mathbf{2.2}$$

where D is the Gd-based contrast agent dose (mM/kg of body mass), a_1 and a_2 are the amplitudes of the exponential components, and m_1 and m_2 are their rate constants.[52]

The solution to eq. 2.1 is then given as a triexponential expression (assuming $v_p = 0$),

$$C_t(t) = D\left[b_1 \exp(-m_1 t) + b_2 \exp(-m_2 t) + b_3 \exp(-m_3 t)\right] \tag{2.3}$$

where $m_3 = \mathrm{K}_{\mathrm{TK}} / v_e$, $b_1 = \mathrm{K}_{\mathrm{TK}} a_1 / (m_3 - m_1)$,

$b_2 = \mathrm{K}_{\mathrm{TK}} a_2 / (m_3 - m_2)$, $b_3 = -(b_1 + b_2)$.

and K_{TK} is $\mathrm{K}^{\mathrm{trans}}$ estimated by the Tofts and Kermode technique.

Our implementation of the technique described by Tofts and Kermode [52] is in-fact a variant of their method, in terms of data collection and analysis. In the original technique a single standard set of values was used for the parameters in the $C_p(t)$ equation, which were determined from the blood sample tracer measurements taken by Weinmann et al. [56]. However, we have fitted the biexponential $C_p(t)$ equation (in a constrained fashion [74]) to the CCTC measured from plasma in purely vascular voxels in a main blood vessel in each subject individually, in an attempt to decrease the intersubject variability and increase the accuracy of K_{TK} estimates. The constraint used was that the sum of a_1 and a_2 in eq. 2.2 must always equal 2.6 mmol/litre, since this is the value expected as the maximum $C_p(t)$ for a contrast medium dose of 0.1 mmol/kg, assuming immediate and complete mixture with blood [56].

B) Li et al.

The model of Li et al. [9] was developed to provide an estimate of K^{trans} from data which could be acquired rapidly within a single breath hold. The model uses only dynamic data collected during the first passage of contrast bolus and the estimate of K^{trans} which results has therefore been called K^{trans}–first-pass (K_{fp}). The model also assumes that voxels within the tissue of interest may contain significant amounts of intra-vascular contrast in large blood vessels. Development of this model was possible largely because of the availability of scanning protocols with far higher temporal resolution than had previously been possible. The observed measurements of CCTC in plasma at high temporal resolution shows that it does not conform to the biexponential decay assumed in the Tofts and Kermode model, but actually exhibits a gamma-variate shape as the contrast bolus passes through a vascular voxel [75]. The analytical model is based on the assumption that in the initial phase of contrast passage C_e will be negligible. Assuming therefore that $C_p >> C_e$ [9], it is possible to simplify equation 2.1 to the form:

$$C_t(t) = \mathrm{K}_{\mathrm{fp}} \int_0^t C_p(t')dt' \qquad \textbf{2.4}$$

Therefore K_{fp} can be estimated by measuring the CCTC in the extracellular space at a certain time-point and the measured integral of the CCTC in the intravascular space up to that time-point. A gamma-variate function is fitted to the CCTC curve in purely vascular voxels, usually within a main blood vessel that is supplying the tissue of interest in order to estimate $C_p(t)$ [9].

The method of Li et al. also includes a mathematical decomposition of the CCTC data from individual voxels into intra- and extra-vascular components. This is done by an iterative mathematical fitting routine which uses prior knowledge of the relationship between peak and early recirculation values of intra-vascular contrast concentration and the known shape of the leakage profile (i.e. the integral of $C_p(t)$) to separate intra vascular and extra vascular contributions to $C_t(t)$. The procedure is detailed in [9].

The area under the first-pass $C_p(t)$ curve has commonly been used to represent the relative blood volume (rBV) in previous studies. However, this approach ignores the errors introduced by contrast leakage, which will erroneously increase the apparent rBV. Using the model of Li et al. [9], 3D leakage-free $\mathrm{CBV}_{\mathrm{T}_1}$ (cerebral blood volume from T_1-weighted data) maps, denoted as $\mathrm{CBV}_{\mathrm{T}_1}$_corrected, are generated using the following relationship,

$$CBV_{T_1}\_corrected = \frac{\int_0^T \left[C(t) - \mathrm{K_{fp}} \cdot \int_0^t C_p(t')dt' \right] dt}{\int_0^t C_p(t')dt'} \qquad \mathbf{2.5}$$

From this point onward, we will refer to $\mathrm{CBV}_{\mathrm{T}_1}$_corrected as simply $\mathrm{CBV}_{\mathrm{T}_1}$.

2.2.2 Deriving Contrast Concentration from MR Signal

In order to obtain contrast concentration measurement from T_1-weighted MR signal, the following method was employed, for both models.

Maps of intrinsic longitudinal relaxation rate ($R_{10} \equiv 1/T_{10}$) were calculated by a fitting process using pre-contrast T_1-FE (T_1 field echo) signal at three different flip angles: 2°, 10° and 35° [43].

4D (*x*, *y*, *z*, *t*) post-injection longitudinal relaxation rate {R_1(t)} maps were calculated for each T_1-weighted dynamic phase using signal intensity data from pre- and post-contrast T_1-FE images {S(t) – S(0)} at a flip angle of 35° [43].

Then 4D Gd-based contrast concentration {C(t)} maps were calculated from the 4D R_1(t) maps using,

$$C(t) = \frac{R_1(t) - R_{10}}{r_1} \qquad \textbf{2.6}$$

where r_1 is the relaxivity of the Gd-based contrast medium. For Gd-DTPA-BMA, relaxivity was determined experimentally *in vitro*, $r_1 = 4.39\ s^{-1}mM^{-1}$ (at 37°C and in a magnetic field of 1.5 T) [9, 43]. This was used as an approximation to the *in vivo* value.

2.2.3 Clinical Imaging

Twenty-three patients with gliomas were included in the study. All patients gave informed consent. Central Manchester Healthcare NHS Trust and Salford Royal Hospitals NHS Trust medical ethical committees approved the study and the guidelines set by the medical ethical committee of Erasme Hospital were adhered to. Surgical biopsies for histopathological analysis were taken from all tumours. All patients were treated with steroids prior to scanning but none were receiving any other treatment. The histological grading and demographic data are shown in Table 2.1.

Imaging was performed on a 1.5 tesla MR system (Philips Medical Systems, Best, The Netherlands) using a birdcage head-coil. A 3D T_1-FFE (T_1 fast field echo) scanning sequence was applied, with an image matrix of 128 × 128 pixels and 25 slices in the axial plane. The field of view used was 230 mm, and a slice thickness of 6 mm with 3 mm overlap (Fourier interpolation), resulting in an effective slice thickness of 3 mm. TR was set at 4.2 ms, and TE at 1.2 ms.

The same method was used for calculation of baseline T_1 measurements for both models [9, 43] (a modification of the original method given in [52]). Three pre-contrast data sets were acquired for baseline T_1 calculation using 3D radiofrequency spoiled T_1-weighted field echo acquisitions at flip angles of 2°, 10° and 35°. This was followed by a dynamic contrast-enhanced acquisition series at a flip angle of 35°, consisting of 120 scans with a temporal spacing of approximately 5 seconds. Gadolinium-based contrast agent (Gd-DTPA-BMA; Omniscan™, Amersham Health AS, Oslo, Norway) was injected as a bolus over 4 seconds at a dose of 0.1 mmol/kg of body weight.

The TK model uses all dynamic scans acquired to generate the parametric maps, whereas the initial 20 dynamic scans are used by the FP model.

All imaging data were transferred from the Scanner to an independent workstation (Sun Microsystems, Palo Alto, CA) for analysis. Analysis was carried out with software written in-house using IDL (Interactive Data Language®, Research Systems Inc., Boulder, CO, USA).

A vascular input function ($\equiv C_p(t)$) was measured from the vertical part of the superior sagittal sinus on the middle slice of the scanned volume for every patient data set and for both models (whereas a standard vascular input function was assumed in [52] originally). Even though the vascular input function is meant to be obtained from a vessel feeding the tumour (i.e. an artery), we have used the descending portion of the superior sagittal sinus (SSS) vein in the brain for inter-patient consistency because supplying arteries (such as the internal carotid arteries) are not clearly visible in all patient data sets. Also the CCTC curve in the SSS seems to have a similar shape (in terms of width and height) as an arterial vessel and the appearance time delay is corrected for [9].

ROIs were drawn on image slices to include only the enhancing portion of the tumours in the parametric measurements, which was done by an experienced radiologist (T.A. Patankar). The regions were drawn on at least three consecutive slices through the middle of the tumour volume.

The TK model generated maps of K_{TK} and v_l (v_l is the term originally used by Tofts and Kermode and is equivalent to the term v_e later described by the Consensus Workshop on terminology) [7, 52]. The FP model generated maps of K_{fp} and CBV_{T_1}. To compare the behaviour of the two models in the whole brain, scattergrams were produced relating pixel values of K_{TK}, K_{fp} and CBV_{T_1} from whole slices through the middle of a tumour. K_{TK}, K_{fp} and CBV_{T_1} measured within enhancing tumour do not exhibit normal distributions. Thus to make the statistical analysis sounder we have taken the median values for these.

2.3 RESULTS

Figure 2.1 shows an image from a slice acquired through the middle of a high grade glioma in the anterior frontal lobe. This is a post-injection contrast enhanced T_1-weighted dynamic image taken during the first passage of contrast bolus. Enhancement of the superior sagittal sinus and intracerebral arteries is clearly seen, as is the typical rim enhancement of the glioma tumour tissue.

Figure 2.2 shows parametric maps from a patient with a high grade glioma. Fig. 2.2(a) shows the K_{TK} map generated with our variant TK model. Since this image contains some very high values, in the order of 10^5 min^{-1}, a threshold has been applied to exclude all values above 1.2 min^{-1} [45]. Figures 2.2(b) and 2.2(c) are K_{fp} and CBV_{T_1} maps generated using the FP method (abbreviated as K_{fp}). Direct comparison of the K_{TK} and K_{fp} maps demonstrates significant differences in the distribution of values within the tumour. In addition the K_{TK} map demonstrates areas of high values within the normal brain, which would not be expected in the presence of an intact blood-brain barrier. In contrast the K_{fp} shows uniformly low values within normal brain with high values seen only in the tumour and the choroid plexus. Furthermore, comparison of K_{TK} and K_{fp} with the CBV_{T_1} map shows that the distribution of K_{TK} and CBV_{T_1} map is very similar. These findings were typical of those seen in other cases.

Figure 2.3 shows a series of pixel-by-pixel scattergrams comparing the distribution of values within the parametric maps shown in Figure 2.2. The plot of K_{fp} against K_{TK} in Fig. 2.3(a) shows close correlation between the two but the value of K_{fp} is consistently smaller than that for K_{TK}. There are also a large number of pixels, which fall outside the area of correlation with very low K_{fp} values but higher values of K_{TK}. The plot of CBV_{T_1} against K_{TK} in Fig. 2.3(b) also shows a highly correlated distribution of pixels at high values of both K_{TK} and CBV_{T_1}, which is not seen in a similar plot of K_{fp} against CBV_{T_1} (Fig. 2.3(c)). In this plot pixels with high values of CBV_{T_1} (vascular density) demonstrate low values of K_{fp}.

Figure 2.4 shows the anatomical distribution of correlated and non-correlated values of K_{TK} and K_{fp} based on the pixel-by-pixel scattergram shown in Fig. 2.3(a). The correlated values of K_{TK} and K_{fp} are identified as a yellow overlay on the scattergram in Fig. 2.4(a) and on the greyscale CBV_{T_1} image in Fig. 2.4(b). Pixels with low values of K_{fp} but high values of K_{TK} are identified in blue on the scattergram in Fig. 2.4(c) and on the greyscale CBV_{T_1} image in Fig. 2.4(d). It can clearly be seen that poor correlation occurs in pixels that represent major blood vessels where the true K^{trans} value should be zero.

Figure 2.5 shows a plot of the median values of K_{TK} against K_{fp} from each tumour volume. The highly heterogeneous nature of the gliomas makes the use of mean values and standard deviations of the distribution inappropriate and we have therefore used the median measurement to represent the distributions of K_{TK}, K_{fp} and CBV_{T_1}. Regions of interest data have also been processed to exclude zero values, which represent fit failures. Comparison of median values of K_{TK} and K_{fp} (Fig. 2.5) shows that measures of K_{TK} are significantly higher than comparable values of K_{fp} (Wilcoxon's $Z = -4.197$, $p < 0.001$). Despite this there is a significant correlation (Spearman's rho = 0.650, $p < 0.01$) between median values of K_{TK} and K_{fp} although several outliers exist which are characterised by very high values of K_{TK} compared to K_{fp}. Median values of K_{TK} and K_{fp} also correlate with CBV_{T_1}, being stronger with K_{fp} (rho = 0.610, $p < 0.01$) than with K_{TK} (rho = 0.470, $p < 0.05$).

2.4 DISCUSSION

As interest in quantitative imaging of the microvasculature continues to grow, a bewildering variety of imaging and analysis approaches have been described. This profusion of techniques underlines the fact that no ideal method exists for the quantitative description of microvascular characteristics. Faced with this potentially confusing situation it is important that the methodology for studies using these techniques is based on careful understanding of their relative strengths and weaknesses. These can be partly appreciated by direct modelling approaches using mathematical simulation [73] or Monte Carlo modelling techniques [76] to explore the expected relationships between true and derived values for specific parametric variables. Equally important are methodological studies, like the one presented here, which test the modelling predictions in actual data. The final choice of imaging and analysis approach must be based on clear understanding of the physiological parameters which are of importance in a specific study (e.g. blood flow, endothelial permeability, etc.), which combination of imaging protocol and analysis technique will most accurately provide measurements reflecting those parameters and a number of pragmatic considerations such as the capability of the scanning system, the size of the area to be imaged and temporal resolution required.

In this study we have compared two distinctive data analysis approaches for the measurement of the volume transfer coefficient (K^{trans}) [7] between plasma and extravascular extracellular space (EES) for a small molecular weight gadolinium based contrast agent. The motivation for this type of study derives from increasing understanding that the behaviour of many types of pathological tissues, particularly tumours, depends on the development of an adequate vascular supply and microvascular environment to support tissue growth. This developing neovasculature typically shows disorganised vascular structure, increased vascular density and abnormal increases in microvascular endothelial permeability due to local effects of angiogenic cytokines. The measurement of endothelial permeability (P) or of endothelial permeability surface area product (PS) is therefore of considerable interest as a possible surrogate indicator of angiogenic activity with potential applications in clinical practice and in the area of drug development. In practice the measurement of P or PS is extremely difficult since the efflux of contrast from vessels is flow limited. This means that the efflux rate of contrast will be directly related to PS only in cases where the rate of delivery of contrast (blood flow, F) is sufficiently high that trans-endothelial leakage does not cause significant decrease in the vascular contrast concentration either in the voxel of interest or in other voxels subsequently supplied by the same vessels. Although it is theoretically possible to model the effects of flow and therefore extract direct estimates of PS [6] this increases the demands on the curve fitting optimisation routines used in the analysis making the derived parameters far more sensitive to the effects of local minima, covariance errors and therefore to the effects of poor signal to noise ratio [76]. As a result of these problems the majority of studies use simpler estimates of K^{trans}, which, like those employed here, will be flow limited. The effect of this is that K^{trans} estimations may reflect local blood flow, PS or a mixture of these factors.

The TK and FP models employed in this study both provide measurements of the volume transfer constant, which are referred to as K_{TK} and K_{fp} respectively. Both techniques have been used in clinical and antiangiogenic drug development studies [65, 77]. However we have shown that these measurements differ considerably, both in magnitude and distribution, due to differences in the analytical processes. There are three major differences between the TK and FP analysis techniques, which may be expected to influence calculated values of transfer coefficient. Firstly, improved temporal resolution on modern scanners has shown that the shape of the CCTC curve in the vascular plasma space does not in-fact follow a smooth biexponential function, as determined by Tofts and Kermode [52], but is actually made up of a number of “phases”. Intravenously injected contrast causes the greatest increase in local T_1-weighted signal — the first pass peak — as the contrast bolus first passes through the vessel of interest. The recirculation peak is a relatively much smaller increase in vascular T_1-weighted signal as the contrast bolus passes through the vessel of interest a second time having lost much of its volume through leakage into peripheral tissues and having mixed and dispersed throughout the intravascular space. After this the vascular signal increase becomes less distinct with each pass of the bolus as CA continues to mix throughout the circulating plasma volume. The FP model addresses the true structure of the vascular CCTC, fitting the $C_p(t)$ curve only to the first pass phase of the plasma CCTC curve [9, 66] giving a realistic description of the intravascular compartment. In our modified implementation of the TK model we have used the contrast-enhanced image data we have acquired to measure the vascular input function (VIF) separately in individual patients, whereas the original implementation of this model assumed a standard VIF in all subjects. However, whichever approach is taken, the use of a biexponential model for contrast concentration changes in the vascular compartment is clearly an oversimplification. The use of a biexponential function was originally described by Tofts and Kermode and was based on collection of serial blood samples after intravenous injection as well as observations from dynamic MRI data. The temporal resolution of both these approaches was far lower than that offered by modern dynamic MRI and made detection of the short-lived first pass peak impossible. The large fluctuations of contrast concentration during the first 20 seconds of contrast passage were therefore averaged to give a small number of very high readings so that the measured concentration time course data conforms to a biexponential [78]. Consequently, the CCTC during the first passage of the contrast bolus will be variable and dependant on the temporal resolution of the imaging sequence and the best fit of the biexponential function is to the vascular CCTC points after the recirculation phase [78].

The second major difference between the TK and FP models is the assumption in the TK model that all contrast related signal changes within a tissue voxel result from extravasated contrast within the EES, because the vascular space in MS lesions is known to be very small. In practice the signal change in many voxels will result largely or entirely from contrast in the intravascular extracellular space (v_p), which corresponds to plasma. The original TK model makes no attempt to model this contribution although an upper threshold value in the region of 1.2 min^{-1} [45] may exclude values which result from intravascular contrast in the measurement voxel. This gives rise to artificially elevated values of K^{trans} in voxels with significant intravascular contrast, an effect which has been referred to as “pseudopermeability” [43]. The FP model attempts to deal explicitly with the contribution of intravascular contrast in each voxel by decomposition of the CCTC into intra- and extra-vascular components generating separate CCTC data for intra- and extra-vascular contrast agent.[9, 66]

The third major difference between the techniques is the assumption made in the FP model that backflow of contrast from the EES into the plasma space is negligible [9, 66]. This assumption is based on the fact that the first pass analysis technique only uses data collected during the first 20 seconds after the arrival of contrast within the measurement voxel and commences at a time when there is no contrast in the EES. It allows simplification of the pharmacokinetic model on which the analysis relies. In practice this assumption is incorrect and Monte Carlo modelling has demonstrated that the FP approach results in a systematic and reproducible underestimation of true values of K^{trans}, which is proportionately greater at higher values.

Modelling studies [73, 76] therefore predict three major differences between the estimated values of K_{TK} and K_{fp}. Firstly, the presence of intravascular contrast within a tissue voxel will give rise to erroneously elevated values of K_{TK} (pseudopermeability). Secondly, where the contribution of intravascular contrast agent is negligible and values of true K^{trans} are low then the TK model will produce unstable estimations due to covariance errors in the fitting procedure and these will be greatest where the signal-to-noise ratio (SNR) is poor. In addition the TK model increasingly overestimates K_{TK} at low values and breaks down completely as true K^{trans} approaches zero. Under the same circumstances the FP model will produce accurate measures of true K^{trans} which are robust to the effects of poor SNR. Thirdly, where the contribution of intravascular contrast agent is negligible and values of true K^{trans} are high then the TK model will produce accurate estimations of true K^{trans} although these will continue to show variation where SNR is poor. Under the same circumstances the FP model will produce systematically repeatable underestimations of true K^{trans} and the magnitude of the underestimation will be proportional to the true value. This underestimation reflects the inability of the first pass model to accurately address backflow of contrast from the EES which is an intrinsic component of the model and which, as described above, arises from the use of an isolated subset of the data which records the first passage of the contrast bolus.

Observations of the experimental data in the present study demonstrate the magnitude of these effects. The most striking difference between K_{TK} and K_{fp} is the variation in absolute values. Comparison of median values for regions of interest shows that the TK technique produces values between 28 and 270 times the values measured with the FP approach and these discrepancies are not related to the magnitude of individual measurements (Fig. 2.5). Examination of pixelwise scattergrams from individual cases (Fig. 2.3) shows a subgroup of pixels with close correlation between K_{TK} and K_{fp} although K_{TK} is still larger than K_{fp} ($K_{TK} = 1.6 \times K_{fp}$, approximately). However the remaining pixels show no such correlation with low values of K_{fp} and high values of K_{TK}. These two populations of correlating and non-correlating pixels represent areas with small and large intravascular contrast components respectively. Comparison of parametric maps shows pixels with low K_{fp} and high K_{TK} correspond to the location of cerebral blood vessels and mapping of these values from pixelwise scattergrams onto maps of CBV confirm this (Fig. 2.4). These erroneous areas of high K_{TK} are also seen within the enhancing portions of the tumours and explain the close agreement between images of K_{TK} and CBV seen in Figures 2.2(a) and 2.2(c). The presence of these areas of pseudopermeability also explains the major discrepancies seen between the median values of K_{TK} and K_{fp} in Figure 2.5.

The accuracy of measured values of K^{trans} by either method cannot of course be assessed from the data presented here. However, as described above previous Monte Carlo modelling studies [73, 76] suggest that for pixels where there is negligible intravascular contrast agent contribution to signal the FP technique can be expected to provide accurate measurements up to a value of approximately 0.2 min^{-1}. Above this value K_{fp} will systematically underestimate true K^{trans}, whilst measurements from the TK model will be increasingly accurate as values rise above 0.1 min^{-1}. In the case of the tumour illustrated in Fig. 2, for pixels with negligible intravascular contrast agent contribution to the signal measured K_{fp} values range from 0 to 0.29 min^{-1} and K_{TK} values from 0 to approximately 0.4 min^{-1}. These observations are in close agreement with the predictions of Monte Carlo modelling [76]. Also, modelling studies can only assess the effect of different vascular input functions (VIF) on the measurements. Previous studies have shown that the use of an inappropriate biexponential model produces significant errors in estimates of K_{TK} derived from the TK technique [78] and that absolute calculated values of K_{TK} will be highly dependant on the temporal resolution with which the VIF data is sampled [74]. One result of this is poor reproducibility of K^{trans}–estimating techniques unless the VIF is standardised by use of modelled or partially modelled data [78]. Where this issue is addressed the reproducibility of K^{trans} estimates becomes acceptable [78] but remains lower than the reproducibility of estimates of K^{trans} in similar data outside the brain [65, 77].

The TK model can be extended to include a vascular (v_p) term to account for the intravascular contrast agent concentration contribution to the total intravoxel concentration.

Comparison of such an extended TK model with the FP method would be fairer, since the FP model has a vascular term built in. This study was subsequently carried out by Harrer et al. [79]. Also, we constrained the initial amplitude of the TK model's biexponential fit to the VIF in individual patients (see section 2.2.1.A) so as to stabilise its fitting to post-recirculation time points. This constraint caused the very high contrast agent concentration values in the first pass peak to be considerably underestimated by the TK model. However, a biexponential function cannot describe the intricacies of the first pass peak or recirculation phase of the contrast bolus passage and was originally designed with the assumption of immediate mixing of contrast agent with the blood and a smooth biexponential elimination. Such a biexponential decay is only seen in post-recirculation points, hence the good biexponential fit to these points. Allowing the biexponential fitting to the VIF in an unconstrained fashion would reduce the fitting stability.

In conclusion, the FP technique offers a feasible method for generating estimates of transfer constant and blood volume from T_1-weighted contrast-enhanced data, short acquisitions, decreased movement artefacts and improve patient cooperation which is beneficial for clinical implementation. The TK model is easy to implement, produces accurate measurements of K^{trans} in values in excess of 0.2 $mins^{-1}$ however it suffers from major inaccuracies in areas where large volumes of intravascular contrast agent are present giving erroneously high values of TK. Successful use of the TK model in areas of high vascularity and vascular flow will depend on the development of techniques which explicitly model the vascular fraction.

Patient No.	*Sex*	*Age*	*Histological Grade**
1	M	52	IV
2	M	58	IV
3	F	31	II
4	F	46	III
5	M	75	III
6	M	55	IV
7	M	52	IV
8	M	53	III
9	M	53	IV
10	F	63	IV
11	M	45	IV
12	M	54	IV
13	F	71	IV
14	M	64	IV
15	M	69	IV
16	M	69	IV
17	M	50	IV
18	M	55	IV
19	M	65	IV
20	F	56	IV
21	M	36	IV
22	M	47	II[†]
23	F	38	IV

Table 2.1. Patient demography

* Grading according to World Health Organisation (WHO) criteria for histopathological findings of tissue biopsy samples, taken after imaging. In general, glioma grade II = fibrillary astrocytoma; III = anaplastic astrocytoma; IV = glioblastoma multiforme. † is an oligodendroglioma, but has been included

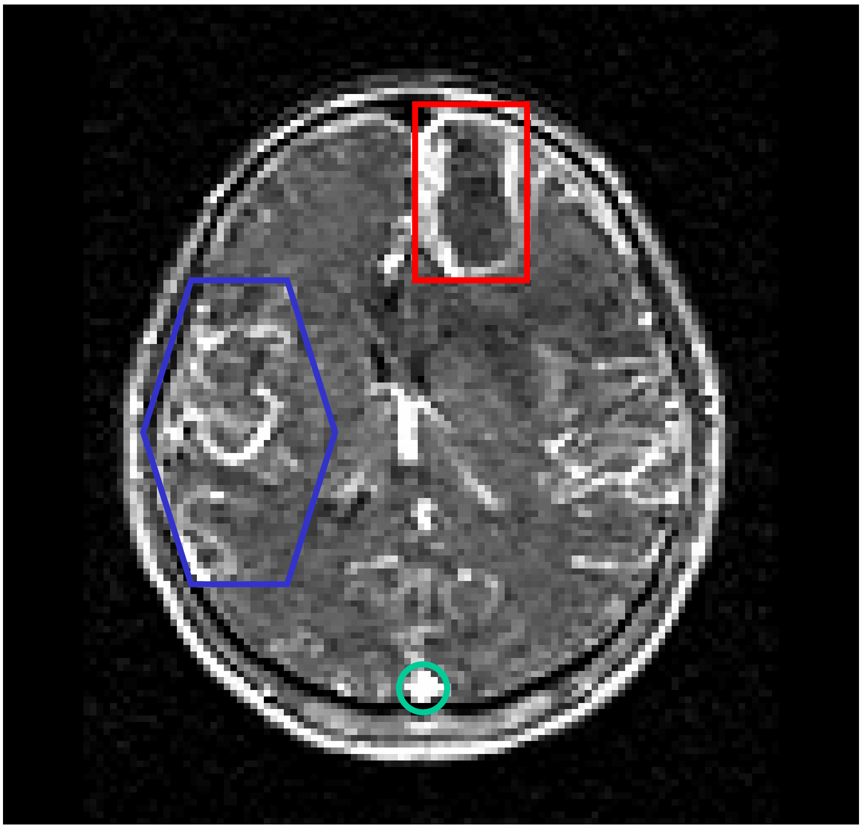

Figure 2.1. Post-contrast brain image showing enhancement of a high grade glioma (red) and of major blood vessels (superior sagittal sinus (green) and internal carotid arteries (blue))

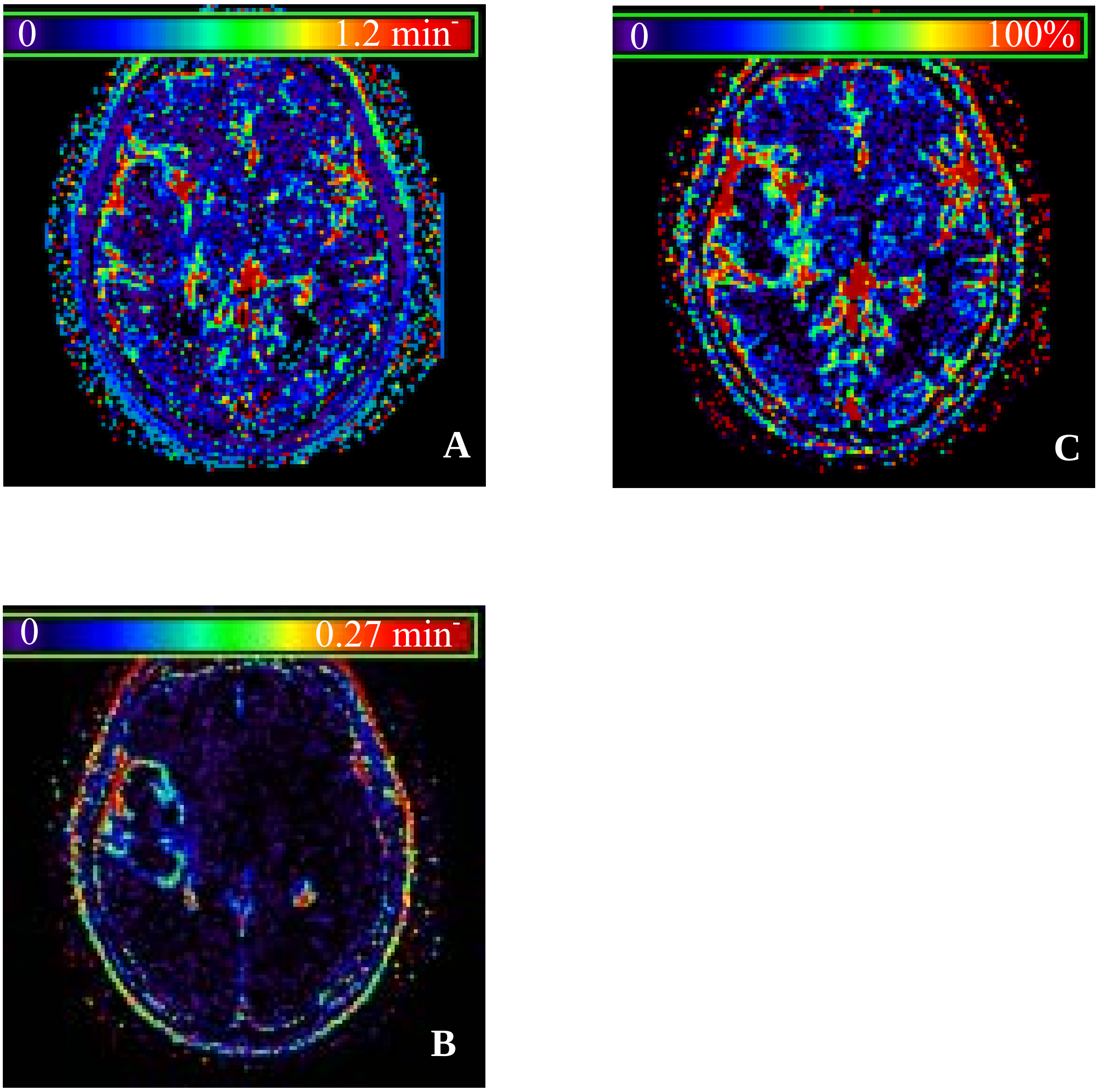

Figure 2.2. Maps generated from T_1-weighted fast field echo contrast-enhanced dynamic data through the middle of a high grade glioma. (a) K_{TK}, (b) K_{fp} and (c) T_1-CBV maps from the FP technique

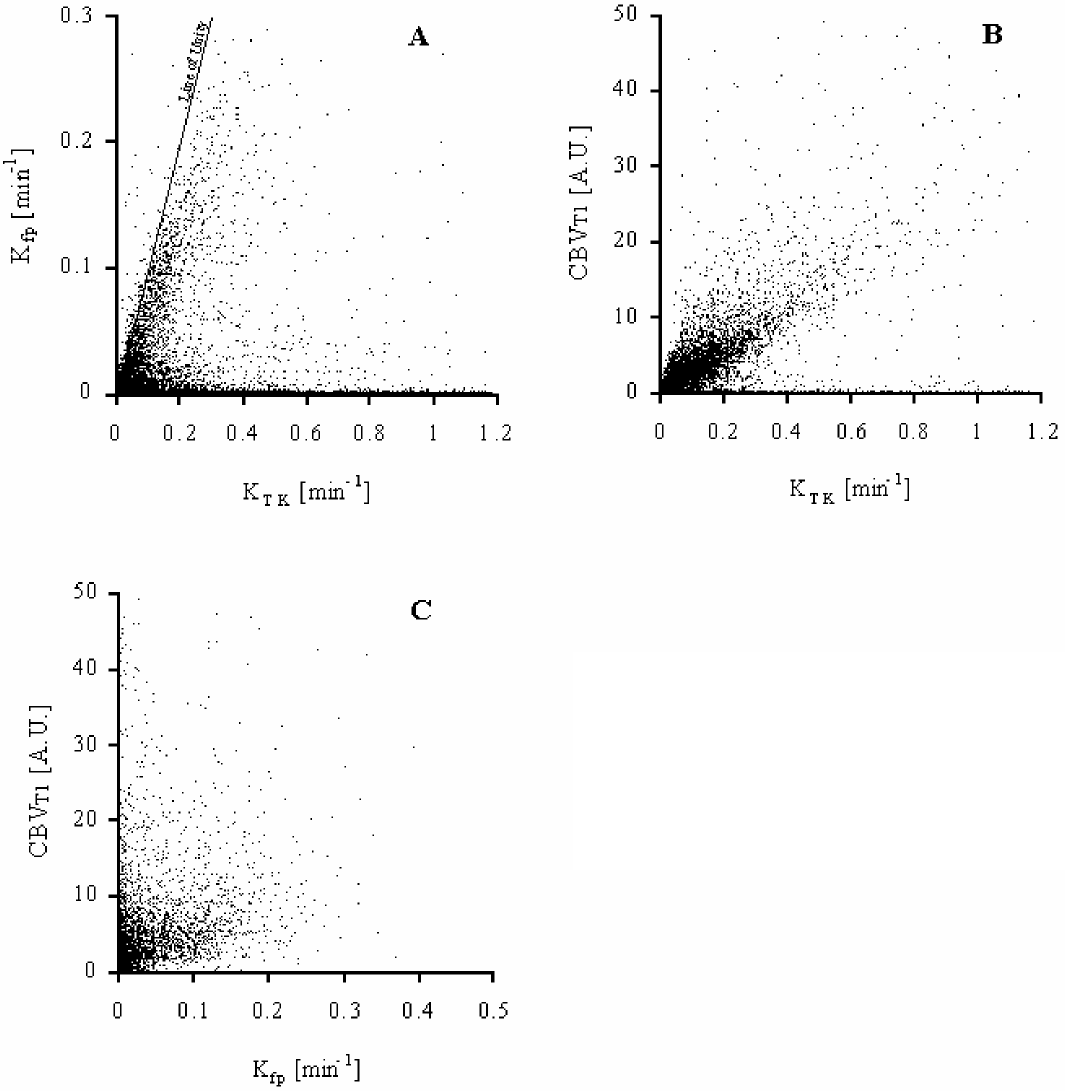

Figure 2.3. Pixelwise scattergrams of a whole brain slice containing a high grade tumour (as shown in Figure 2.2). K_{fp} (Fig. 2.2(b)) against K_{TK} (Fig. 2.2(a)) (a), T_1-CBV (Fig. 2.2(c)) against K_{TK} (b), and T_1-CBV against K_{fp} (c)

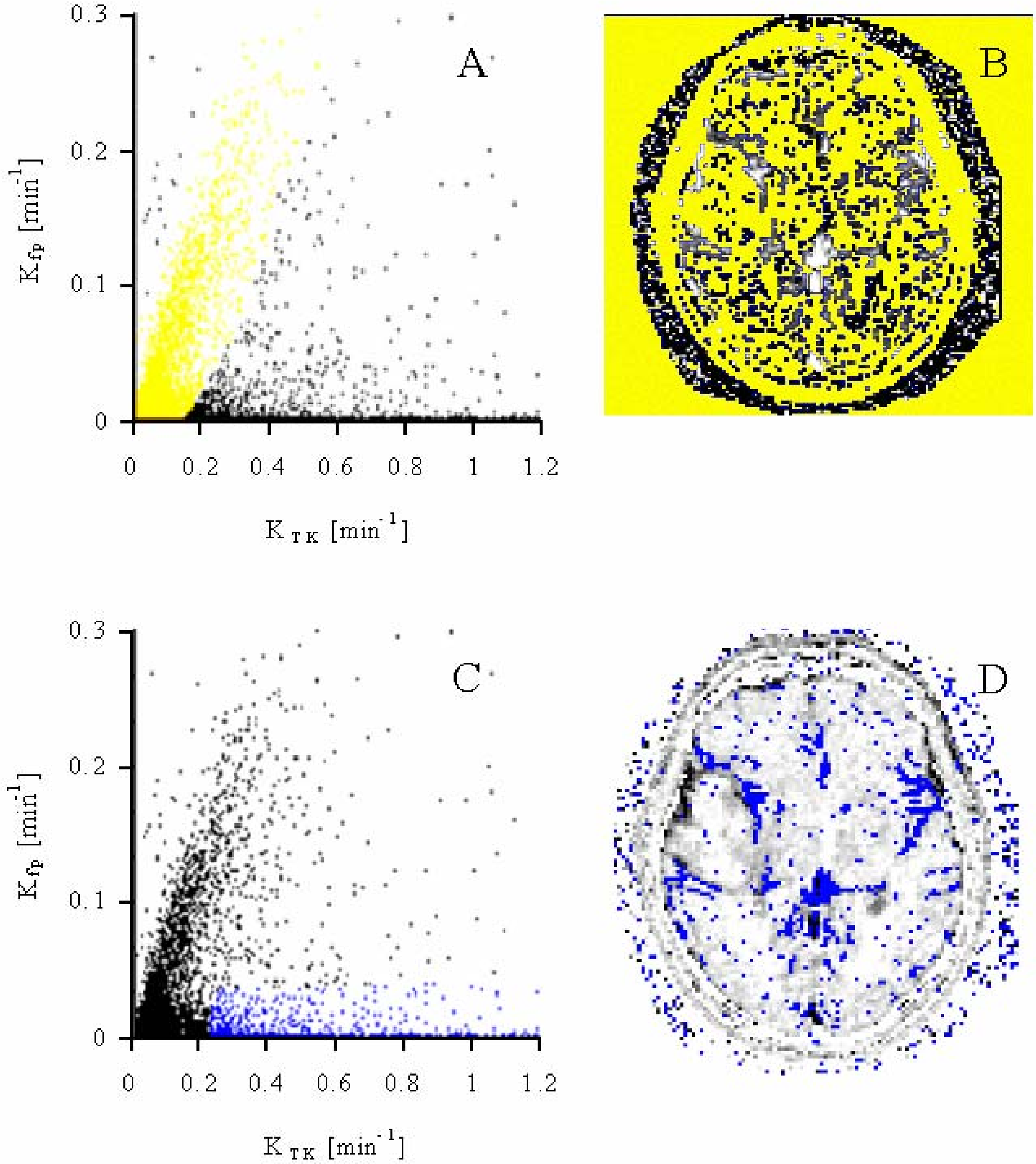

Figure 2.4. Mapping of pixels where there seems to be a correlation between values of K_{TK} and K_{fp}, highlighted as yellow pixels on the scattergram (a) and correspondingly highlighted in yellow on the T_1-CBV map (b). Mapping of pixels that show high values of K_{TK} but very low values of K_{fp}, highlighted as blue pixels on the scattergram (c) and correspondingly highlighted in blue on the T_1-CBV map (d)

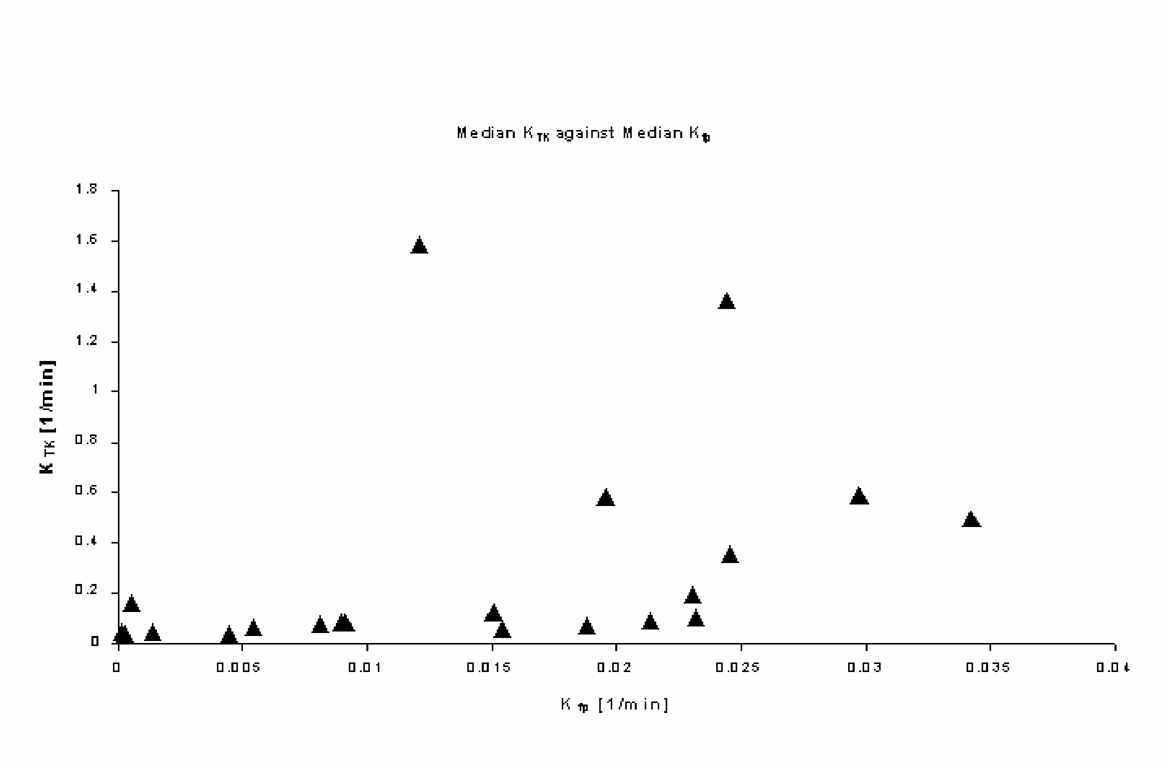

Figure 2.5. Median measurements taken from a region of interest (ROI) drawn around tumour tissue, and only including non-zero pixels. Comparison of the median measurement taken using the same ROI on the K_{TK} maps against the K_{fp}, for all our glioma cases

CHAPTER 3 :

IS THE VOLUME TRANSFER COEFFICIENT (K_{fp}) RELATED TO HISTOLOGICAL GRADE IN HUMAN GLIOMAS?

Co-authors: Tufail F Patankar, Samantha J Mills, Danielle Balériaux, David L Buckley, Geoff JM Parker, Alan Jackson

3.1 INTRODUCTION

Histological grading of glial cell tumours makes an important contribution to determining optimal therapeutic strategy and estimating prognosis. Unfortunately, these tumours, and particularly those of higher grade are histologically heterogeneous and surgical biopsy can lead to acquisition of unrepresentative samples. This has led to widespread use of image-guided biopsy in an attempt to avoid inappropriate classification [80-86].Targeting of enhancing areas within tumours ensures that biopsy material will represent viable tumour. However, areas of most marked enhancement do not appear to correspond specifically to areas of dedifferentiation and several techniques have been developed in an attempt to allow identification of the most dedifferentiated areas within a tumour as biopsy targets. The identification of correlations between imaging based parameters and tumour grade has led many groups to examine the feasibility of non-invasive image based tumour grading [70, 81, 82, 85-90]. The most promising methods for non-invasive grading to date are based on magnetic resonance spectroscopy [83, 91] and dynamic contrast enhanced magnetic resonance imaging (DCE-MRI) [82]. Dynamic acquisition of images during contrast enhancement allows calculation of specific descriptive parameters related to local microvasculature characteristics including cerebral blood volume (CBV). The production of parametric maps of CBV is straightforward and many groups have demonstrated a relationship between CBV and tumour grade [80, 87, 90, 92-96]. Furthermore, regional increases in CBV in high grade glial tumours appear to correlate to areas of histological dedifferentiation. Despite this, estimation of CBV does not allow accurate classification of tumour grade although some authors have quoted diagnostic specificities as high as 79% [80-82, 84, 86, 87, 97, 98]. The relationship between CBV and grade is intuitive since pathological studies demonstrate clear increases in the proportion of blood vessels in higher-grade tumours.

More recently, many groups have described pharmacokinetic analysis techniques to extract other descriptive parameters from DCE-MRI data [7, 43, 66, 99, 100] that include blood flow (F) and microvascular endothelial permeability surface area product (PS). Evidence from modalities such as Xenon-enhanced CT shows a clear relationship between tumour grade and blood flow [101, 102]. There is also a theoretical basis for a relationship between endothelial permeability and tumour grade since high-grade tumours classically express increased levels of the vasoactive cytokine vascular endothelial growth factor (VEGF) which promotes endothelial proliferation and directly increases endothelial permeability. Consequently high grade tumours are characterised by a high proportion of immature and hyperpermeable vessels [103-105]. In practice the separate estimation of F and PS is difficult and most techniques attempt to measure the volume transfer coefficient, K^{trans}, for passage of contrast agent between the blood and the extravascular extracellular space (EES) [7]. The transfer coefficient will be affected by both flow and permeability surface area product, however, since both of these values are expected to increase with increasing tumour grade their effects on measured K^{trans} can be confidently predicted to be cumulative. Consequently, measurements of K^{trans} might be expected to be related to tumour grade and could potentially provide additional information to measurements of CBV. This has led several authors to examine the relationship between the transfer coefficient and tumour grade [81, 88, 89, 106]. However, the results from these studies are conflicting with some showing far weaker relationships between K^{trans} and tumour grade than for CBV and others showing K^{trans} to be strongly related to grade. The reasons for this variability in the results of apparently similar studies have to date been unclear although there is wide methodological variation between them. This study represents an attempt to clarify the potential value of CBV and K^{trans} measurements for classification of cerebral gliomas using a well-validated pharmacokinetic modelling technique and an attempt to explain the apparent contradictions in the literature to date.

3.2 MATERIALS AND METHODS

3.2.1 Clinical Imaging

Thirty-nine patients with clinically suspected gliomas of varying grades were recruited for this study (mean age of 52.9 years (range: 31–77 years), 29 males and 10 females). All diagnoses were histologically confirmed. All patients gave informed consent. The Central Manchester Healthcare NHS Trust and Salford Royal Hospitals NHS Trust medical ethical committees and the ethical committee of Erasme Hospital approved the study. All patients with high grade tumours (grades III and IV) were treated with steroids prior to scanning but none were receiving any other treatment. The histological grading and demographic data are shown in Table 3.1.

Following MR imaging, patients underwent surgery either for tumour resection or biopsy. Histological examination and determination of the grade of tumour biopsy was performed according to criteria set out by the World Health Organisation (WHO) [14].

Imaging was performed on identical 1.5 tesla MR systems (Philips Medical Systems, Best, The Netherlands) using a birdcage head-coil. Routine pre and post contrast clinical imaging was performed according to local protocol. Three pre-contrast data sets were acquired for baseline T_1 calculation using a 3D T_1-FFE (T_1 fast field echo) sequence (TR/TE 4.2/1.2 ms, field of view 230 × 230 mm, imaging matrix 128 × 128, slice thickness 6 mm interpolated to 3 mm, 25 slices) with flip angles of 2°, 10° and 35°. This was followed by a dynamic contrast-enhanced acquisition series at a flip angle of 35°, consisting of 20 volume acquisitions with a temporal spacing of approximately 5 seconds. Gadolinium-based contrast agent (Gd-DTPA-BMA; Omniscan™, Amersham Health AS, Oslo, Norway) was injected as a bolus over 4 seconds at a dose of 0.1 mmol/kg of body weight following acquisition of the ninth image volume.

All imaging data were transferred from the scanners to an independent workstation (Sun Microsystems, Palo Alto, CA) for analysis. Analysis was carried out with software written in-house using IDL (Interactive Data Language®, Research Systems Inc., Boulder, CO, USA). A vascular input function ($\equiv C_p(t)$) was measured from the vertical part of the superior sagittal sinus on the middle slice of the scanned volume for every patient dataset. ROIs were defined by an experienced radiologist (T.A. Patankar and S.J. Mills) on one of the post contrast datasets. The regions were drawn on three consecutive slices through the middle of the tumour volume. Tumour ROIs were defined to contain all visually enhancing components of the tumours and specifically excluded coherent large non-enhancing areas.

3.2.2 Deriving Contrast Concentration from MR Signal

Maps of intrinsic longitudinal relaxation rate ($R_{10} \equiv 1/T_{10}$) were calculated by a fitting process using the pre-contrast T_1-FFE signal at three different flip angles: 2°, 10° and 35° [43].

4D (*x*, *y*, *z*, *t*) post-injection longitudinal relaxation rate $R_1(t)$ maps were calculated for each T_1-weighted dynamic phase using signal intensity data from pre- and post-contrast T_1-FFE images at a flip angle of 35°[43]. Then 4D Gd-based contrast concentration C(t) maps were calculated from the 4D $R_1(t)$ maps using,

$$C(t) = \frac{R_1(t) - R_{10}}{r_1} \qquad \textbf{3.1}$$

where r_1 is the relaxivity of the Gd-based contrast medium. For Gd-DTPA-BMA, relaxivity was determined experimentally *in vitro*, $r_1 = 4.39\ s^{-1}mM^{-1}$ (at 37°C and in a magnetic field of 1.5 T) [9, 43]. This was used as an approximation to the *in vivo* value.

3.2.3 Calculation of K^{trans} and CBV

A) General Theory

A single voxel of enhancing tissue is made up of fractional intravascular plasma space (v_p), fractional extracellular extravascular space (v_e) and fractional intracellular space (v_i), ($v_p + v_e + v_i = 1$). The molecular size of gadolinium-based contrast agents commonly used in magnetic resonance imaging prevents them from passing through the cell membrane. The concentration of contrast in the voxel $C_t = v_p C_p + v_e C_e$, where C_p is the CA concentration in the intravascular plasma space and C_e the concentration in the extracellular extravascular space (EES). The general equation for the transfer of contrast agent from the intravascular space to the extracellular space is given by:

$$v_e \frac{dC_e(t)}{dt} = \mathrm{K}^{\mathrm{trans}}\left(C_p(t) - C_e(t)\right) \qquad \mathbf{3.2}$$

where $\mathrm{K}^{\mathrm{trans}}$ is the volume transfer constant. In normal brain parenchyma $\mathrm{K}^{\mathrm{trans}} \approx 0$, due to the presence of the blood-brain barrier.

B) Leakage Profile Model

The analytical leakage profile model of Li et al. [9] is based on the assumption that in the initial phase of contrast passage C_e will be negligible (which holds if the ratio $\mathrm{K}^{\mathrm{trans}}/\mathrm{v}_\mathrm{e}$ is small in eq. 3.2). Assuming therefore that $C_p >> C_e$ [9], it is possible to simplify eq. 3.2 to the form:

$$C_t(t) = \mathrm{K}_{\mathrm{fp}} \int_0^t C_p(t')dt' \qquad \mathbf{3.3}$$

Therefore K_{fp} can be estimated from the tissue contrast agent concentration time course and vascular input function over a time t representing the duration of the first pass of contrast agent through the tissue. A gamma-variate function is fitted to the contrast agent concentration time course curve in purely vascular voxels, usually within a main blood vessel that is supplying the tissue of interest in order to obtain a regularised estimate of $C_p(t)$ during the first pass [9].

The First Pass Leakage Profile method of Li et al. also includes a mathematical decomposition of the contrast agent concentration time course data from individual voxels into intra- and extra-vascular components. This is done by an iterative fitting routine which uses prior knowledge of the relationship between peak and early recirculation values of intra-vascular contrast concentration and the known shape of the leakage profile (i.e. the integral of $C_p(t)$) to separate intra vascular and extra vascular contributions to $C_t(t)$. The procedure is detailed in [9].

The area under the first-pass $C_p(t)$ curve has commonly been used to represent the relative blood volume (rBV) in previous studies. However, this approach ignores any errors introduced by contrast leakage, which will erroneously increase the apparent blood volume. Using the model of Li et al. [9, 66, 76], 3D leakage-free $\mathrm{CBV_{T_1}}$ (cerebral blood volume from T_1-weighted data) maps, denoted as $\mathrm{CBV_{T_1}}$_corrected, are generated using the following relationship,

$$\mathrm{CBV_{T_1}\_corrected} = \frac{\int_0^T \left[C(t) - \mathrm{K_{fp}} \cdot \int_0^t C_p(t')dt' \right] dt}{\int_0^t C_p(t')dt'} \qquad \textbf{3.4}$$

From this point onward, we will refer to $\mathrm{CBV_{T_1}}$_corrected as simply $\mathrm{CBV_{T_1}}$.

3.2.4 Statistical Analysis

The FP model generates maps of $\mathrm{K_{fp}}$ and $\mathrm{CBV_{T_1}}$. $\mathrm{K_{fp}}$ and $\mathrm{CBV_{T_1}}$ measured within enhancing tumour do not exhibit normal distributions and hence for statistical analysis median values were taken. In addition, we have examined the significance of the value of the 95th-centile (95%) of the distribution for both $\mathrm{K_{fp}}$ and $\mathrm{CBV_{T_1}}$ ($\mathrm{K_{fp}}$(95%) and $\mathrm{CBV_{T_1}}$(95%)).

Comparison between grades for each of the four parametric variables was performed using a one-way analysis of variance (ANOVA) and inter-group comparisons were performed using a post-hoc test assuming unequal variance between the groups (Tamahane) [107]. The correlation between histological grade and median values for each parametric variable was assessed using Spearman's correlation coefficient. In addition, the correlation between each of the parametric variables was measured using Pearson's correlation coefficient. The ability of the parametric variables to distinguish between the tumour grades was assessed using a discriminate analysis using a forward stepwise model. A leave one out cross-validation analysis was also performed to estimate the expected efficiency of diagnostic classification in a larger group.

Separate statistical analysis was performed to examine the difference between high grade (grade III and grade IV) and low-grade (grade II) tumours. The difference between median values for each of the four parametric variables was assessed using a Mann-Whitney U test and the ability of each of the variables to distinguish between high and low grade tumours was assessed using a logistic regression analysis. Finally, receiver operator curve analysis was performed to quantify the ability of each of the parametric variables and of the optimised canonical discriminate function to distinguish between: 1) high and low grade tumours and 2) grade III and grade IV tumours.

3.3 RESULTS

Figure 3.1 and Figure 3.2 show a representative selection of parametric brain images showing cross sections through gliomas of varying histological grade (II (a), III (b), and IV (c)). K_{fp} maps are shown in Fig. 3.1, and corresponding CBV_{T_1} maps are shown in Fig. 3.2. The K_{fp} maps show the clear difference between low (II) and high (III and IV) grades, and heterogeneity within high grade tumour tissue. K_{fp} values within normal brain are zero or consistent with noise. CBV_{T_1} values in grade II tumour tissue are very similar to normal tissue, and are clearly higher and heterogeneous in high grade tumour tissue. Vasculature in normal brain is evident on the CBV_{T_1} maps, especially the superior sagittal sinus and cerebral arteries. The mean value and standard deviation of the distribution of median values from individual tumours for each of the four parametric variables are shown in Tables 3.2A and 3.2B. There was close correlation between measured values of CBV_{T_1} and K_{fp} ($r = 0.688$, $p < 0.001$). There were significant group differences between tumour grades for all four parametric variables (K_{fp}, $K_{fp}(95\%)$, CBV_{T_1} and $CBV_{T_1}(95\%)$; $p < 0.001$). Pairwise comparisons demonstrated significant differences between grades II and III and between grades II and IV for all variables except K_{fp}, which did not show significance in the grade II and III comparison, and between grades III and IV for CBV_{T_1} and $CBV_{T_1}(95\%)$ (Table 3.3). There was a significant correlation between grade and the median values of each of the parametric variables (Figure 3.3, $p < 0.01$). The correlation was greatest for $K_{fp}(95\%)$ ($r = 0.740$, Table 3.4). Discriminate analysis identified a single significant predictive function (C1):

$$C1 = 0.695 \cdot (CBV_{T_1}) + 0.577 \cdot (K_{fp}(95\%)) \qquad \textbf{3.5}$$

values of K_{fp} and $CBV_{T_1}(95\%)$ had no independent predictive value. Figure 3.4 shows the relationship between values of median CBV_{T_1} and $K_{fp}(95\%)$ for all individual cases. The discriminate variables accounted 99.7% of the variance in the model ($p < 0.001$) and the effective classification accuracy is shown in Table 3.5 with a total correct classification of 74.4% of cases. The results of cross-validation analysis showed a decrease in discriminative accuracy (Table 3.6).

3.3.1 Comparison of high and low grade tumours

There were significant differences between high and low grade tumours for all four parametric variables (K_{fp}, $K_{fp}(95\%)$, CBV_{T_1} and $CBV_{T_1}(95\%)$; $p < 0.001$). Logistic regression analysis showed $K_{fp}(95\%)$ and CBV_{T_1} to be independently and significantly related to grade ($p < 0.01$ and $p < 0.05$, respectively).

Table 3.7 and Figures 3.5 and 3.6 show the results of receiver operator curve (ROC) analysis. Figure 3.5 shows the effect of using each individual variable or the discriminate function (C1) in differentiating between high and low grade tumours and Figure 3.6 shows the effect in differentiating between grade III and IV tumours. The area under the ROC curve for high versus low grade was greatest for the discriminate function (0.993). Within the independent parametric variables the area was highest for $K_{fp}(95\%)$ (0.986) although similarly high values were seen for K_{fp} and CBV_{T_1} (0.979 and 0.966, respectively). For discrimination between grades III and IV, CBV parameters were slightly better than the discriminate function.

3.4 DISCUSSION

Several groups have studied the relationship between contrast transfer coefficient and tumour grade in gliomas using MRI [81, 88, 89, 106]. The results of these studies appear contradictory and careful review demonstrates a wide variation in image acquisition protocols, image analysis techniques and statistical analysis approaches. It is important to attempt to clarify the causes of these discrepancies since the potential role, if any, of transfer coefficient measurements in clinical practice remains unclear.

In the current study we have used a pharmacokinetic model based on the first passage of the contrast bolus and first described by Li et al [9, 66, 76].It is a functional model that uses Patlak approach [108]. The model is based on temporal changes in calculated contrast concentration derived from T_1-weighted data and uses a decomposition of the measured data to identify relative contributions from intravascular and extravascular contrast in each pixel. The decomposition step together with the reduction in the number of fitting variables employed in curve fitting stages makes the model highly reproducible and stable to wide variations in signal-to-noise ratio. A major significant drawback with this model is the inherent assumption that no backflow of contrast will occur from the EES into the plasma during the first passage of the contrast bolus. This is untrue in tissues with very high endothelial permeability (> 0.2 min^{-1}) where the ratio of K^{trans} to v_e is high and an underestimation of transfer coefficient values occurs above this approximate threshold [76]. In the current study values of this magnitude were not observed in any individual case and therefore we can reasonably expect the measured values of transfer coefficient and CBV_{T_1} to be representative of true tissue values. The output of the analysis is matched quantitative parametric maps of transfer coefficient (called K_{fp} rather than K^{trans} in order to identify it as the output of a **f**irst-**p**ass analysis technique) and CBV_{T_1}.

We have chosen to examine all tissues within the enhancing component of the tumour for this study and to examine both the median value of the parametric variables extracted from the tumour and their 95th-centile values. Median values of the parameters were chosen since the distribution of pixel values in individual tumours seldom conforms to a normal distribution. The use of 95th-centile values recognises the fact that many distributions show a significant skew with a tail to the right side of the distribution (i.e. an excess of high values), which presumably represents increases in measured parameters in a small sub-population of pixels. The use of the 95th-centile value helps to identify distributions in which the median value is not significantly changed but the presence of small numbers of pixels with increased values gives rise to a large skew in the distribution [109].

Some approaches rely on values calculated from large regions of interest that encompass some or the entire tumour. In some cases this is simply the enhancing component of the tumour whilst other authors include the entire tumour area. The use of data from large regions of interest gives increased signal-to-noise ratio but makes it impossible to examine the effects of distribution patterns of values within the tumour. In contrast, other studies produced parametric images from which measurements are subsequently made. In some studies, such as the one presented here, an attempt is made to represent the distribution of values within the entire enhancing tumour area. In other studies an attempt is made to identify the highest values of individual parameters by use of carefully selected or multiple regions of interest. Direct comparison between measurements from these two sampling strategies is not appropriate. This is the reason we have included centile values for each of the parameters in an attempt to identify the potential significance of changes in the higher end of the distribution curves. Another major difference between studies of this type is the choice of statistical test used to examine the derived values. Authors commonly examine the relationship between individual parameters and grade by measurement of a correlation coefficient. Although correlation coefficients illustrate relationships between grade and measured values they give little or no information concerning the relative discriminative value of individual variables and there are many problems with this approach where data is divided into categories such as histological grade [107]. It is therefore essential that studies of this type should present the results of comparative ROC and discriminative analyses if conclusions are to be drawn concerning the diagnostic value of calculated parameters.

In this study we demonstrated close correlation between measurements of CBV_{T_1} and K_{fp}. All parametric variables discriminated between high and low grade tumours and logistic regression analysis showed that K_{fp}(95%) and CBV_{T_1} were independently related to grade. Optimal differentiation between high and low grade tumours was obtained using a discriminate function which correctly classified 94.9% of cases. Comparison of values across all tumour grades showed that only CBV_{T_1} and CBV_{T_1}(95%) were significantly different between grades III and IV. Discriminate analysis again showed both K_{fp}(95%) and CBV_{T_1} to be significant independent predictors of grade but, classification accuracy was poor.

There have been many studies which have demonstrated a relationship between CBV and tumour grade using susceptibility contrast enhanced (T_2*-weighted) techniques and, despite variations in methodology, these publications are largely in agreement [43, 82, 84, 86, 87, 90, 97, 98, 106, 109, 110]. Previous publications examining the relationship between grade and transfer coefficient have described widely varying findings. The first such study published in 2000 used a low temporal resolution (26 sec) T_1-weighted acquisition [89]. The analysis of dynamic data was based on signal intensity changes and no attempt was made to correct for baseline T_1 values or to calculate contrast concentration changes during the study. The regions of interest studied included all of the enhancing tissue within the tumour and found significant differences in permeability between all pairs of grades and a high correlation between grade and permeability ($r = 0.76$). This study showed no statistical difference of fractional blood volume between grades although there was a weak correlation ($r = 0.39$). There are two significant potential methodological problems with this analysis technique [89]. Firstly, the use of signal intensity variations rather than calculation of contrast concentration changes and, secondly, the use of very low temporal resolution. The relationship between contrast agent concentration and signal intensity on T_1-weighted images is nonlinear[67]. This is particularly problematic in areas of very high concentration where the signal intensity will be significantly lower than would be expected with a linear relationship. The form of arterial input function used may have been flawed as high concentrations are typically seen in large vessels so that the use of signal intensity changes to provide an arterial input function are likely to systematically overestimate the contrast changes taking place in the vascular tree. In addition, contrast agent was administered as a short lived bolus with duration shorter than the sampling time of the acquisition sequence. This makes accurate measurement of the peak arterial contrast value impossible and can lead to considerable variation in measured arterial input functions [78]. The combination of these effects can be predicted to produce considerable variability, which would affect CBV estimations and therefore also introduce bias into estimates of the transfer coefficient. The failure of the study to demonstrate relationships between CBV and tumour grade contradicts a large body of previous work based principally on susceptibility based techniques which have repeatedly demonstrated such a relationship to exist. It is possible that any genuine contribution from CBV was factored into the transfer coefficient estimate due to the low temporal resolution data acquisition. The second group to specifically address the relationship between endothelial permeability and grade used a high temporal resolution (1 sec) T_1-weighted acquisition and analysed the data by applying a multi-compartment pharmacokinetic model to the calculated contrast agent concentration data [81, 111]. The analysis included all the tumour tissue including non-enhancing components and produced parametric images of the variables. The analysis was based on histogram distribution in individual pixels within the tumour and specific measured values of individual parameters were not presented. However, the authors stated that there was a strong discriminative relationship between estimates of CBV and grade that could be used to classify individual tumours using arbitrary thresholds. In this study of 24 gliomas, defining any tumour with more than 5% of voxels with values of over 5%

CBV as grade III and any tumour with more than 7% of voxels with values over 8% CBV as grade IV resulted in 83% of cases being classified correctly. However, there was no relationship between permeability related parameters and grade. This may be due to the fact that the model applied to the data was non-standard, and that the form of arterial input function used was flawed, with no evidence of a first pass peak. In 2002, Provenzale et al [88] studied 22 patients with glioma using a T_2*-weighted dynamic imaging spin echo sequence with a temporal resolution of 1.5 seconds. The data were analysed using a model previously described by Weisskoff [100] to produce parametric maps of transfer coefficient. The data was analysed by sampling the tumour with multiple regions of interest to find a mean and the highest measurable transfer coefficient value. These authors demonstrated significant differences in transfer coefficient between low and high grade tumours with the greatest difference being seen in maximum of values ($p = 0.018$). This provided a positive predictive value of 90% and a negative predictive value of 75% for a transfer coefficient value of 0.03. The authors did not measure nor comment on blood volume effects. Unfortunately the accuracy of decomposition of intra- and extravascular contrast agent contributions from T_2*-weighted dynamic dataset are related to the extraction rate of contrast agent into the tumour tissue. In the presence of large extraction fractions, the original authors expect the model to be less appropriate [100]. The presence of significant T_1 contributions to signal intensity represents the worst case scenario where parts of the tumour with highly permeable capillary beds show significant T_1 related enhancement during the first passage of the contrast bolus [112]. Weisskoff et al. suggested that in such cases the use of techniques to minimise T_1-related enhancement would be required in order to more aggressively correct the contrast agent leakage [100]. In fact the original description of the technique employed pre-enhancement techniques to reduce T_1 related effects and the authors suggested that higher dose pre-enhancement might be needed where contrast extraction fraction was high. In the study by Provenzale et al. no pre-enhancement was utilised so that T_1 effects should be expected and will be proportionately greater in higher grade tumours where leakage is likely to be higher [112]. This would have the effect of reducing apparent values of CBV while increasing measures of K^{trans} in high grade, enhancing, tumours. The latest study to examine the relationship between microvascular parameters and tumour grade in gliomas was published in 2004 [106]. This large study of 73 patients with primary gliomas used a high temporal resolution (1 sec) T_2*-weighted acquisition sequence. CBV estimates were calculated using standard techniques for T_2*-weighted images which have previously been shown to produce strong correlations between CBV and grade. Estimates of transfer coefficient (K^{trans}) were produced using a standard two-compartment model applied to the same data. Measurements were extracted from parametric images using multiple regions of interest targeted at areas of significant enhancement and the highest of four measurements was selected. The authors demonstrated significant differences in CBV between all pairs of grades but differences between K^{trans} were found only between grades II and III and grades II and IV. There was a significant correlation between CBV and grade (r =0.817) and a much weaker relationship between K^{trans} and grade (r= 0.266). Logistic regression to identify predictors of high versus low grade tumours showed only CBV to be significantly predictive. Once again there are potential methodological problems associated with the approach taken in this study. The use of T_2*-weighted imaging again raises the problem of competing T_1-weighted effects in enhancing tissue as were discussed above [112]. Once again no attempt was made to reduce these effects by pre-enhancement or by use of sequences insensitive to T_1. Secondly, the elevation of apparent contrast concentration following the passage of the bolus is attributed entirely to contrast agent leakage and takes no account of the possibility of residual intravascular contrast. In practice the authors acknowledge that blood flow can be extremely variable and heterogeneous in any given region of a tumour and that K^{trans} may be underestimated if extremely slow flow is present such as might be seen in areas of low perfusion pressure or torturous vessels. We have previously examined the relationship between tumour grade and the early contrast recirculation phase on T_2*-weighted images using a measurement of the integral of contrast concentration in the early recirculation phase to the regional blood volume [109, 112]. This relative recirculation parameter shows clear relationship to tumour grade in gliomas with increased skewness of the distribution at higher grade and we attributed this relationship to retention of contrast within tortuous poorly perfused vessels which are typically seen in high grade tumours. This raises the possibility that some of the early recirculation phase changes on T_2*-weighted acquisitions reflect not only permeability but also retained intravascular contrast.

Although it is clear that DCE-MRI techniques offer considerable promise in clinical practice there are clearly considerable problems associated with their implementation and interpretation. Estimation of CBV from T_2*-weighted images represents an example of a technique that is relatively robust to image acquisition protocol and analysis technique with a large body of published work generally showing good agreement. More complex analysis strategies inevitably involve a series of assumptions relating to the cause of observed signal changes and the underlying physiological mechanisms that control contrast distribution and signal formation. The studies described here show quite disparate results almost undoubtedly as a result of variations in methodology. There seems little doubt that there is a strong relationship between CBV and tumour grade in gliomas since there is a large published body of work derived from both T_2*- and T_1-weighted data [84-87, 97, 113-115]. These studies use direct measurement of CBV by integrating the contrast concentration time course curve and this same method was used with similar results in the study of Law et al. described above [106]. The current study and the work of Ludeman et al. [81, 111] used pharmacokinetic modelling of T_1-weighted data and were also able to demonstrate this relationship. The relationship between K^{trans} and grade remains less clear. The studies of Ludeman et al. [81, 111] failed to demonstrate any relationship between K^{trans} and grade, and the study of Law et al. [106] showed only a weak relationship. However, the current study and the study described by Provenzale et al. [88] both identified K^{trans} as a significant discriminator between high and low grade gliomas. Each of the imaging and analysis techniques employed in these studies is associated with specific potential disadvantages. This is also true of the technique we have used which is known to underestimate K^{trans} where the contrast extraction fraction is high. However the method has been tested extensively both by establishment of reproducibility coefficients and by Monte Carlo modelling to identify the magnitude of errors induced by the use of low signal-to-noise data and by the assumptions in the modelling itself [9, 66, 76]. The studies suggest that within the measured range of K_{fp} identified in the current study the model can be expected to be accurate and reproducible. The technique also offers significant advantages since data acquisition can be performed in under a minute and can be used in conjunction with a breath hold technique [65].

In conclusion, we have demonstrated strong relationships between both CBV and K^{trans} and histological grade in gliomas. Either CBV or K^{trans} or a combination of the two, show good discriminative power in distinguishing between low and high grade tumours with diagnostic sensitivity and specificity in excess of 90%. The identification of grade III and grade IV tumours is relatively poor with diagnostic sensitivity of only 68% and specificity of 62%.

Patient No.	*Sex*	*Age*	*Histological Grade**
1	M	52	IV
2	M	58	IV
3	F	31	II
4	F	46	III
5	M	75	III
6	M	55	IV
7	M	52	IV
8	M	53	III
9	M	53	IV
10	M	45	IV
11	M	54	IV
12	F	71	IV
13	M	64	IV
14	M	69	IV
15	M	69	IV
16	M	50	IV
17	M	55	IV
18	M	65	IV
19	F	56	IV
20	M	47	II[†]
21	F	46	II[†]
22	M	44	II[†]
23	F	34	II[†]
24	M	45	II
25	F	42	II
26	M	38	III
27	M	46	III
28	M	53	IV
29	M	58	IV
30	M	48	IV
31	F	40	II[†]
32	F	60	IV

33	M	55	IV
34	M	72	II
35	M	61	IV
36	M	50	IV
37	M	77	IV
38	M	42	III
39	F	33	II

Table 3.1. Patient demography
* Grading according to World Health Organisation (WHO) criteria for histopathological findings of tissue biopsy samples, taken after imaging. In general, glioma grade II = fibrillary astrocytoma; III = anaplastic astrocytoma; IV = glioblastoma multiforme. † is an oligodendroglioma, but has been included

WHO Histological Grade	*No. of Patients*	K_{fp} $[min^{-1}]$		CBV_{T_1} [%]	
		Mean	*SD*	*Mean*	*SD*
II	10	0.000712	0.000712	1.284	0.75
III	6	0.0185	0.0102	2.995	0.44
IV	23	0.025	0.0177	4.022	1.352

Table 3.2A. Means and standard deviations (SD) of K_{fp} and CBV_{T_1} median measurements in gliomas grouped by WHO grade (assuming that the median values are normally distributed)

WHO Histological Grade	*No. of Patients*	K_{fp} (95%) $[min^{-1}]$		CBV_{T_1} (95%) [%]	
		Mean	*SD*	*Mean*	*SD*
II	10	0.018	0.0126	4.63	2.47
III	6	0.073	0.033	8.83	1.64
IV	23	0.112	0.055	12.24	4.37

Table 3.2B. Means and standard deviations (SD) of K_{fp}(95%) and CBV_{T_1}(95%) measurements in gliomas grouped by WHO grade

		Grade III	*Grade IV*
Grade II	CBV_{T_1}	< 0.001	< 0.001
	K_{fp}	NS*	< 0.001
	$CBV_{T_1}(95\%)$	< 0.01	< 0.001
	$K_{fp}(95\%)$	< 0.05	< 0.001
Grade III	CBV_{T_1}		< 0.05
	K_{fp}		NS
	$CBV_{T_1}(95\%)$		< 0.05
	$K_{fp}(95\%)$		NS

Table 3.3. Post-hoc pairwise comparisons between grades (Tamahane test)
*NS = not significant

	Spearman's rho	*Significance*
CBV_{T_1}	0.719	< 0.001
K_{fp}	0.656	< 0.001
$CBV_{T_1}(95\%)$	0.718	< 0.01
$K_{fp}(95\%)$	0.740	< 0.001

Table 3.4. Correlation values (Spearman's rho) and significance of the correlation between each of the four parametric variables and grade

Predicted *Observed*	*Grade II*	*Grade III*	*Grade IV*
Grade II	9 (90)	1 (10)	0
Grade III	0	6 (100)	0
Grade IV	0	9 (39.1)	14 (60.9)

Table 3.5. Classification results using the canonical discriminate variable [C1 = $0.695 \cdot (CBV_{T_1}) + 0.577 \cdot (K_{fp}(95\%))$]. Numbers in brackets represent percentages of correct classification. Total number of cases correctly classified is 74.4%

Predicted *Observed*	*Grade II*	*Grade III*	*Grade IV*
Grade II	9 (90)	1 (10)	0
Grade III	1 (16.7)	4 (66.7)	1 (16.7)
Grade IV	0	9 (39.1)	14 (60.9)

Table 3.6. Classification results using the canonical discriminate variable [C1 = $0.695 \cdot (CBV_{T_1}) + 0.577 \cdot (K_{fp}(95\%))$] and a leave one out cross validation analysis. Numbers in brackets represent percentages. Total number of cases correctly classified is 69.2%

	High versus Low Grade	*Grade III versus Grade IV*
CBV_{T_1}	0.966 ($p < 0.001$)	0.754 (NS)
K_{fp}	0.979 ($p < 0.05$)	0.551 (NS)
$CBV_{T_1}(95\%)$	0.955 ($p < 0.001$)	0.754 (NS)
$K_{fp}(95\%)$	0.986 ($p < 0.001$)	0.725 (NS)
C1	0.993 ($p < 0.001$)	0.732 (NS)

Table 3.7. Results of the ROC analysis for each individual variable and for the discriminate function C1 in differentiating between low grade tumours (left) and grade III and grade IV high grade tumours (right). The value shown are the area under the ROC curve and the significance of the relationship in brackets

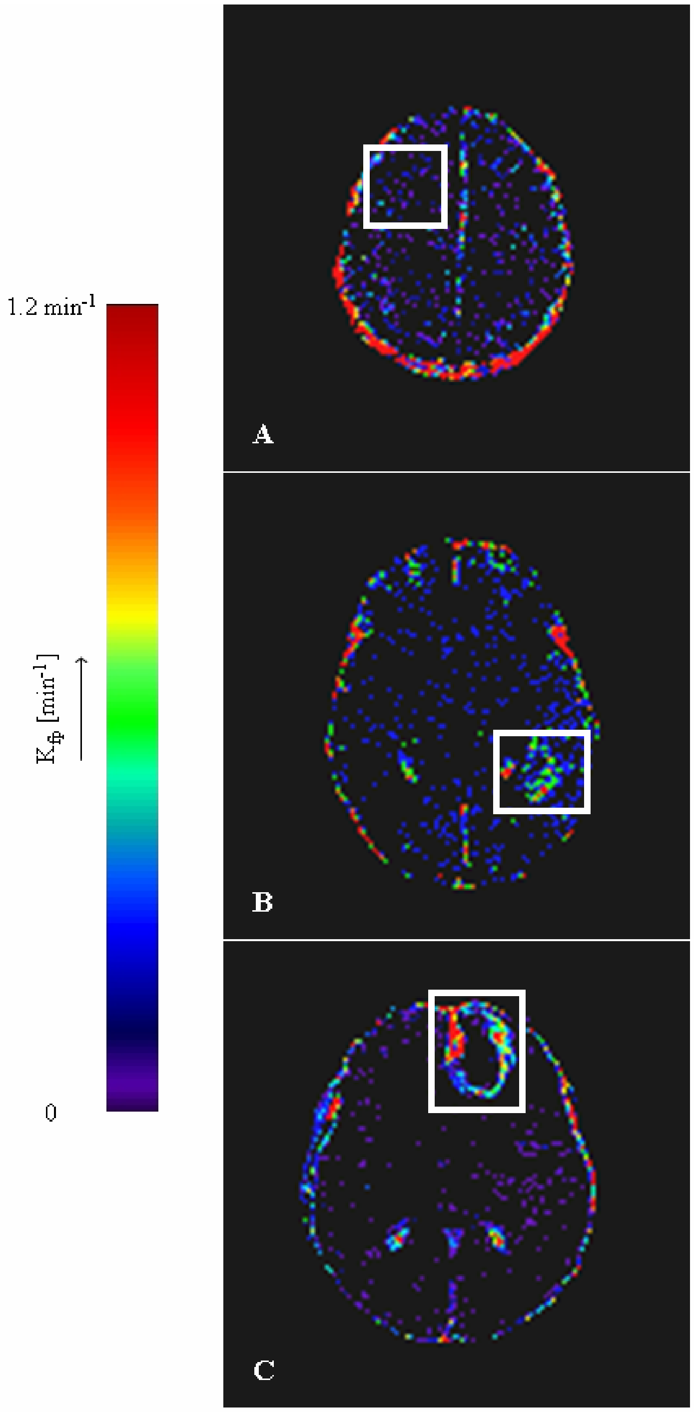

Figure 3.1. Representative K_{fp} maps from (A) a grade II fibrillary astrocytoma, (B) a grade III anaplastic astrocytoma, and (C) a grade IV glioblastoma multiforme. The white boxes enclose the tumour area in each image. Note that vasculature does not appear in these maps, and K_{fp} values in normal brain are insignificant and consistent with noise. The K_{fp} values in the grade II tumour (A) are insignificant corresponding to the lack of enhancement with contrast. The high-grade-defining necrotic core is clearly evident in the middle of the tumour in (C). The heterogeneity of K_{fp} is clearly evident in the enhancing tumour portion in (B) and (C).

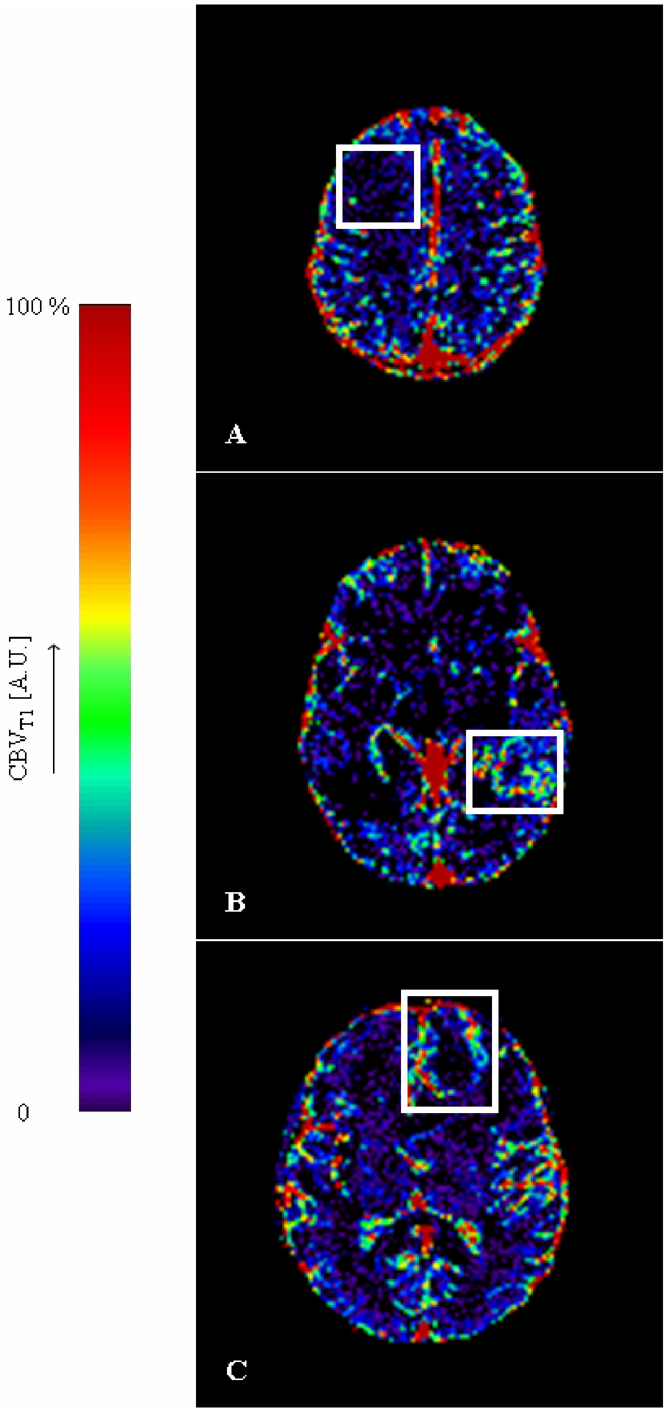

Figure 3.2. Representative CBV$_{T_1}$ maps from (A) a grade II fibrillary astrocytoma, (B) a grade III anaplastic astrocytoma, and (C) a grade IV glioblastoma multiforme. The white boxes enclose the tumour area in each image. The normal cerebral vasculature is clearly seen on these maps, particularly the superior sagittal sinus and other major vessels. The grade II tumour in (A) homogeneously shows very low blood volume which is below the measurement accuracy of the technique. The necrotic core is clearly evident in the middle of the tumour in (C). The heterogeneity of CBV$_{T_1}$ is clearly evident in the enhancing tumour portion in (B) and (C), and shows very different distributions to those in Fig. 3.1 (A) and (B).

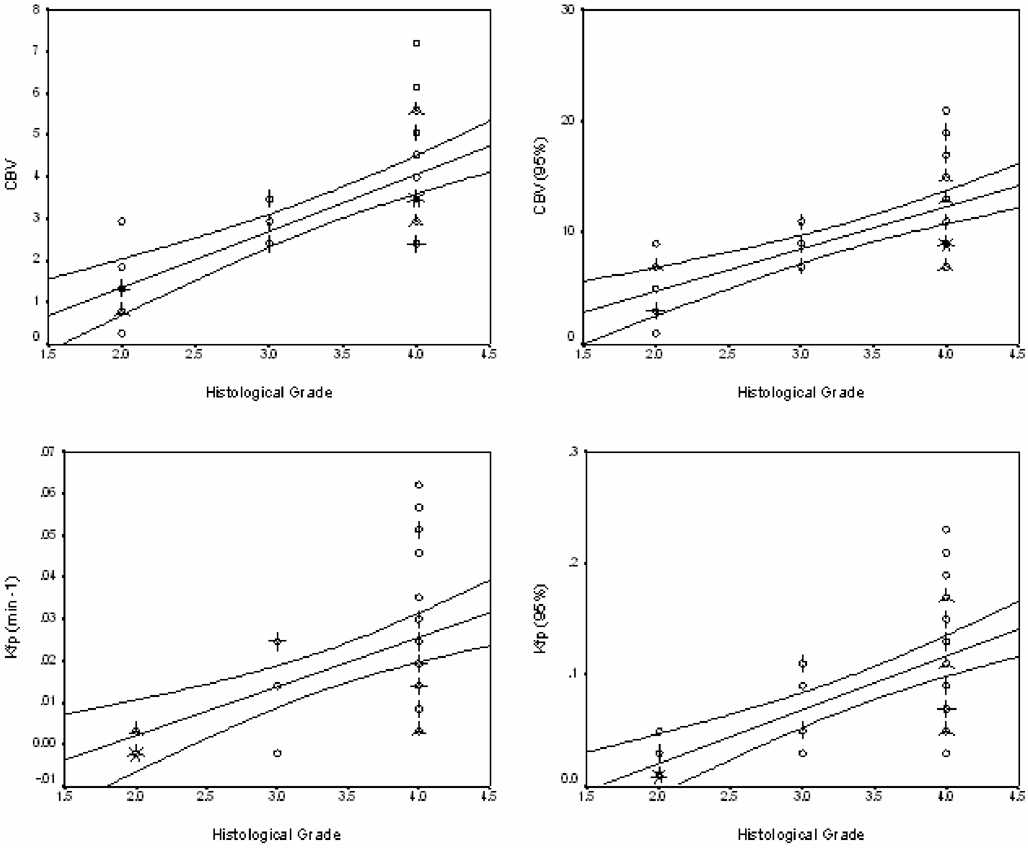

Figure 3.3. Scattergrams showing the relationships between histological grade and median values of K_{fp}, $K_{fp}(95\%)$, CBV_{T_1} and $CBV_{T_1}(95\%)$. Individual cases are indicated by circles, multiple cases are represented by the addition of "petals" to the glyph with the number of petals representing the number of cases. Lines indicate the optimal linear regression fit for the data and the 95th centile confidence limits for the regression fit for the entire data set. The correlation between grade and the median values of each of the parametric variables is significant (K_{fp}, $K_{fp}(95\%)$, CBV_{T_1} and $CBV_{T_1}(95\%)$) [$p < 0.01$].

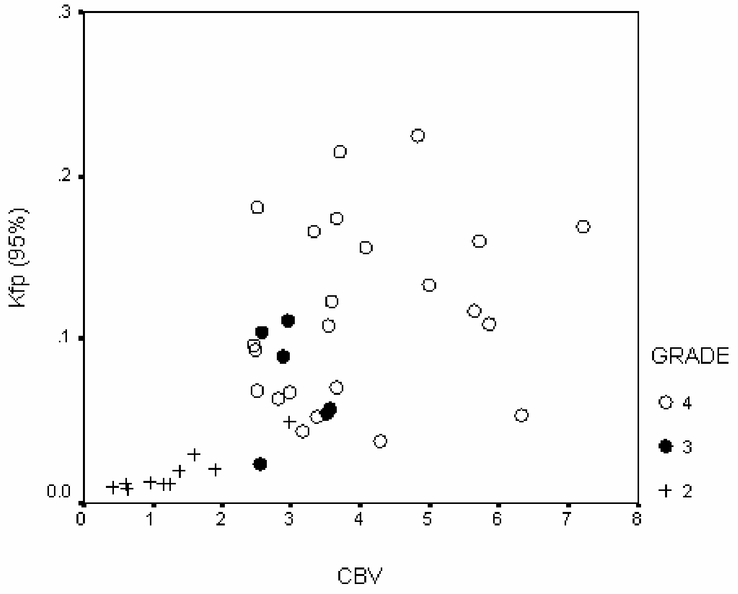

Figure 3.4. Scattergram showing the relationship between values of median CBV_{T_1} and K_{fp}(95%) for all individual cases. The grade II tumours show lower values of both CBV_{T_1} and K_{fp}(95%). Higher values are seen in grade III and IV tumours but there is a considerable overlap in these distributions.

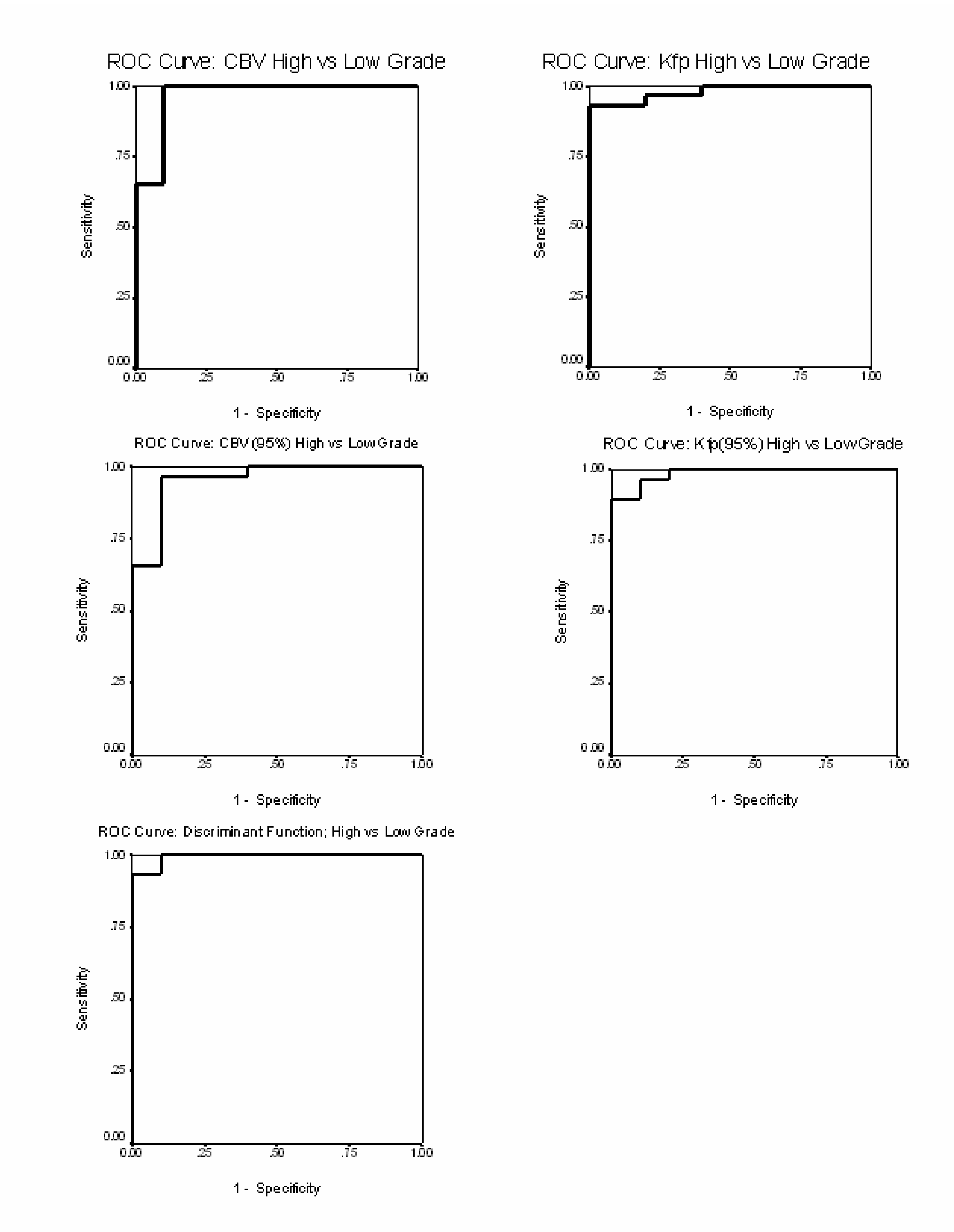

Figure 3.5. Receiver operator curve (ROC) analysis showing effect of using each individual variable or the discriminate function (C1) in differentiating between high and low grade tumours. The area under the ROC curve for high versus low grade is greatest for the discriminate function (0.993). Within the independent parametric variables the area was highest for K_{fp}(95%) (0.986) although similarly high values were seen for K_{fp} and CBV_{T_1} (0.979 and 0.966, respectively) (Areas under the ROC curves are shown in Table 3.7).

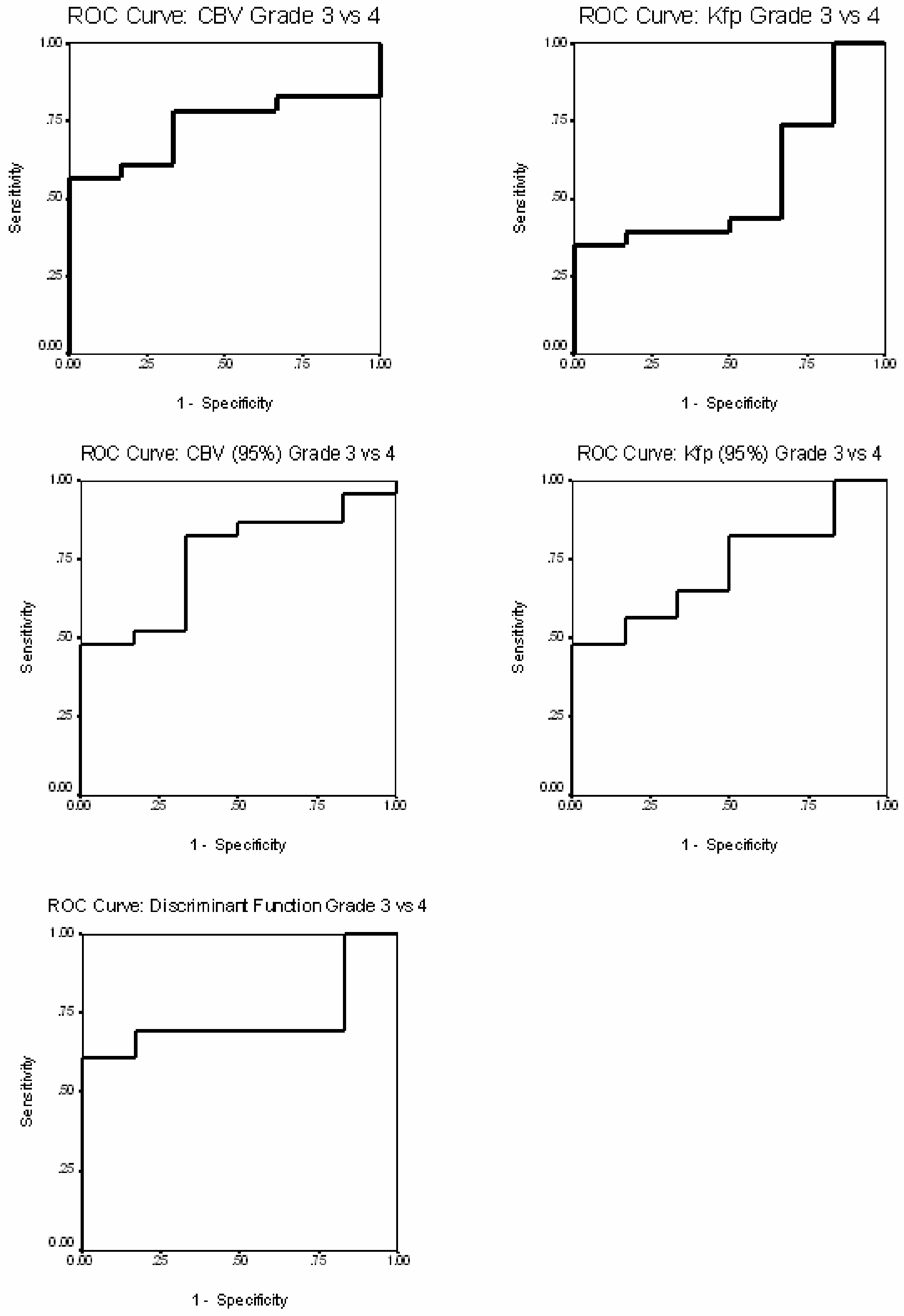

Figure 3.6. Receiver operator curve (ROC) analysis for separation of grade III and IV tumours. Areas under the ROC curves are shown in Table 3.7.

CHAPTER 4 :

COMPARISON OF CEREBRAL BLOOD VOLUME MAPS GENERATED FROM T_2*- AND T_1-WEIGHTED MRI DATA IN INTRA-AXIAL CEREBRAL TUMOURS

Co-authors: Tufail F Patankar, Neil A Thacker, Marietta J Scott, Karl Embleton, Xiaoping Zhu, Kaloh Li, Alan Jackson

4.1 INTRODUCTION

The development of new blood vessels in tumours depends on the process of angiogenesis. Under ischemic and hypoglycaemic challenge developing tumour cells produce cytokines and other vascular mediators which cause sprouting of endothelial cells from local blood vessels and a number of other physiological and developmental changes [2, 116]. These lead to the in-growth of new blood vessels and vascularisation of the tumour. In general terms more aggressive, rapidly growing tumours will provide a stronger angiogenic stimulus and are characterised by increased microvascular density (MVD) on histological examination. A clear relationship between microvascular density and prognosis has been demonstrated for many tumour types which encouraged the development of non-invasive imaging based techniques that try to duplicate these measurements *in vivo* [117-119]. The best documented of these is the measurement of regional cerebral blood volume (CBV) using dynamic contrast enhanced MRI. Several groups have demonstrated a clear relationship between CBV and histological grade in cerebral glioma and in a number of other tumour types [43, 81, 82, 94, 110, 113, 120-124]. Areas of increased CBV within the enhancing components of gliomas correspond well with areas of increased fluorodeoxyglucose uptake on PET and with histological evidence of tumoral de-differentiation [43]. As a result CBV maps are increasingly used in clinical assessment of patients with intracerebral tumours and appear to have application in tumour diagnosis, classification and particularly for the targeting of stereotactic surgical biopsy and post resection radiotherapy [84, 86, 125-127].

The most commonly applied method for mapping CBV is based on dynamic contrast enhanced imaging using susceptibility (T_2*) weighted images (DSCE-MRI) [86, 128, 129]. This approach was first used to study the perfusion of normal cerebral capillary beds in grey and white matter where the blood brain barrier (BBB) is intact and gadolinium based contrast agents can be assumed to act as purely intravascular markers. In these applications susceptibility based contrast mechanisms have the advantage over other MR techniques of increased signal to noise ratio in areas of low blood volume such as capillary beds. However susceptibility based techniques have significant disadvantages related to spatial distortion occurring in areas of paramagnetic variation and residual relaxivity effects in areas of extravascular contrast leakage. This has led several workers to try to derive CBV maps from T_1 weighted data [114, 115, 130-132]. Although these methods showed some promise they are not routinely used, largely because of their tendency to give rise to erroneously high estimates of CBV in areas of extravascular contrast leakage.

In 2000, Li et al. [9, 66, 76] described a novel method for the analysis of relaxivity (T_1) based dynamic contrast enhanced MRI (DRCE-MRI) which uses a shape-based analysis to decompose the dynamic contrast concentration time course data into intra- and extra-vascular components. One consequence of this analytical approach is the generation of an estimate of the intravascular contrast concentration time course curve that is free of leakage effects and therefore ideal for the calculation of leakage-free estimates of CBV.

Examination of the method using Monte Carlo simulation techniques has shown that the representation of CBV values can be expected to be accurate across a wide range of CBV values [76].

The purpose of the study presented here is to compare this novel DRCE-MRI technique with conventional DSCE-MRI approaches. The CBV maps generated from both methods have been compared in terms of image quality (spatial information, distortions, etc.), pixel value distributions within normal brain and measured values within intraaxial cerebral tumours. The aim is to determine the suitability of these CBV maps for diagnosis, grading and the planning and guidance of procedures such as surgery and radiotherapy.

4.2 MATERIALS AND METHODS

Nine patients (4 females and 5 males; mean age 48.2 years) with intra-axial cerebral neoplasms (see Table 1) were recruited into the study. All patients gave informed consent and the Central Manchester Healthcare NHS Trust and Salford Royal Hospitals NHS Trust medical ethical committees approved the protocols.

4.2.1 Image Acquisition

Imaging was performed on a 1.5 tesla MR system (Philips Medical Systems, Best, The Netherlands) using a birdcage head-coil.

Routine clinical T_1- and T_2-weighted anatomical imaging was performed in all patients prior to dynamic studies. Post-contrast T_1-weighted volume images (TR 24 ms / TE 11 ms) were acquired at the end of the dynamic studies and used for qualitative comparison with parametric maps of CBV.

For acquisition of T_1-weighted dynamic contrast-enhanced data, a 3D T_1-FFE (T_1 fast field echo) scanning sequence was applied, with an image matrix of 128 × 128 pixels and 25 slices in the axial plane. The field of view used was 230 mm (square), with a slice thickness of 6 mm with 3 mm overlap (Fourier interpolation), resulting in an effective slice thickness of 3 mm. TR was set at 4.2 ms, and TE at 1.2 ms. Three pre-contrast data sets were acquired for the baseline T_1 calculation using flip angles of 2°, 10° and 35°. This was followed by a dynamic contrast-enhanced acquisition series at a flip angle of 35°, consisting of 120 scans with a temporal spacing of approximately 5 seconds. Gadolinium-based contrast agent (Gd-DTPA-BMA; Omniscan™, Amersham Health AS, Oslo, Norway) was injected as a bolus over 4 seconds at a dose of 0.1 mmol/kg of body weight.

Acquisition of T_2*-weighted data was carried out immediately after completion of T_1-weighted data acquisition so that pre-enhancement would minimize residual relaxivity effects ('T_1 shine through') in the dynamic data [112]. T_2*-weighted (T_2*W) dynamic contrast-enhanced data was acquired using a multislice 2D T_2*W-FEEPI (field echo EPI) sequence. The image matrix was 128 × 128 pixels, with 9 slices in the axial plane. The field of view was again 230 mm (square), with slice thickness of 5 mm with 1 mm interslice gap, giving an effective slice thickness of 6 mm. TR was set at 440 ms, and TE at 30 ms. The dynamic contrast-enhanced series consisted of 52 scans at a flip angle of 35° and a temporal spacing of 1.8 s. A second dose of contrast agent (Gd-DTPA) was injected after the fifth dynamic scan using the same protocol described above.

For all scans the tumour was centred in the imaging volume, the imaging volume included the superior sagittal sinus to provide a vascular input function for analysis and the geometry of the T_2*W acquisitions was selected from the preceding T_1W acquisition so that images were spatially coincident with the central images in the T_1W dynamic dataset.

4.2.2 Image Analysis

Dynamic contrast-enhanced T_1-weighted data was analysed using the First Pass Leakage Profile (FPLP) method described by Li et al [9, 66]. This technique uses a shape analysis to decompose contrast concentration time course data into two separate components representing intra- and extra-vascular contrast agent, allowing calculation of CBV free from the effects of contrast leakage (T_1-CBV), and of the transfer coefficient (K_{fp}) for the passage of contrast between the plasma and the extracellular extravascular space (EES).

T_2*-weighted dynamic contrast-enhanced data was analysed using the technique described by Zhu et al. [43], based on the techniques of Kassner et al. [112]. Multi-slice maps of rate of change of T_2* (ΔR_2*) were calculated from the T_2*W-FEEPI dynamic data signals for each dynamic phase and a gamma variate model [31] was used to fit the first pass ΔR_2*(t) data. Relative cerebral blood volume (rCBV) maps were calculated by pixel-by-pixel integration of the resulting gamma variate curves.

4.2.3 Comparison of T_1-CBV and T_2*-CBV

Visual comparison was performed between maps of T_1-CBV, T_2*-CBV and standard post-contrast T_1W anatomical images. Qualitative analysis included calculation of lesion conspicuity, a calculation of the correlation coefficient between median CBV values from each technique and an attempt to produce pixel by pixel correlation values from one representative case.

Due to spatial distortions resulting from susceptibility effects in the T_2*-weighted acquisition it was not possible to reliably apply automated coregistration of T_1W and T_2*W images. Separate corresponding regions of interest (ROIs) were therefore manually defined on matched T_1W and T_2*W images. ROIs were drawn by an experienced neuroradiologist (T.A. Patankar) and were defined on contrast enhanced images from the late phase dynamic acquisitions. ROI definition included all enhancing components of the tumour but excluded areas of non-enhancement. As with T_1-weighted CBV maps, calculation of CBV values from T_2*-weighted images involved normalization to a value of 1 for a group of vascular voxels (to avoid noise) with an intensity value of greater than 99% of the maximum (assumed to be 100% CBV) to obtain an estimate of absolute CBV. Median tumour CBV values from T_1-CBV and T_2*-CBV were calculated from each ROI, the values were plotted on a scattergram and the correlation between the values tested using Pearson's correlation coefficient. In addition direct visual comparison of T_1-CBV and T_2*-CBV maps was performed using a standardized colour map to aid comparison.

ROIs were also drawn on normal appearing white matter on both T_1-CBV and T_2*-CBV maps, and the mean (μ) and standard deviation (σ) from these were compared to values from the enhancing tumour ROIs in the same maps, to ascertain an index of tumour conspicuity using the following expression:

$$\text{conspicuity} = \frac{\left|\mu_{tumour} - \mu_{white\_matter}\right|}{\sigma_{tumour} + \sigma_{white\_matter}} \qquad \textbf{4.1}$$

Since distortion on T_2*W images prevents accurate coregistration with T_1W images we compared pixel-by-pixel values of T_1-CBV and T_2*-CBV in non-tumour brain using the following method.

A single corresponding slice was chosen from the T_1-CBV and T_2*-CBV maps of a representative case and manually registered. The T_1-CBV map was then normalised to the T_2*-CBV by finding the peak in the distribution of the logged CBV ratio over all voxels. Actually, scattergrams were produced of the square-root of the CBV estimates from normal vascularised brain only in the two data sets over a range of 0 – 0.6 in square-root CBV ($\sqrt{\text{CBV}}$). The square root is taken for two reasons: first it produces voxel CBV estimates which have uniform error, and secondly, it expands the dynamic range of the data making it easier to see trends in the correlation between the two datasets. A second scattergram was obtained by taking the most similar value from the T_1-CBV image to the T_2*-CBV image corresponding to a half pixel linear interpolation in one of four directions (anterior, posterior, left, right) – a *pixel shuffle* technique. This is intended to account for slight non-rigidity between the two volumetric acquisitions and broadening of large blood vessels in T_2* data due to susceptibility effects.

Finally, a direct qualitative comparison was made between volume rendered datasets from each technique. Due to the high level of noise in parametric calculated images, volume rendering was based on specifically calculated correlation images for each dataset. Signal intensity time courses were extracted for both a major vessel and enhancing tumour. These time courses were correlated with the time course from each individual voxel within the original volume, resulting in two sets of volume data with a dynamic range of -1 to +1 representing the correlation coefficients. These volumes of correlation coefficients were rendered using Amira™ (TGS Template Graphics Software, Inc., USA). The quality of the individual volume renders from DSCE-MRI and DRCE-MRI were compared using a four point scale (0: non-diagnostic; 1: poor; 2: satisfactory; 3: excellent), evaluated by experienced neuroradiologists (A. Jackson and T.A. Patankar).

4.3 RESULTS

Parametric images from all patients were of good quality without motion artefacts. There was no evidence of residual relaxivity effects ('T_1 shine through') in the dynamic T_2*-weighted data, which was tested as described previously [112].

Figure 4.1 shows a typical representative axial slice through the centre of a high grade glioma (patient 8). A standard high resolution T_1-weighted volume post-contrast anatomical image showing the enhancing portion of the tumour and enhanced vasculature (Fig. 4.1(a)) is provided for comparison with parametric maps. Fig. 4.1(b) is a T_2*-CBV map at the same location as that of Fig. 4.1(a) and displays the distribution of CBV values within the brain and tumour tissue (note that the skull and scalp have been stripped from this image during processing). Normal vasculature, such as the branches of the middle cerebral artery and the cerebral veins, show high values of CBV as expected, and the enhancing portion of the tumour shows a heterogeneous distribution of CBV values. There is good differentiation of normal grey and white matter. Note that blood vessels appear much broader and smoother-edged on the T_2*-CBV map than on the high resolution anatomical image. There is also considerable signal drop-out and distortion in the basal prefrontal cortex due to susceptibility artefact resulting from air in the paranasal sinuses. Fig. 4.1(d) is a T_1-CBV map at the same location as Fig. 4.1(a). In contrast to Fig. 4.1(b) the map shows improved demonstration of high spatial frequency features and anatomical details, particularly vascular structure, corresponding closely to the anatomical image (Fig.

4.1(a)). The signal-to-noise ratio in normal grey and white matter in Fig. 4.1(d) is poorer than in the T_2*-CBV image but still allows clear subjective visual discrimination. The spatial distribution of CBV values in Fig. 4.1(b) and 4.1(d) is similar in normal brain, tumour and vessels. The FPLP method also generates maps of K_{fp} as shown in Fig. 4.1(c) indicating an intact blood brain barrier where K_{fp} is zero or consistent with noise, and areas of higher K_{fp} representing contrast leakage only within the tumour and choroid plexus.

Figures 4.2(a) and 4.2(b) are T_1-CBV and T_2*-CBV maps of the tumour and major basal arteries in patient 1. These images have been chosen to show the extent of the broadening of major blood vessels in the T_2*-CBV map compared with the same vessels in the T_1-CBV map and in the high resolution anatomy image (Fig. 4.2(c)), and have been windowed accordingly. Marked distortion and broadening of the main blood vessels in the T_2*-CBV image is clearly observed, and some detail of vascular structure is obscured in comparison to the T_1-CBV map. When compared to the high resolution anatomy image the large vessels seen in the T_1-CBV map correspond closely to their true location and size.

Figure 4.3 shows a plot of median measurements from the tumour ROIs on T_2*-CBV and spatially corresponding T_1-CBV maps. There is a significant correlation between these median values of T_1-CBV and T_2*-CBV ($r = 0.667$, $p = 0.05$). Comparison of tumour conspicuity values between T_1-CBV and T_2*-CBV maps showed no significant difference; hence visual identification of tumour tissue is equally good on both. The scatter plot in Figure 4.4 shows the pixel by pixel variation between T_1-CBV and T_2*-CBV in normal brain. The plot illustrates a strong correlation between CBV estimates from the two techniques ($r = 0.92$, $p < 0.001$) and three additional features. First, estimates of T_1-CBV extend down to zero, whereas those from T_2*-CBV appear to be restricted to values above 0.01 CBV (0.1 in square-root CBV). This is entirely consistent with the expected susceptibility effects of enhancing capillary beds in T_2* images. Secondly, the correlation is strong but with a broad random component. Thirdly, there is some evidence for an excess of large (> 0.2 CBV) values in T_2*. Figure 4.5 is a pixel-by-pixel scattergram representing the same data using the pixel shuffle technique, which is intended to reduce differences due to small local spatial distortions. The results indicate that both approaches to CBV estimation are consistent ($r = 0.96$, $p < 0.001$) with the exception of spatial distortion effects in T_2*-CBV, the differences being due to capillary enhancement occurring only in CBV values below those generally common in brain tissue.

3D volume renderings from DRCE-MRI and DSCE-MRI data are shown in Figure 6. Corresponding rendered mappings of correlation with an enhancing portion of tumour tissue (Fig. 4.6(a)) and with a major blood vessel (Fig. 4.6(b)) from DRCE-MRI data demonstrate high quality volumetric information about the location of the tumour and major vasculature in relation to the patient's head (the skull, scalp, ears and nose are clearly visible). Fig. 4.6(a) essentially gives an indication of voxels having enhancement time courses consistent with contrast leakiness, and Fig. 4.6(b) of voxels having enhancement time courses consistent with a major blood vessel. The low signal-to-noise ratio of normal grey and white matter vasculature in the T_1-weighted data aids the clear visualisation of tumour and major vasculature within the volume. Only the mapping of correlation with a major blood vessel for the DSCE-MRI data is shown in Fig. 4.6(c) because the correlation mapping with enhancing tumour was very similar. The absence of the skull and scalp make it difficult to perceive the relationship between the brain and anatomy. The broadening of normal grey and white matter vasculature is visible. Major vasculature and the tumour margins are not easily distinguishable in the rendered volume, being obscured by the vessels of the brain parenchyma. Mean visual quality scores for renderings from T_1- and T_2*-weighted data were 2.6 and 1.2 respectively.

4.4 DISCUSSION

Measurements of CBV based on DSCE-MRI techniques have clinical significance in a range of disease states and appear to provide similar information to fluorodeoxyglucose PET scanning concerning the presence and distribution of tumour tissue heterogeneity [97]. In patients with stroke, regional changes in CBV correlate poorly with local flow changes and far better with changes in local water diffusion characteristics and appear to reflect local autoregulatory status [133, 134].

The generation of quantitative CBV maps has traditionally been based on T_2* weighted sequences utilizing susceptibility contrast mechanisms. DSCE-MRI approaches were initially used because the susceptibility contrast mechanism gives a superior signal-to-noise ratio in low density capillary beds such as are seen in normal brain [125, 128, 135]. In addition, the signal changes seen on T_2* weighted images in normal brain are less affected by contrast in large vessels, so that DSCE-MRI acquisitions were classically considered as "capillary weighted". These properties can be considered beneficial for the study of normal brain tissue where the CBV is low and the blood brain barrier is intact.

However, the use of DSCE-MRI techniques to measure CBV in cerebral tumours is associated with a number of inherent disadvantages. High sensitivity to susceptibility effects is associated with distortions around susceptibility interfaces, which will include the air in the paranasal sinuses and petrous bone and structures containing a high concentration of contrast in enhanced images. Secondly, leakage of contrast due to blood brain barrier breakdown, which is an intrinsic feature of malignant cerebral tumours, will cause competing relaxivity effects on the observed signal changes which will lead to erroneous underestimation of CBV. In practice, these effects are compensated by decreasing the T_1 sensitivity of the sequences or by contrast pre-enhancement to saturate T_1 based signal change effects as was performed in the current study [112]. Thirdly, T_2* weighted images rely on the use of long echo times (TE) to maintain their T_2 sensitivity which reduces the size of the sampling matrix and number of slices which can be acquired within the required temporal resolution (approximately 2 seconds). This can be tackled by the use of echo planar imaging (EPI) acquisitions which greatly enhance acquisition speed but which will impose additional and unpredictable spatial distortions into the image making them potentially unsuitable for spatially-sensitive procedures such as surgical planning applications. These effects can be reduced to some extent by the use of segmented EPI acquisitions and temporal resolution can be maintained by the use of echo shifting techniques in sequences such as PRESTO which also uses a volume acquisition to maintain signal to noise ratio [136].

In view of the problems associated with DSCE-MRI techniques several groups have attempted to use relaxivity based dynamic images (DRCE-MRI) to derive estimates of CBV. The potential advantages of this approach include the lack of spatial distortion associated with T_1W images and the potential for fast 3D imaging approaches without the need for EPI collections. The major problem with DRCE-MRI in enhancing tissues is the inability to separate the effects of intravascular and extravasated contrast on the observed signal change. This means that signal changes in areas of high capillary permeability will result to a large degree from contrast leakage and estimates of CBV will therefore be erroneously high.

Despite this disadvantage, Hacklander's group in the late nineties described the use of DRCE-MRI in cerebral tumours in a series of publications [115, 130-132]. This group dealt with the leakage problem by assuming that contrast leakage is so slow that it can be ignored over the time course of a single passage of a contrast bolus. They stated that: “gadopentate dimeglumine can almost be regarded to be an intravascular contrast agent, even in cases of a disturbed blood brain barrier”. They concluded that T_1-CBV measurements could be used in enhancing tissues. However, it is interesting to note that they were unable to demonstrate significant differences between grade III and grade IV glioma even though this has been shown by several groups using susceptibility based techniques [43, 113, 114]. In addition, careful comparison of the results from the T_2* and T_1 based techniques shows systematic overestimation of T_1-CBV in tumours with high values (Figure 7 in [132]). Although the authors do not comment on this a similar observation was highlighted by Bruening et al. [114], who described areas of apparently very high CBV on T_1-CBV maps which were not seen on T_2*-CBV. They commented: “In the high grade group, different values between T_1 and T_2 CBV maps were apparent”, concluding: “Theoretically one would anticipate that in settings of blood brain barrier disruption there would be a tendency for T_1 rCBV maps to cause elevated rCBV measurements. In contrast T_2 rCBV maps tend to underestimate the apparent rCBV values in the presence of a blood brain barrier breakdown and may show false negative findings in the event of an active tumour recurrence.”

In practice, as described above, the tendency for T_2*-CBV maps to underestimate CBV in areas of contrast leakage can be minimised by a variety of acquisition strategies which are discussed in detail by Kassner et al. [112], so that the major residual disadvantages of T_2* based methods are the distortion associated with susceptibility effects and the restrictions on imaging time. The sequences used here represent a compromise between spatial resolution and susceptibility sensitivity using a segmented EPI acquisition protocol to reduce scan time whilst minimising the degree of spatial distortion. Despite this we were only able to collect 9 slices of data at a matrix of 128^2 within the 1.8-second time resolution required and the resultant images show significant distortions both at tissue-air interfaces and more importantly, around large vessels. Further improvements in gradient performance mean that our current system can collect 12 slices within the same time window but, in reality, the use of T_2* EPI sequences is problematic. The use of optimized T_2* based sequences such as PRESTO [136] offer the opportunity to improve on this performance by combining echo shifted, segmented EPI collection and volume acquisition techniques in order to maximize temporal and spatial resolution whilst limiting sensitivity to susceptibility artefacts and distortions. Although these sequences are still not widely available and we have not used them in this study our experience with them indicates that the improvements in susceptibility distortion are relatively limited and spatial distortion remains a significant problem [112, 137].

The use of DRCE-MRI offers significant theoretical advantages allowing increased sampling speed and therefore greater spatial resolution and coverage. More importantly there is no susceptibility spatial distortion associated with standard T_1W sequences. A third potential advantage is the ability to use reduced contrast doses compared to DSCE-MRI although we have not explored that aspect in this study [114, 132]. The major problem with DRCE-MRI is that the signal changes resulting from intravascular contrast and from extravasated contrast occur in the same direction and, since they result from the same physical contrast mechanism, cannot be separated by modifications of the acquisition technique. We have used the first pass leakage profile model described by Li et al. [66, 76] to separate these effects and to generate leakage free T_1-CBV maps. This analysis technique decomposes the contrast concentration time course data from DRCE-MRI into two components: the first due to intravascular contrast agent, and the second due to contrast agent leakage into the extravascular extracellular space. The technique works by using a constrained shape model of each component and decomposing the data to produce the optimised fit to these constraints. Although the technique was designed to produce estimates of transendothelial contrast transfer coefficient (K^{trans} [7], or more specifically K_{fp} [70]) which are free of intravascular contrast effects it also allows calculation of leakage-free CBV maps. The theoretical advantages in terms of temporal resolution, tissue coverage and freedom from image distortion have been the subject of the present study. However, it is equally important to know that CBV estimates from DRCE-MRI provide comparable biological information to those derived from conventional DSCE-MRI techniques. This study has confirmed that this is the case with close correlation between median values and also excellent pixel-by-pixel agreement, particularly when spatial distortion effects are reduced. The advantages of T_1 techniques allow confident use of parametric maps for image guided surgical procedures and radiotherapy planning with negligible risk of error due to spatial distortion. The ability to increase coverage and through plane resolution also allows direct 3D visualisation of these data sets with better practical quality than with DSCE-MRI.

In conclusion we would recommend the routine use of T_1-weighted DCE-MRI for the measurement of CBV in cerebral tumours. The technique allows larger sampling volumes, removes the risk of significant spatial distortion, provides biologically equivalent data to conventional T_2*-weighted DCE-MRI methods and has the added advantage of providing high-quality maps of the transfer coefficient.

Patient No.	*Sex*	*Age*	*Histological Grade**
1	M	58	IV
2	M	28	Unconfirmed
3	F	31	II
4	F	22	Unconfirmed
5	F	55	IV
6	M	52	IV
7	F	63	IV
8	M	54	IV
9	M	71	IV

Table 4.1. Patient demography.
* Grading according to World Health Organisation (WHO) criteria for histopathological findings of tissue biopsy samples, taken after imaging. In general, glioma grade II = fibrillary astrocytoma; III = anaplastic astrocytoma; IV = glioblastoma multiforme. Unconfirmed cases have not had histopathological findings reported.

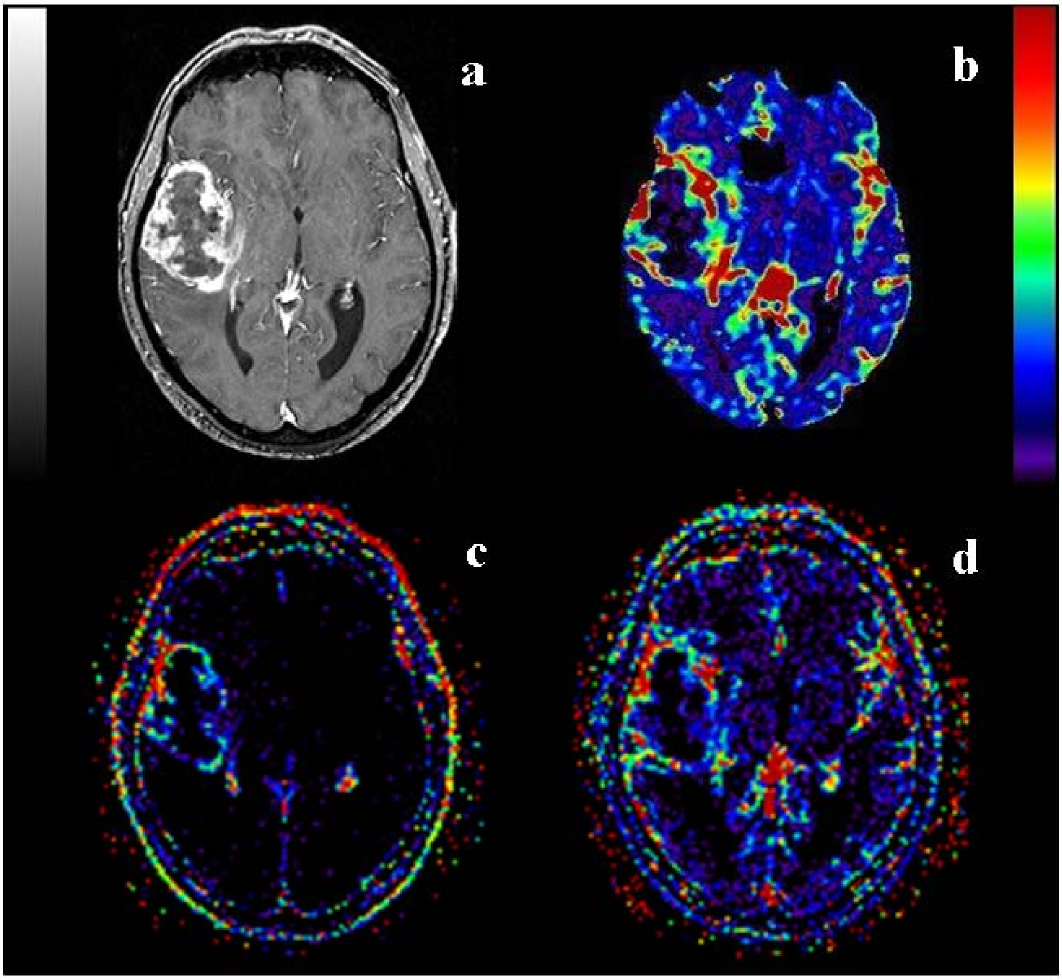

Figure 4.1. (a) High resolution post-contrast T_1-weighted (volumetric T_1-FFE / TR 24 ms / TE 11 ms) anatomical image showing an enhancing high grade glioma (patient 8). (b) Corresponding cerebral blood volume (CBV) map generated from T_2*-weighted EPI dynamic susceptibility-enhanced data (T_2*-CBV) [values range 0 - 100%]. Related maps generated from T_1-weighted fast field echo contrast-enhanced dynamic data of (c) K_{fp} [values range 0 – 1.2 min^{-1}] and (d) T_1-CBV [values range 0 – 100%]. ((b),(c) and (d) use the same colour rendering table for display.)

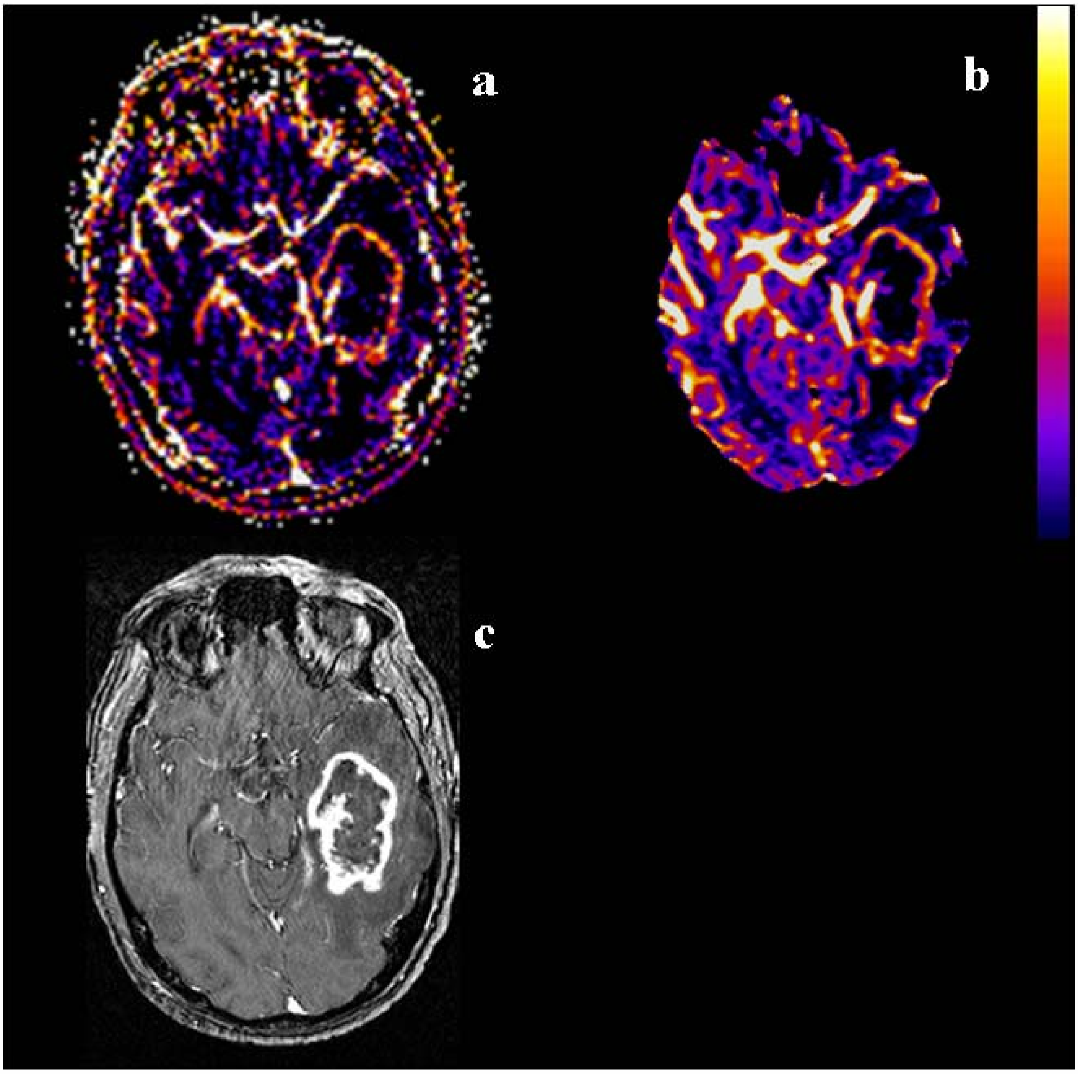

Figure 4.2. Corresponding T_1-CBV (a) and a T_2*-CBV (b) maps showing a high grade glioma, the circle of Willis and middle cerebral arteries (patient 1). (c) High resolution post-contrast T_1-weighted (volumetric T_1-FFE / TR 24 ms / TE 11 ms) anatomical image showing the same location. ((a) and (b) use the same colour rendering table for display.)

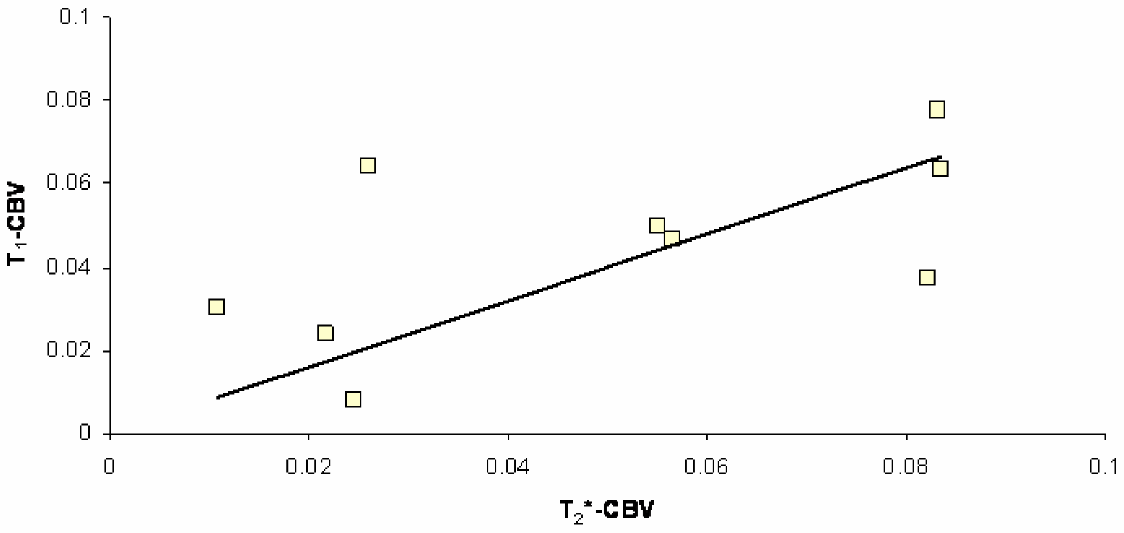

Figure 4.3. Comparison of the median measurement taken from enhancing tumour tissue ROIs on manually matched slices of T_1-CBV maps against T_2*-CBV, for all our tumour cases. (rho = 0.667, $p < 0.05$)

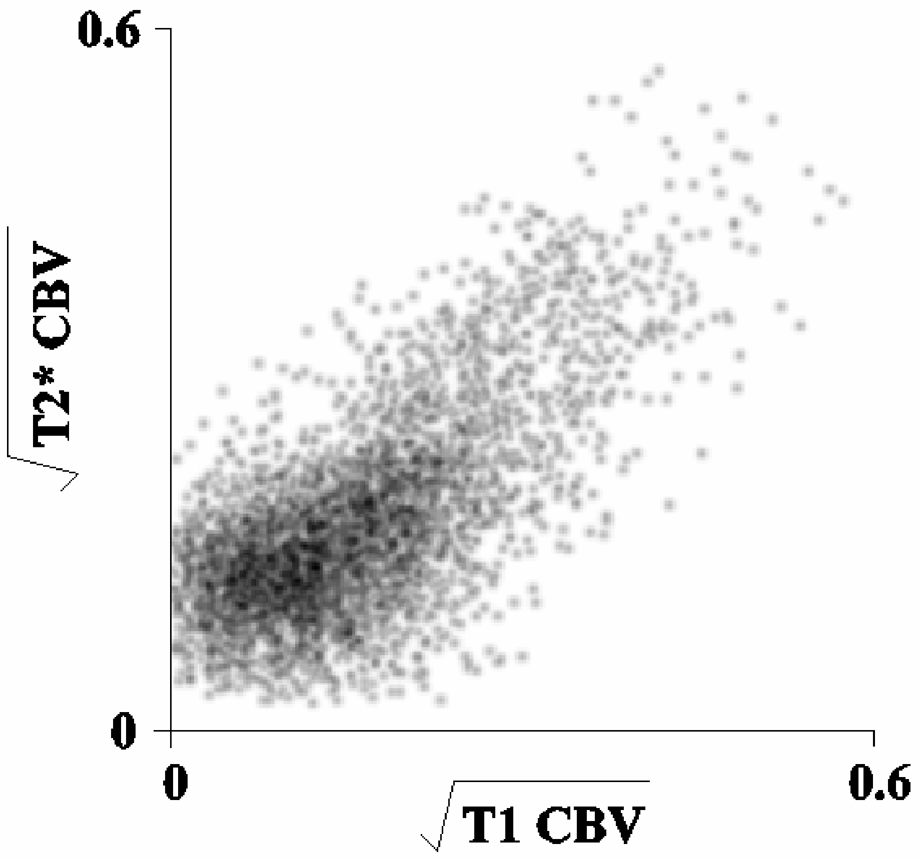

Figure 4.4. Pixel-by-pixel scattergram of a visually matched brain slice from the T_1-CBV and T_2*-CBV maps in patient 7, using a vascular region of normal brain only. The square-root of the values from the two maps are used to ensure uniform error and to expand the dynamic range of data for visualisation (see text). ($r = 0.92$, $p < 0.001$)

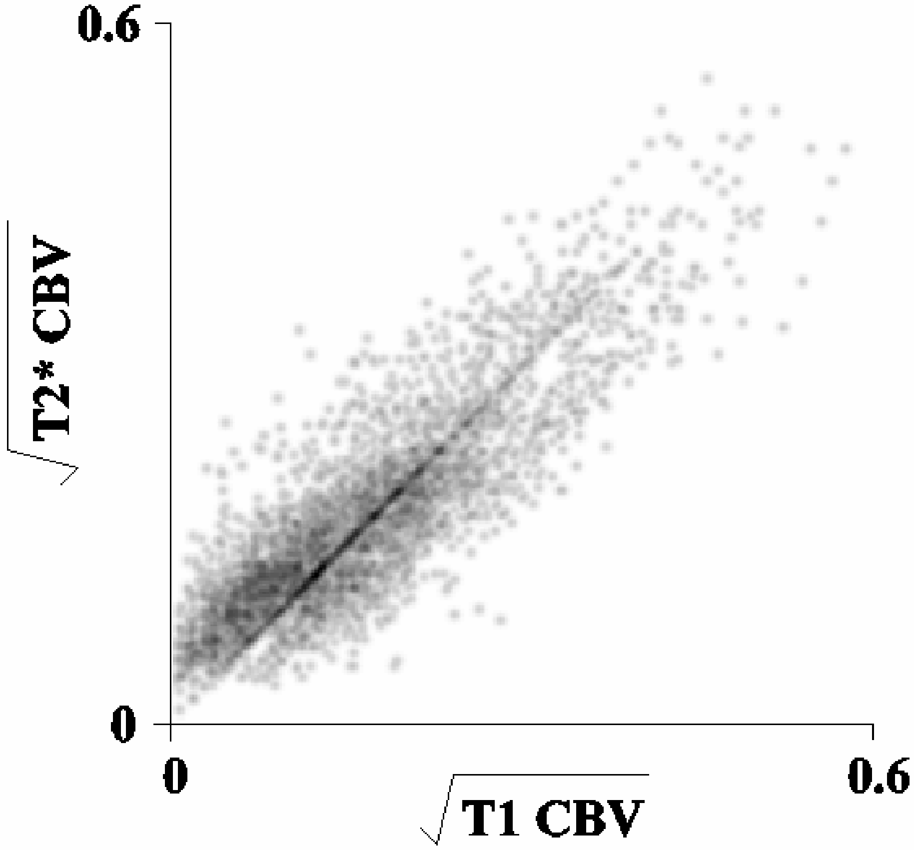

Figure 4.5. Pixel-by-pixel scattergram generated from the same data as in Fig. 4.4 except that this has been produced by a pixel shuffling method between CBV maps to allow for spatial distortions in the T_2*-CBV map (see text). ($r = 0.96$, $p < 0.001$)

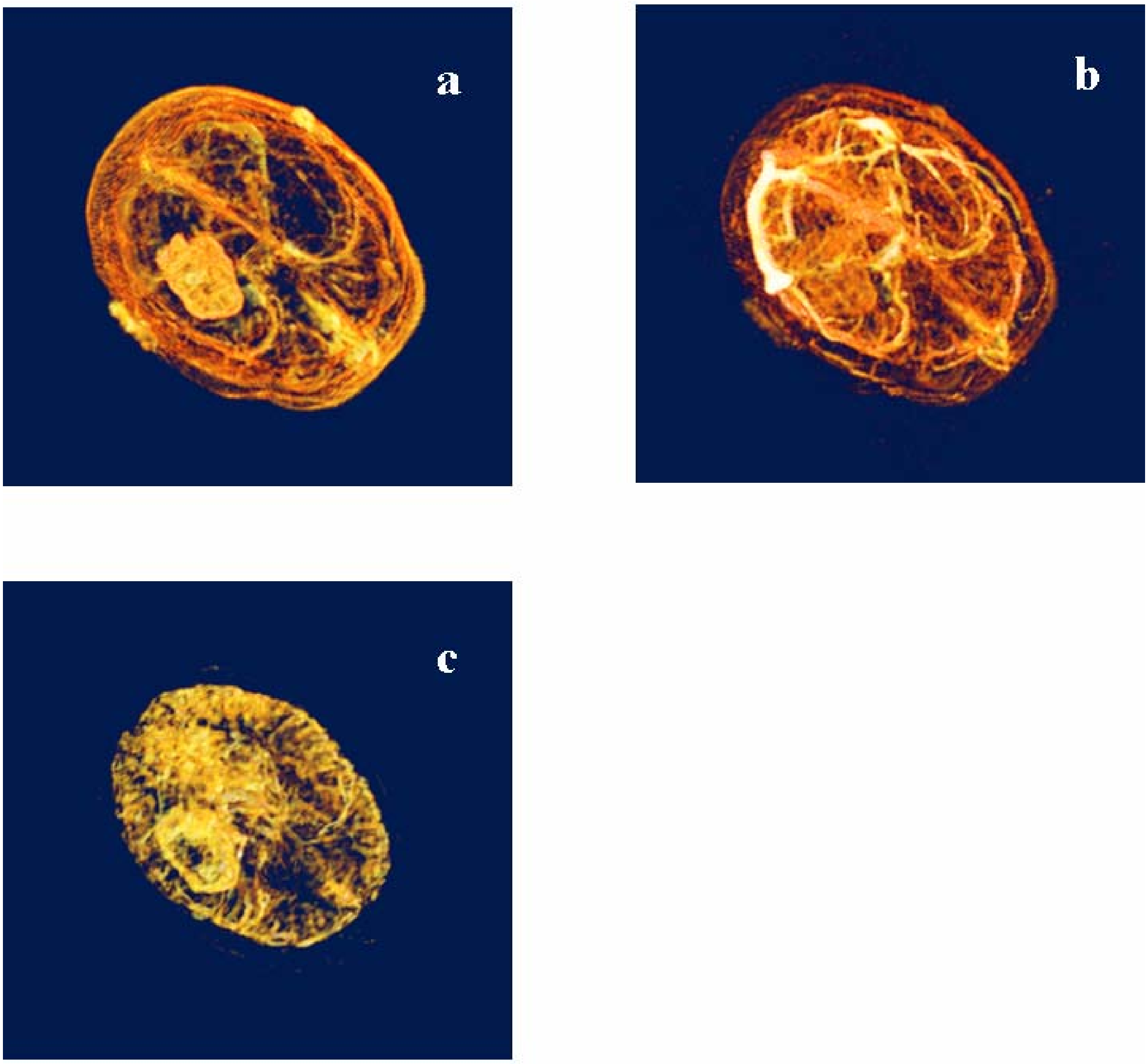

Figure 4.6. 3D volume rendered correlation mappings with enhancing portion of tumour tissue (a) and with a major blood vessel (b) from DRCE-MRI data, and with a major blood vessel from DSCE-MRI data (c).

CHAPTER 5 :

BREATH-HOLD PERFUSION AND PERMEABILITY MAPPING OF HEPATIC MALIGNANCIES USING MAGNETIC RESONANCE IMAGING AND A FIRST-PASS LEAKAGE PROFILE MODEL

This Chapter is a reproduction of [65].

5.1 INTRODUCTION

The quantification of endothelial permeability in tumours has attracted increasing attention in recent years with the recognition that the growth of tumours is dependant on the development of new blood vessels via a process known as angiogenesis [138]. This recognition has led to the realization that the characteristics of the tumoral microvasculature such as vascular density and endothelial permeability can provide important information about prognosis and tumour behaviour [23, 129, 139, 140]. In particular there has been considerable research activity in developing novel therapeutic agents that utilize the characteristics of the angiogenic process to specifically target the developing microvasculature [141, 142]. We have recently described a new technique for simultaneous calculation of blood volume and endothelium permeability images from large three-dimensional data sets in patients with brain tumours [9, 43]. The novel feature of this model is that it uses only data collected during the first passage of the bolus of contrast media through the target tissue so that data acquisition is extremely fast compared with the conventional method for measuring permeability [53-55]. Since data acquisition can be performed in a single breath-hold, it has the potential to be used in abdominal studies where respiratory motion complicates the collection of dynamic data for the measurement of contrast enhancement. Unlike normal brain the microcirculation in normal liver is highly permeable to transitional metal ions and compounds of gadolinium or manganese, such as feromoxides [143, 144] and gadolinium diethylene triamine penta-acetic acid (Gd-DTPA) [145]. In addition the blood supply to the liver is derived jointly from the hepatic arteries and the portal venous system so that systemically administered contrast agents arrive at the liver in two distinct phases [146]. In this study, we have applied the first pass analysis technique in a patient group with hepatic neoplasm to investigate the feasibility of permeability mapping using the first pass technique and breath-hold acquisitions, to examine the reproducibility of the technique and the effect of the liver's dual vascular supply on the assumptions of the model.

5.2 MATERIALS AND METHODS

5.2.1 Patients

Fourteen patients with known liver tumors were included in the study. All patients gave informed consent and the Central Manchester Healthcare Trust Medical Ethics Committee and the South Manchester Ethical committee approved the study. Table 5.1 shows the demographic data and histological diagnosis for each patient.

5.2.2 Clinical Imaging

MR images were obtained on a 1.5 T Philips ACS NT-PT6000 MR system with maximum gradient strength of 23 mT/m and maximum slew rate of 105 mT/m/ms (Philips Medical Systems, Best). Prior to the MR examination a 16G catheter was inserted into an antecubital vein using local anaesthetic (lignocaine, s.c.). The imaging protocol for dynamic contrast enhanced studies consisted of three consecutive three-dimensional radiofrequency (rf) spoiled (T_1-weighted) field echo acquisitions with an array of flip angles (α = 2, 10 and 35°) to allow calculation of T_1 maps. The third sequence was repeated ($n = 6$, duration $T = 24.6$ s) for baseline acquisition. The same sequence was then repeated to produce a T_1-weighted dynamic data set (T_1dy) with a time resolution of Δt = 4.1 s and a duration of 41 s. All images were acquired in the axial plane and MR parameters are shown in Table 5.2. Contrast agent (0.1 mmol/kg of gadodiamide, Gd-DTPA-BMA; Omniscan, Nycomed, Oslo) was given as a manual intravenous bolus injection over a period of 4 s and was immediately followed by a bolus of 35 ml of normal saline injected at the same rate. The injection was started as the dynamic imaging sequence was initiated. The images were all collected during breath holding. The first three images providing the variable flip angle data were collected in one breath-hold (19 s) and the baseline images were collected in a second breath-hold (18 s). The dynamic enhancement data was collected using a 41 s data acquisition and the patient was asked to hold their breath for as long as was comfortable during this acquisition. Data for the analysis is adequate if the data collection covers the initial precontrast baseline to the first two collection points after the recirculation bolus. This can be achieved in as little as 25 s if the timing of the bolus arrival and the image collection coincide. Additional data collected after the patient begins to breath was easily identified by the presence of movement artefact and was discarded. All patients were rehearsed in the MR protocol immediately prior to the examination. Patients were not imaged at any specific time of day and no attempt was made to control their dietary intake prior to scanning. Five patients were reimaged again 48–56 h after the initial studies in order to establish the reproducibility of the technique (Table 5.1).

5.2.3 Data Analysis

All images were transferred to an independent workstation for analysis (Sun Microsystems, Palo Alto, CA).

A) Movement Correction

The spatial positions of the liver in the three separate breath-hold acquisitions were compared by performing spatial coregistration of the hepatic component of each data set to the baseline scan. The coregistration algorithm chosen uses a calculation of the dot product of gradient edge strengths and is therefore suitable for comparison of images with divergent contrast characteristics. The transformation matrices from the coregistration procedure were used to identify patients with significant misregistration (greater than one voxel in any direction) between the breath-hold sequences. Misregistration of this magnitude was seen in two cases and misregistered data was realigned using a scaled sinc kernel [147].

B) Calculation of Contrast Agent Concentration.

Maps of proton density (M_0) and intrinsic longitudinal relaxation rate ($R_{10} \equiv 1/T_{10}$) were calculated by fitting the steady-state T_1-FE signals $S(\alpha)$ with the Ernst formula (assuming $TE << T_2*$):

$$S(\alpha) = M_0 \cdot \sin\alpha \cdot (1 - E_{10}) / (1 - \cos\alpha \cdot E_{10}) \qquad \textbf{5.1}$$

where α has three discrete values (α = 2, 10 and 35°) and $E_{10} = \exp(-TR \cdot R_{10})$.

Four-dimensional maps of longitudinal relaxation rate [R_1(t)] maps were calculated using signal intensity data from pre- and post-contrast T_1-FE images [$S(t) - S(0)$]:

$$R_1(t) = -\left(\frac{1}{TR}\right) \cdot \ln\left\{\frac{1-(A+B)}{1-\cos\alpha \cdot (A+B)}\right\} \qquad \textbf{5.2}$$

where $\alpha = 35°$, $TR = 4.3\text{–}7.0$ ms, $A = [S(t) - S(0)]/(M_0 \cdot \sin\alpha)$, $B = (1 - E_{10})/(1 - \cos\alpha \cdot E_{10})$.

Four-dimensional Gd-DTPA-BMA concentration maps were then calculated for each dynamic phase:

$$C(t) = \frac{R_1(t) - R_{10}}{r_1} \qquad \textbf{5.3}$$

where r_1 is the relaxivity of Gd-DTPA-BMA determined experimentally, $r_1 = 4.39\ \text{s}^{-1}\ \text{mM}^{-1}$ (at 37°C).

In recent work we have introduced a new parameter, which we call the leakage profile of contrast agent [9]. The leakage profile is based on a well-established pharmacokinetic model as shown below [52]:

$$\frac{dC_e}{dt} = K^{trans}\left(\frac{C_p(t) - C_e(t)}{v_e}\right) \qquad \textbf{5.4}$$

where v_e is the extra-vascular contrast distribution volume, C_e is the concentration of contrast in the extravascular space, K^{trans} is the endothelial permeability surface area product and C_p is the concentration of contrast agent in plasma. If we assume that back-flux can be ignored during the first vascular pass of contrast bolus, eq. 5.4 becomes:

$$v_e \frac{dC_e}{dt} = K^{trans} \cdot C_p \qquad \textbf{5.5}$$

Thus, the extravascular component of the total contrast concentration in a voxel is equal to the transfer constant, now called K first pass (K_{fp}), times the integral of the plasma concentration of contrast agent.

$$C_t(t) = \mathrm{K}_{\mathrm{fp}} \int_0^t C_p(t')dt' \qquad \textbf{5.6}$$

We call this function the leakage profile (LP):

$$LP(t) = \int_0^t C_p(t')dt' \qquad \textbf{5.7}$$

Calculation of K_{fp} using this approach requires accurate identification of the temporal variation of contrast agent concentration in the blood vessels supplying the tissue. This function is commonly referred to as the arterial, or more correctly the vascular input function (VIF). In the case of the liver the organ is supplied by two distinct vascular systems. Approximately 10–15% of the blood supply to normal hepatic parenchyma is derived from the aorta via the hepatic arteries. The majority (75–85%) comes from the portal vein via the splenic and intestinal circulation. This creates a complex situation making the identification of the correct VIF for any individual voxel difficult unless one or other of the vascular supplies is heavily dominant. In contrast to hepatic parenchyma the arterial supply to hepatic tumours is usually derived wholly or largely from the hepatic artery. A VIF was therefore determined from the aorta or hepatic artery in all cases. It must be noted, however, that this VIF is entirely inappropriate for use in the hepatic parenchyma supplied predominantly via the portal venous system (*vide infra*). In order to provide an indicator to the source of vascular input in each voxel, a parametric map of the time of contrast arrival (T_0) was generated and was used to identify voxels where the vascular supply arises predominantly from the portal system.

5.2.4 Calculation of K_{fp} and BV_{T1}

Contrast concentration changes in tissue over time on T_1-weighted images represent a cumulative effect of intra and extravascular contrast agent. Failure to compensate for this effect will result in the overestimation of K^{trans} in voxels with significant intravascular contrast. This will in turn lead to a bias in the estimation of K^{trans}, which will appear artificially high in tumours with a larger perfused blood volume. This effect has been called ‘pseudopermeability’ and can be addressed in a number of ways. These include the use of simple cut-off threshold values for K^{trans} and attempts to correct data using rBV maps calculated from T_2*-weighted data. T_2*-weighted data can be collected in a separate acquisition or simultaneously using dual echo techniques to derive both T_1 and T_2 weighted measurements. We have used a high temporal resolution T_1-weighted data collection and employed post-processing techniques to decompose the data for each voxel into intra and extravascular components. The post processing strategy has the following steps:

1. A vascular input function [$C_p(t)$] is obtained for each patients from voxels in the hepatic artery or abdominal aorta.
2. The ratio of peak $C_p(t)$ and steady-state $C_p(t)$, marked by the beginning of recirculation of contrast bolus, is measured from the VIF curve for use later in the analysis. This value represents the ratio of the peak concentration of contrast agent to the concentration in recirculation phases and is abbreviated to RPR.
3. The measured $C_p(t)$ curves are integrated to calculate the tumour LP.
4. For each voxel the leakage profile is used to define the shape of the extravascular contrast component, with K_{fp} providing the scaling factor [eq 5.6]. The residues from

each voxel between the extravascular component defined by the LP and the actual data define the intravascular component. In order to perform this step the timing of the leakage profile is modified so that the contrast arrival time for the LP coincides with the contrast arrival time observed in the voxel.

5. An iterative process is then used to optimize the separation of these intra- and extravascular components. The iterative process determines the accuracy of the iterative decomposition by assessing the goodness of fit of the decomposed intravascular contrast concentration data to the RPR measured in step 2. The measured RPR is then used to modify the estimate of the intravascular contrast concentration in the recirculation phase to conform to the ratio measured in the input function. The process proceeds through this iterative loop until the difference between two successive estimations of K_{fp} is smaller than ε (= 10^{-4} min^{-1} in the current study).

The decomposed concentration–time course data were then used to derive estimates of K_{fp} using eq. 5.6 and BV_{T1} expressed as the area under the curve of the intravascular contrast concentration. Parametric images of K_{fp} and BV_{T1} were thresholded using T_0 measurements in order to remove normal liver tissue supplied by the portal system.

Volumes of interest within tumours were defined from maps of contrast enhancement generated by subtraction of pre-contrast from post contrast images. Non-enhancing tumour tissue was not included in the volume of interest.

5.2.5 Measurement of reproducibility

In five cases maps of K_{fp} and BV_{T1} were available from the same patient on separate examinations. This data was used to assess the reliability of repeated measurements of K_{fp} and BV_{T1}. The reproducibility of semi-automated and manual measurement of tumour volume was assessed. Manual tumour volume estimates were derived by manual placement of a volume of interest on maps of enhancement generated by subtraction of precontrast from enhanced images. The semi-automated method used a thresholding approach based on the parametric maps of T_0. Histogram analysis of these maps demonstrates a clear bimodal distribution corresponding to systemic arterial and portal venous supply. A threshold midway between the mean values of these identifies voxels supplied primarily by the arterial tree; these thresholded images contain multiple small areas of low T_0 due to the inclusion of parenchymal branches of the hepatic arteries. These were removed using a morphological closing operator followed by a conditional dilation. A single-tailed Wald–Wolfowitz runs (W-W) tests [148] was used to test for differences in the distributions (histograms) of K_{fp} and BV_{T1} values measured on days 0 and 2. Median and 97.5% centiles of K_{fp} and BV_{T1} for the whole tumor volume were calculated for each patient and for each observation and were used as an indicator of the spread of the data [149, 150].

Reproducibility of volume measurements and of the median and 97.5% centile values of K_{fp} and BV_{T1} was assessed by measurement of the variance calculated as:

$$V = \frac{\sum (x_1 - x_2)}{n \cdot \sqrt{2}} \qquad \textbf{5.8}$$

where x_1 and x_2 are the values measured on the first and second visits and n is the number of subjects. This figure represents a direct estimate of error on repeated measurements. The ratio of the variance (V_r) was also calculated as $V_r = V \cdot 1/x$ where x is the mean value. Since this study used a relatively small number of cases the potential error on the estimate of V was assessed using standard F statistics.

5.3 RESULTS

Examination of the data from individual patients showed remarkably reliable spatial co-registration between data collected on separate breath holds. In 12 cases misregistration was less than one voxel in any direction. In the two remaining cases data collected during one breathhold was slightly misaligned by one to three voxels. Sinc reslicing of the data produced adequate realignment with no evidence of distortion due to non-rigid tissue deformation.

Examination of the vascular supply to the liver demonstrated little difference in the timing or shape of the leakage profile derived from the aorta and the hepatic artery (Fig. 5.1). Portal vein flow was typically delayed by 10–17 s after the arterial supply and demonstrated no evidence of any first-pass peak (Fig. 5.1). In all cases the shape of the portal vein curve was a smooth increase in contrast concentration. All enhancing tumour tissue demonstrated rapid increase in contrast concentration that peaked whilst the portal vein concentrations were still rising (Fig. 5.2). Normal liver tissue showed a slow delayed rise in concentration mirroring the timing of the portal vein contribution.

Examination of T_0 maps clearly demonstrates early arterial passage of contrast, an intermediate phase as blood passes into the capillary beds of arterially supplied tissues such as the spleen and hepatic neoplasms and a late portal phase due to blood from the hepatic portal system supplying the normal hepatic parenchyma (Figure 5.3).

Maps of T_0, K_{fp} and BV_{T1} were subjectively of high quality with homogeneous distributions of parametric values in normal tissues and clear delineation of small structures such as the branches of the portal vein and hepatic arteries (Figure 5.4). Examination of the maps from normal hepatic tissue and from portal system tributaries shows extremely high values of K_{fp} and very low values of BV_{T1} in areas of long T_0. These values are incorrect and reflect failure of the post-processing algorithm which assumes a VIF with a distinct first pass effect such as is seen in the arterial tree (see discussion). In order to avoid errors in the measurement of K_{fp} and BV_{T1}, these parametric images were masked using a threshold value of T_0 (10 s). Tissues supplied by the hepatic portal system are represented by null values (not a number) in the final parametric maps (Figure 5.5). Masked images demonstrate hepatic pixels only where branches of the hepatic artery result in short T_0 or where pathological tumour tissue is supplied by the hepatic arterial system. In two patients with cavernous haemangiomas there was very little perfusion during the first pass and values of BV_{T1} could not be measured. Values of K_{fp} were measurable but were very small. The distribution of median values of K_{fp} and BV_{T1} for all cases is shown in Fig 5.6.

5.3.1 Reproducibility

Comparison of the pixel value distributions of K_{fp} and BV_{T1} from the two investigations in individual patients demonstrated no significant differences in any case. Figure 5.7(A) and (B) illustrates the relationship between median values of K_{fp} and BV_{T1} measured for each of the paired examinations. Figure 5.7(C) and (D) also illustrates the relationship between the upper 5% of pixel values for K_{fp} and BV_{T1} on the two scans. Figure 5.8(A) and (B) illustrates the relationship between tumour volumes measured on the two scans using the manual and semiautomated techniques.

The measures of variance and ratio of the variance for each variable are shown in Table 5.3. *F* statistics show that the potential error on the estimates of variance is expected to be below 85%.

5.4 DISCUSSION

Quantification of the rate of contrast agent leakage provides a potential mechanism for the assessment of capillary endothelial permeability and allows the generation of parametric images that can provide information about the heterogeneity of microvascular function within abnormal tissues [7, 55, 151]. There are many potential methodological approaches but it is important to realize that none is entirely satisfactory [7]. Methods that express the characteristics of contrast leakage rate purely from observed changes in signal intensity are prone to variations in scanning protocol, amplifier gain, injection technique, cardiovascular variation between individuals and other factors [7, 55, 152, 153]. This has led to the development of techniques that use imaging data to derive physiological indicators such as endothelial permeability surface area product (K^{trans}) and relative blood volume (rBV), which should in theory be free from these effects [7]. In principle the calculation of K^{trans} requires accurate measurements of variations in contrast agent concentration with time from the extracellular space within the tissue and from the intravascular space in the blood vessels which supply it. With this data K^{trans} can be calculated simply using eq. 5.4.

Applying these principles to MRI data is complicated by the restrictions imposed by the imaging method. Firstly, the derivation of contrast agent concentration from signal intensity data requires accurate measurement of the T_1 value of the tissue prior to contrast administration which can be technically complex and timeconsuming [32, 154, 155]. Secondly, the measurement of timevarying responses in contrast concentration assumes accurate spatial registration of images throughout the data collection period. Thirdly, the measurement of the temporal variations in the intravascular contrast concentration is complicated by the mechanism of contrast distribution following venous injection [74, 153, 156, 157]. Lastly, the measurement of the temporal variations in contrast concentration in the extracellular, extravascular space is complicated by the need to acquire data from voxels which commonly contain not only permeable capillary beds but also an unknown proportion of medium or large blood vessels [9]. In the liver these problems are further compounded by the presence of a dual vascular supply [146].

The technique we describe uses a series of three T_1-weighted images acquired with varying flip angles to allow calculation of R_{10}. This technique has been described and validated elsewhere [158]. In the liver it proved possible to acquire this set of images in a single breath-hold and the resulting data showed no evidence of misregistration. However, it is not possible to perform this acquisition in the same breath-hold as the dynamic contrast data, so that coregistration of the data sets relies on the patient taking comparable breaths for each scan. It was surprising that we found misregistration of more than one pixel between these scans in only two of 14 studies. In the other studies automated coregistration of the data sets was straightforward and there was no evidence of tissue deformation that would invalidate the use of automated routine rigid body coregistration approaches.

The measurement of changes in the intravascular contrast concentration over time is central to these techniques and requires careful consideration. If a gradual infusion of contrast is used then a relatively low temporal resolution may be adequate. However the use of contrast infusions produces difficulties in attempting to differentiate the effects of intravascular and extravascular contrast agent on signal changes from individual voxels (*vide infra*) [74]. If a bolus injection is used then the contrast concentration changes in the intravascular compartment are complex since the bolus remains compact as it passes around the body and significant peaks of contrast concentration are seen during the first two or even three circulations of the bolus [74, 157]. Once the contrast has undergone two or three circulations (30–40 s) it is uniformly mixed throughout the circulating blood volume. The tissue uptake and renal excretion of contrast during the passage of the bolus will depend on the peak intravascular contrast concentration obtained and the duration of the bolus. Since this peak concentration is transitory this approach demands a very high temporal resolution. We can decrease temporal resolution a little since we know that the profile of the contrast concentration–time course curve will conform to a gamma variate function in normal vasculature. This allows us to use a curve fitting routine to provide data interpolation in the temporal domain and to employ a lower actual temporal resolution than would otherwise be required. In this study we have used a time resolution of approximately 4 s, which is at the upper limit of the acceptable range. The requirement for such high temporal resolution places significant restrictions on the image acquisition protocol and, in particular, restricts the volume and spatial resolution of the acquisition. Despite this, the ability of modern MRI scanners to produce images using very short TR and TE, together with the beneficial effects of volume acquisitions on signal-to-noise ratio has allowed us to image a relatively large volume of tissue at an acceptably high spatial resolution.

The use of high temporal resolution data, combined with a rapid bolus injection allows us to use the shape of the residue function in each voxel to drive a decomposition process which will estimate the contribution of intravascular and extravascular contrast to the observed signal changes [9]. The separation of these effects is important if we desire true measurements of K^{trans} which are not artificially elevated by the presence of intravascular contrast, often referred to as ‘pseudopermeability’. The optimization scheme we have used to decompose the contributions of intra- and extravascular contrast relies on an assumption that the concentrations of contrast due to leakage into the intercellular space during the first passage of the contrast bolus are negligible. This will not be true in tissues with very high extraction fractions and the size of the error due to this assumption is unknown. Very high extraction fractions could lead to the underestimation of K_{fp} and corresponding underestimation of rBV, particularly if the rate of extraction is sufficiently high to generate a peak in contrast concentration in the extravascular space during the passage of the bolus. One way to characterize the magnitude of these potential errors is to compare the results of this technique with estimates of extraction fraction in muscle where the capillary permeability has been extensively examined in both human and animal models and we have found that the first pass technique produces values which are in close agreement with previous studies (unpublished results).

The first pass technique identifies the contributions of intra- and extravascular contrast to signal change by a post-processing algorithm based on the assumption that intravascular contrast concentration changes will show a pattern of temporal variation identical to that seen in the VIF. The algorithm uses features of the VIF (LP and RPR), which are assumed to be constant for any vessel, to estimate the relative contributions of intra- and extravascular contrast. In the liver this assumption is untrue since normal hepatic parenchyma is supplied both by the hepatic arteries and the portal venous system. The characteristics of the contrast changes in these two vascular supplies are very different. The VIF extracted from the hepatic arteries is similar to that seen in the aorta, although slightly delayed and of lower magnitude. The VIF observed in the portal system is significantly delayed and shows a slow progressive rise to a plateau phase with no residual evidence of any first pass bolus. By choosing to use a breath-hold technique we have limited the length of the dynamic acquisition so that it is not possible to measure both the arterial and portal venous VIFs. Furthermore, since the portal venous VIF has lost all traces of the first-pass effect the optimization method we have used would not be able to differentiate between intravascular and extravascular contrast concentration changes. The results of this are that measured values of K_{fp} and BV_{T1} in hepatic tissue supplied by the portal venous system will be unreliable. Furthermore, the algorithm will interpret contrast changes in branches of the portal venous system as representing contrast leakage giving rise to falsely elevated values of K_{fp} and artificially low values of BV_{T1} (Fig. 5.4 and 5.5). This problem is not insoluble since the method we have used is a special case of the expectation-maximization algorithm that avoids the complexities and inherent instabilities of nonlinear optimization approaches [159]. The use of an alternate optimization routine should allow correct measurement of hepatic parenchymal permeability assuming the hepatic portal vein input function can be measured within the data collection period. Despite these problems the differentiation between tissues supplied predominantly by the systemic and arterial circulation and those supplied by the portal venous circulation is made simple by the large time delay between the arrival of arterial and portal venous contrast. The use of the T_0 parameter allows a simple binary classification of voxels and the accuracy with which the contrast changes conforms to the LP provides adequate evidence that the arterial supply is dominant. This has enabled us to produce parametric maps of K_{fp} and BV_{T1} from normal abdominal tissue and from hepatic neoplasms.

In five cases we have been able to repeat the measurements on two occasions, several days apart, without any therapeutic intervention. This has allowed us to calculate the reliability of the technique, which shows that we can expect to confidently detect changes in mean values of K_{fp} and BV_{T1} on the order of 15%, although changes in the upper 5% of the data would need to be on the order of 20%. Although the measurement of tumour volume in the liver is difficult due to poor margination of the tumours on conventional images, the results we present suggest that a change of 10% can be detected with confidence. This can be improved by the use of a semiautomated technique which utilizes the marked differences in T_0 between tumour and normal tissue so that changes of less than 5% can be confidently identified.

The results of this study demonstrate that we can produce high-quality reproducible measurements of tumour volume, endothelial permeability and relative blood volume from hepatic neoplasms that are supplied by the systemic arterial system. This approach offers the benefits of rapid image acquisition allowing breath-hold imaging and provides reproducible independent estimates of K_{fp} and BV_{T1} for each voxel. However it is also clear that the assumptions of the analysis fail in normal liver parenchyma. Furthermore the alteration in the configuration of the contrast concentration profile after passage through the intestinal circulation suggests that the decompositional approach to analysis would not be applicable in normal liver even if the portal VIF could be measured. The development of alternative techniques that address these problems will be challenging. To provide reliable measurements of K^{trans} in both normal liver and hepatic tumours will require independent estimation of BV_{T1} in each voxel to provide regional correction for measurements of K^{trans}. In addition the source of the vascular supply for each voxel must be determined and the data then analysed with the appropriate VIF. This will require separate estimation of the arterial and portal venous VIF functions, which, due to the relative timing of contrast arrival in these two systems, is impossible using breath-hold acquisitions. These restrictions indicate that we will need high temporal resolution data collection that extends from the beginning of the arterial phase until the portal venous contrast concentrations have reached a plateau. This will impose major restrictions on the design of the image acquisition sequence. Possible strategies include the use of navigator echoes to correct for the movements of normal respiration, segmented *k*-space collection to allow reconstruction of data with varying temporal resolution and to support sampling strategies to reduce movement induced blur, and the use of dual echo acquisitions to allow simultaneous collection of data for the estimation of rBV.

In conclusion we have demonstrated that the use of dynamic MRI contrast enhancement combined with a pharmacokinetic model of contrast distribution in the first pass allows us to produce highly reproducible parametric maps of K_{fp} and BV_{T1} from hepatic tumours that are supplied by the hepatic arterial system. The use of T_0 maps allows clear identification of the source of blood supply to each pixel and comparison with the LP indicates whether a mixed blood supply is present. The use of T_0 mapping also improves the reproducibility of tumour volume estimates.

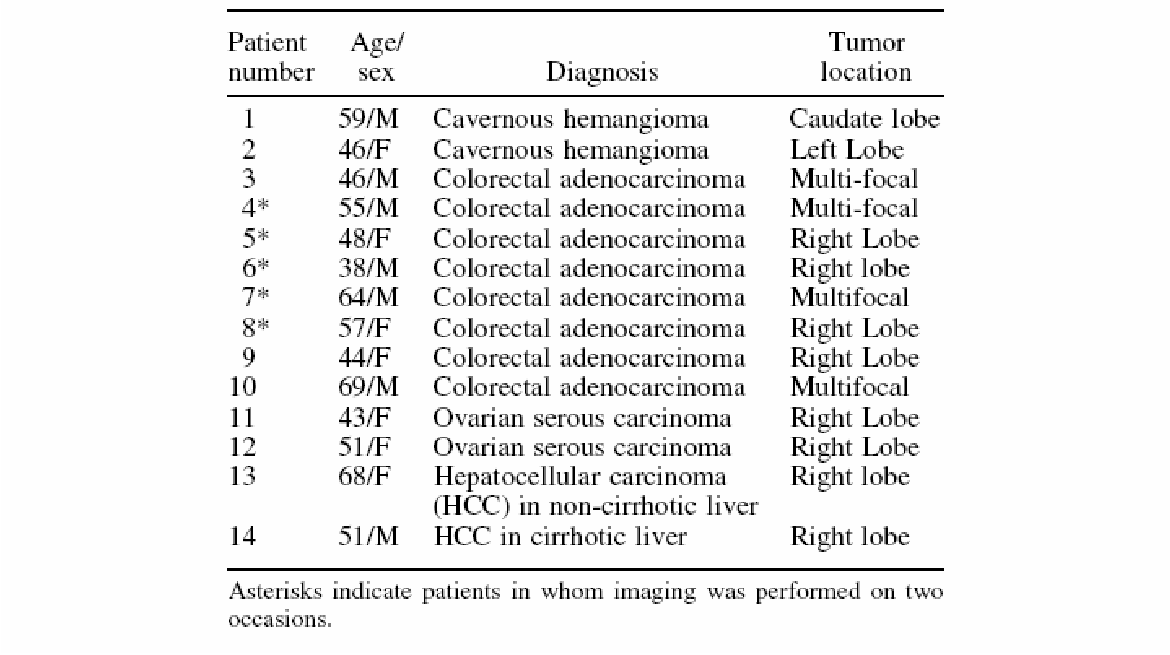

Patient number	Age/ sex	Diagnosis	Tumor location
1	59/M	Cavernous hemangioma	Caudate lobe
2	46/F	Cavernous hemangioma	Left Lobe
3	46/M	Colorectal adenocarcinoma	Multi-focal
4*	55/M	Colorectal adenocarcinoma	Multi-focal
5*	48/F	Colorectal adenocarcinoma	Right Lobe
6*	38/M	Colorectal adenocarcinoma	Right lobe
7*	64/M	Colorectal adenocarcinoma	Multifocal
8*	57/F	Colorectal adenocarcinoma	Right Lobe
9	44/F	Colorectal adenocarcinoma	Right Lobe
10	69/M	Colorectal adenocarcinoma	Multifocal
11	43/F	Ovarian serous carcinoma	Right Lobe
12	51/F	Ovarian serous carcinoma	Right Lobe
13	68/F	Hepatocellular carcinoma (HCC) in non-cirrhotic liver	Right lobe
14	51/M	HCC in cirrhotic liver	Right lobe

Asterisks indicate patients in whom imaging was performed on two occasions.

Table 5.1. Demographic details and diagnoses for 14 patients included in the study

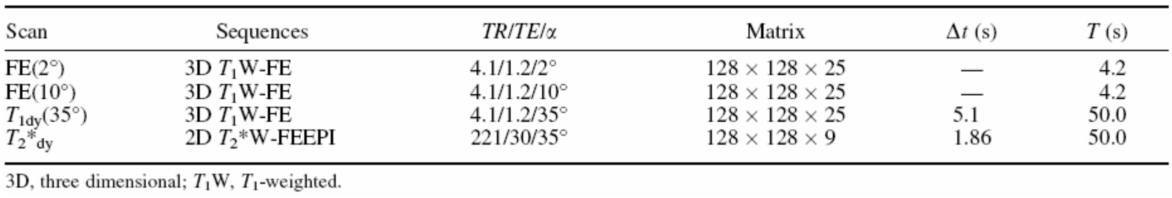

Scan	Sequences	$TR/TE/\alpha$	Matrix	Δt (s)	T (s)
FE(2°)	3D T_1W-FE	4.1/1.2/2°	128 × 128 × 25	—	4.2
FE(10°)	3D T_1W-FE	4.1/1.2/10°	128 × 128 × 25	—	4.2
$T_{1\mathrm{dy}}$(35°)	3D T_1W-FE	4.1/1.2/35°	128 × 128 × 25	5.1	50.0
$T_2{}^*{}_{\mathrm{dy}}$	2D T_2*W-FEEPI	221/30/35°	128 × 128 × 9	1.86	50.0

3D, three dimensional; T_1W, T_1-weighted.

Table 5.2. Imaging sequences, scan parameters, interval between each dynamic phase, Δt (s), and length of scans (T)

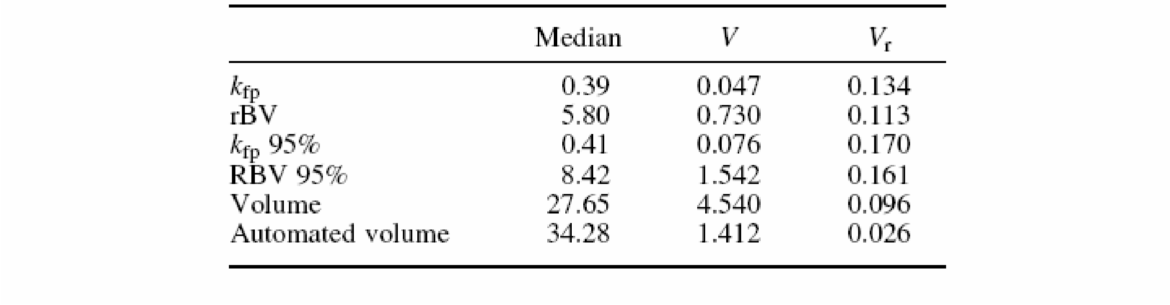

	Median	V	V_r
k_{fp}	0.39	0.047	0.134
rBV	5.80	0.730	0.113
k_{fp} 95%	0.41	0.076	0.170
RBV 95%	8.42	1.542	0.161
Volume	27.65	4.540	0.096
Automated volume	34.28	1.412	0.026

Table 5.3. Measurements of variance (V) and variance ratio (V_r) for repeated measures (n = 5). Column 2 shows median value of measurements for reference

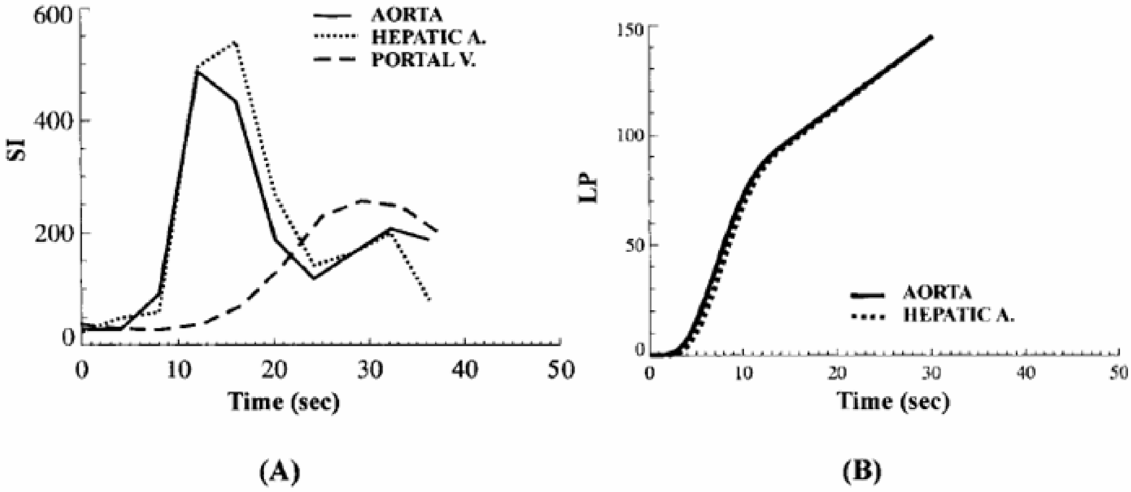

Figure 5.1. (A) $S(t)$ curves from aorta, hepatic artery and portal vein before and after a bolus injection of contrast agent. There is a 12s delay between arterial and portal phases. (B) Normalised integrals of arterial input function (leakage profile) measured from aorta and hepatic artery of right lobe of liver

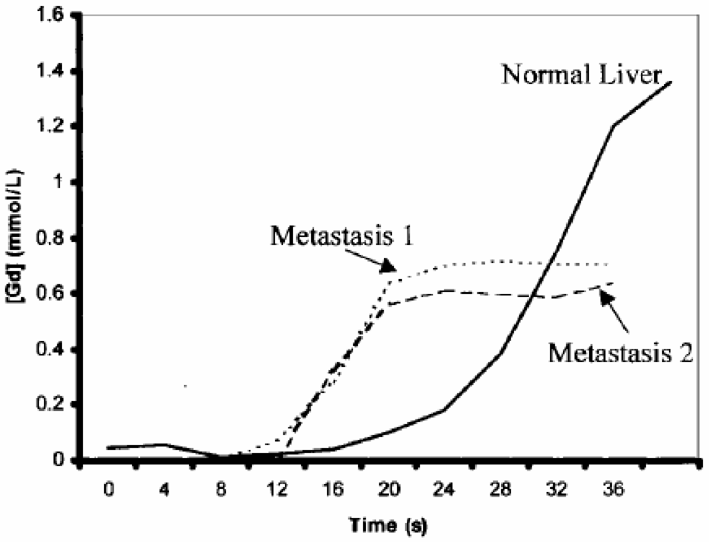

Figure 5.2. Concentration-time course curves from the normal liver and from two metastatic colonic carcinoma deposits (patient 4)

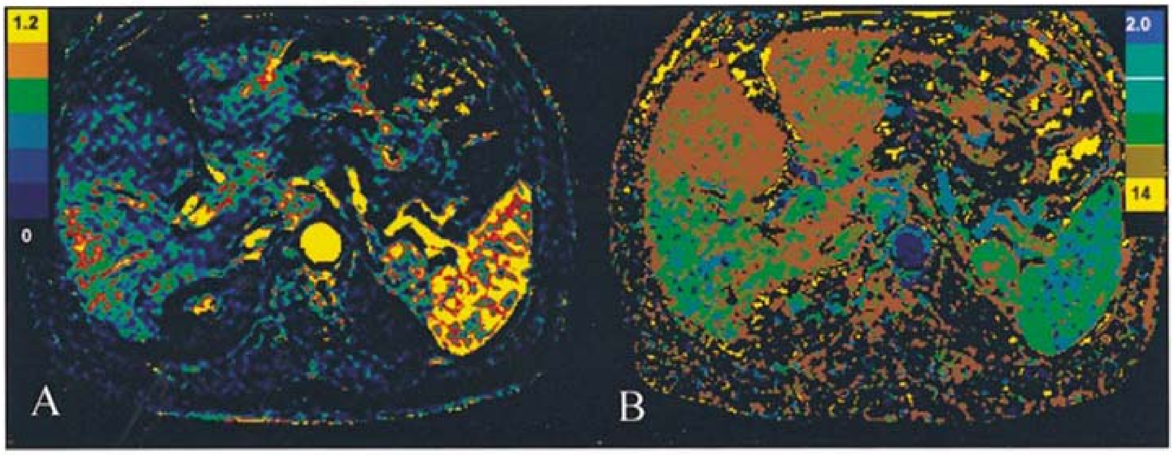

Figure 5.3. A transverse section of liver from K_{fp} (A) and T_0 maps (b) in a patient with hepatoma (patient 14). The T_0 map clearly indicates the early arterial phase (blue), tissue perfusion phase (green) and the late hepatic portal phase (brown)

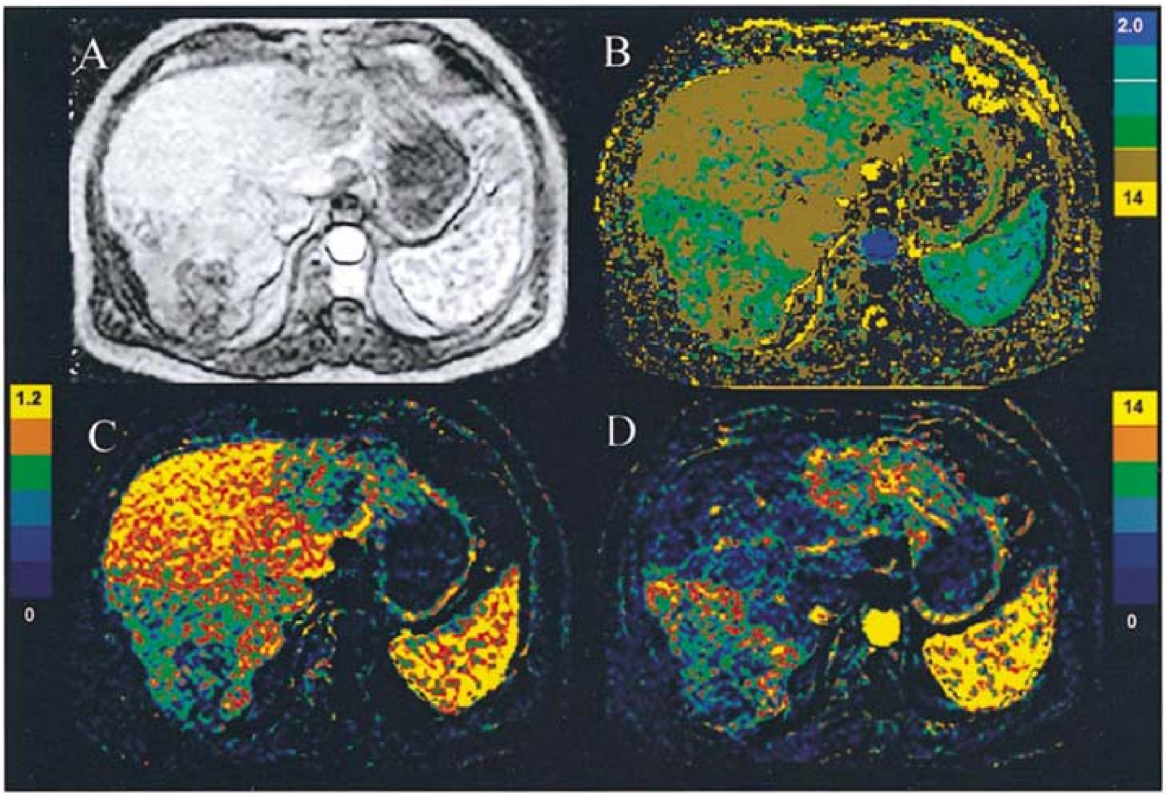

Figure 5.4. Transverse contrast enhanced image from dynamic series (A) and maps of T_0 (B), K_{fp} (C) and BV_{T1} (D) in a patient with metastatic colonic carcinoma (patient 4). Metastatic deposits are seen in the right and left lobes. The T_0 map shows early contrast arrival compared to normal liver in both metastases. Maps of K_{fp} (C) and BV_{T1} (D) show a peripheral rim of high K_{fp} and BV_{T1} in both metastases with low values in the tumour centre. This tumour rim shows K_{fp} values that appear lower than those of normal liver parenchyma and BV_{T1} values that appear higher

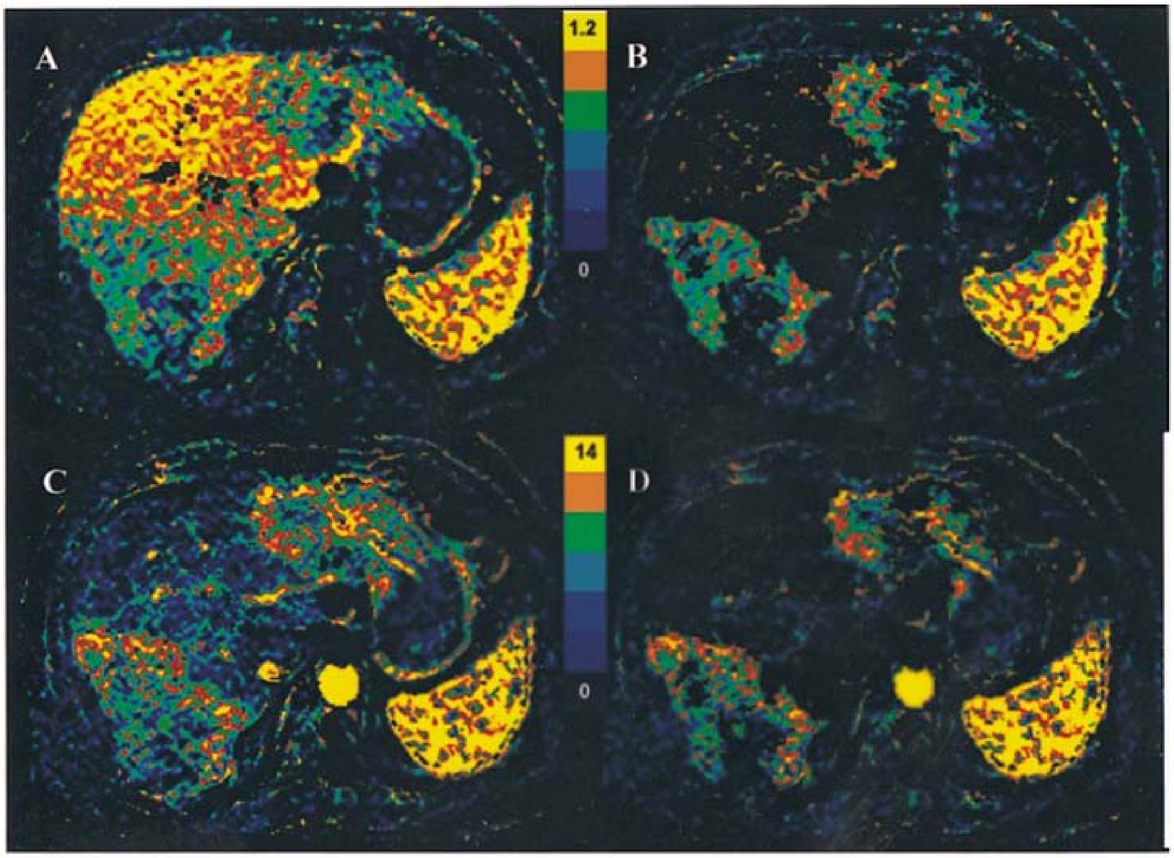

Figure 5.5. Transverse sections of K_{fp} (A and B) and BV_{T1} (C and D) in the patient illustrated in Fig 5.7. The images on the right are generated from the original images on the left by exclusion of pixels with T_0 values in keeping with a portal venous blood supply ($T_0 > 10s$). This removes areas of erroneously elevated K_{fp} and reduced BV_{T1}

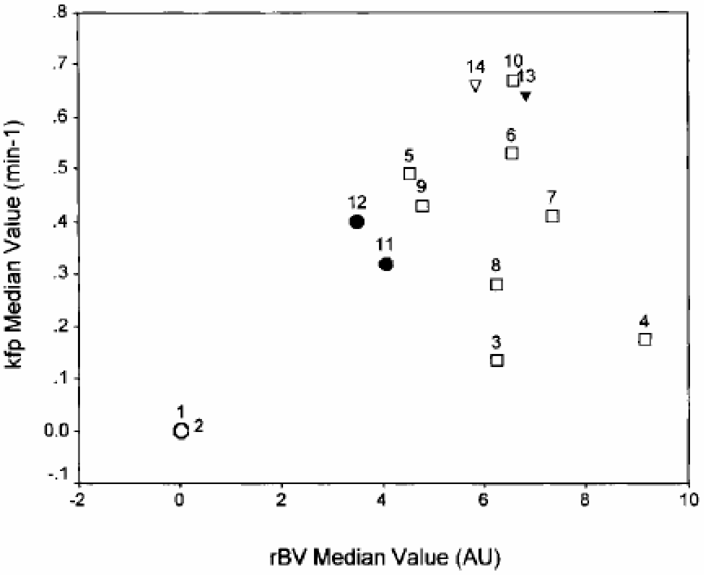

Figure 5.6. Median values of K_{fp} and BV_{T1} from all patients. Patient numbers correspond to Table 5.1. Diagnoses are cavernous haemangioma (open circles), metastatic colonic carcinoma (open squares), metastatic serous carcinoma of the ovary (circles), HCC in cirrhotic liver (open triangle), and HCC in normal liver (triangle). AU = arbitrary units.

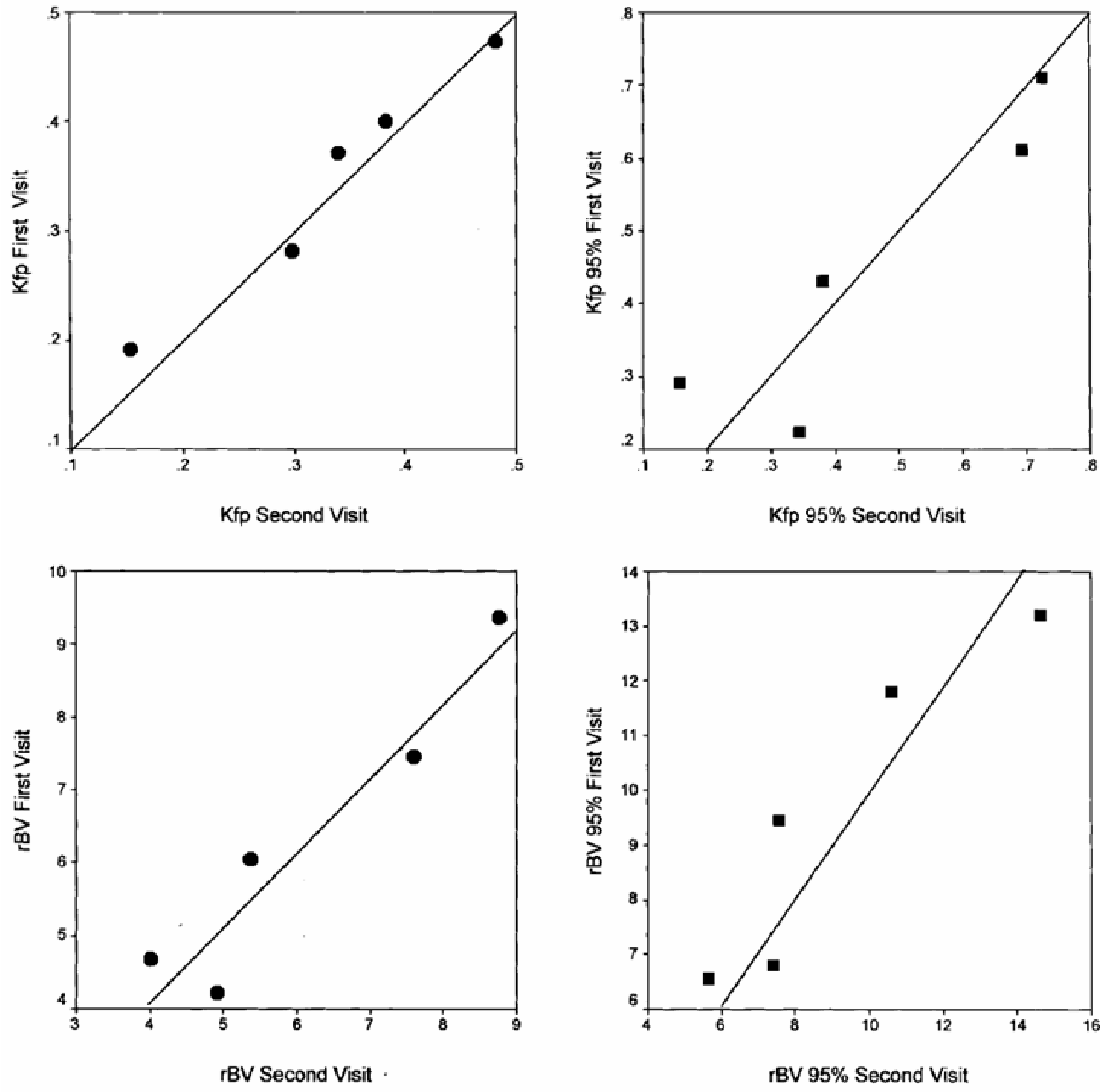

Figure 5.7. Plots showing reproducibility of K_{fp} (top) and BV_{T1} (bottom) values represent median values (left) and median of the upper 5th centile of measurements (right)

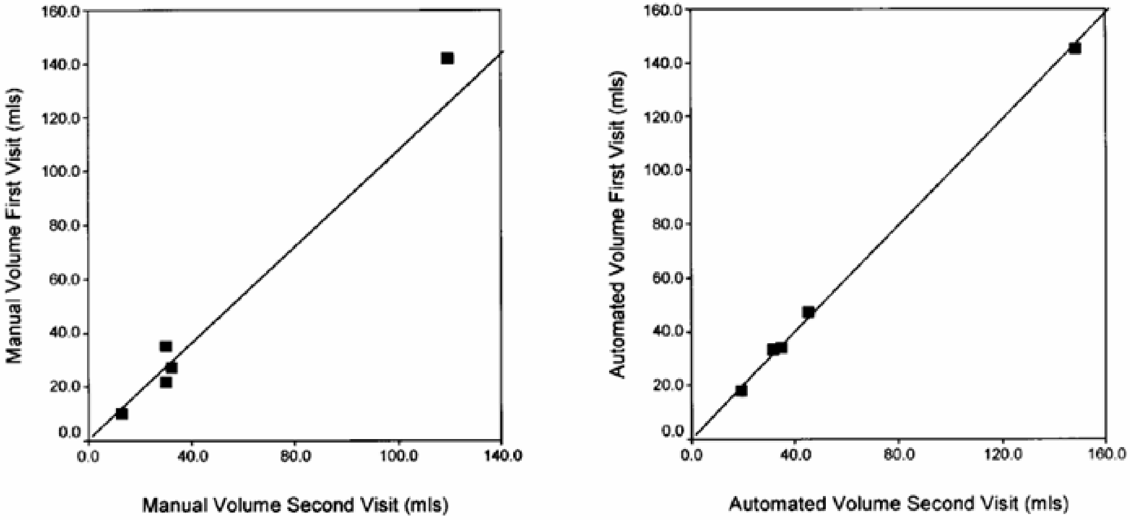

Figure 5.8. Plots showing reproducibility of tumour volume measurements using manual (left) and semi-automated (right) techniques. Lines represent perfect agreement

CHAPTER 6 :

DYNAMIC CONTRAST-ENHANCED MAGNETIC RESONANCE IMAGING IN THE EVALUATION OF HUMV833 ANTI-VEGF ANTIBODY

This Chapter is based on [77].

6.1 INTRODUCTION

Vascular endothelial growth factor (VEGF) has been identified as one of the most potent angiogenic cytokines [160]. Thus the development of antiangiogenic agents has focused largely on the inhibition of VEGF. A number of strategies have been used to inhibit the biologic activity of VEGF, including antibodies to the cytokine or its signalling receptors [161, 162]. These antibodies have so far shown evidence of antitumour activity in an early clinical trial. One anti-VEGF antibody with early preclinical promise is HuMV833, a humanised version of a mouse monoclonal anti-VEGF antibody (MV833), with antitumour activity demonstrated against a broad spectrum of human tumour xenografts [163].

Many trials have sought pharmacokinetic endpoints for antiangiogenic agents that lack a dose-limiting toxicity [164]. However, these trials often use *ex vivo* measurements to evaluate the pharmacokinetic response. So far, studies of the intratumoural concentration of and biological response to antiangiogenic agents have not been reported.

An interdisciplinary study was carried out [77] to investigate the distribution and biologic effects of HuMV833 in tumour patients in a phase I clinical trial, for the European

Organisation for the Research and Treatment of Cancer (EORTC). Four centres participated: Christie Hospital, Manchester, UK; Academisch Ziekenhuis Maastricht, Maastricht, The Netherlands; Universitair Medisch Centrum Utrecht, Utrecht, The Netherlands; and Linkoping University Hospital, Linkoping, Sweden. Positron emission tomography (PET) imaging with ^{124}I-HuMV833 was employed to determine radiological uptake and clearance by both tumour and normal tissue. The *in situ* biological response was determined by application of a first pass analysis technique on dynamic contrast-enhanced (DCE) magnetic resonance imaging (MRI) to estimate the volume transfer coefficient, K^{trans}. K^{trans} is a measure of volume transfer from intravascular to extravascular extracellular space, and can thus relate to endothelial permeability-surface area product in microvasculature. The blood-brain barrier ensures that $K^{trans} \approx 0$ in normal brain, and so a significant K^{trans} measurement reflects pathology. However, outside the brain, it is common for normal tissue to show significant measures of K^{trans}, but areas with relatively elevated K^{trans} values would be evidence for active angiogenesis. Vascular endothelial permeability is promoted by the VEGF cytokine, and since HuMV833 inhibits VEGF expression *in vitro*, it was hypothesised that a reduction in microvascular endothelial permeability (and therefore K^{trans}) would be observed. We have applied a non-conventional first pass leakage profile pharmacokinetic analysis method to the DCE-MRI data to obtain estimates of K^{trans}, and therefore refer to our measures of K^{trans} as K_{fp}. Using only the first pass phase of contrast bolus to calculate K^{trans} (or K_{fp}) allows the implementation of breath-hold techniques when imaging in the abdomen to reduce motion artefact.

This chapter focuses on the MRI contribution to this phase I clinical trial of HuMV833.

6.2 MATERIALS AND METHODS

A cohort of patients was included in this study that satisfied the eligibility criteria for the trial. All had solid tumours, either in the thoracic region (predominantly hepatic metastases) or in the pelvic region (e.g. ovarian carcinoma). The protocol was written by G. Jayson on behalf of the European Organization for Research and Treatment of Cancer (EORTC) Biological Therapeutic Development Group and was approved by the EORTC protocol review committee (EORTC 13992). HuMV833 was supplied by Protein Design Labs., Inc., and approved by the medicines control agency in each participating country. Approval was gained from the local research ethics committee of each centre. All patients gave written informed consent and the trial was performed according to Good Clinical Practice regulations. The project was also approved by the U.K. Administration of Radioactive Substances Advisory Committee (ARSAC).

Two imaging protocols were used for acquiring the required DCE-MRI data, dependent on which region the tumour was located. Since time-course imaging in the thorax would suffer from motion artefact due to breathing effects, we employed a validated breath-hold first pass acquisition method for tumours located in the thoracic region [65]. Breathing effects were not considered to cause significant motion artefact in the pelvic region, so the same first pass acquisition method was employed for tumours in this region as for the brain [9].

MR imaging was performed on a 1.5 T Philips ACS NT-PT6000 scanner, using the body coil, with maximum gradient strength of 23 mT/m and maximum slew rate of 105 mT/m/ms (Philips Medical Systems, Best, The Netherlands). Prior to the MR examination a 16G catheter was inserted into an antecubital vein using local anaesthetic (lignocaine, s.c.). Routine pre-contrast T_1- and T_2-weighted and post-contrast T_1-weighted images were acquired to allow identification of the tumour. All images were acquired in the axial plane.

For the pelvic region the imaging protocol for dynamic contrast enhanced studies consisted of three consecutive 3-D radiofrequency (rf) spoiled (T_1-weighted) field echo acquisitions with flip angles ($\alpha = 2$, 10 and 35°) to allow calculation of baseline T_1 maps. The third flip angle imaging sequence was repeated to produce a T_1-weighted dynamic data set with a time resolution of 5.1 seconds and a duration of 1 minute. Contrast agent (0.1 mM/kg of gadodiamide: Gd-DTPA-BMA; Omniscan™, Nycomed, Oslo) was given intravenously by power injector over a period of 4 seconds via a 16-gauge cannula inserted into an antecubital vein as the imaging sequence commenced and was immediately followed by a bolus of 35 ml of normal saline injected at the same rate.

For the thoracic region the imaging protocol for dynamic contrast enhanced studies consisted of three consecutive 3-D rf-spoiled (T_1-weighted) field echo acquisitions with an array of flip angles ($\alpha = 2$, 10 and 35°) to allow calculation of baseline T_1 maps. The third sequence was repeated ($n = 9$, duration $T = 24.6$ s) for baseline acquisition. The same sequence was then repeated to produce a T_1-weighted dynamic data set with a time resolution of 4.1 seconds and a duration of 41 seconds. Contrast agent (0.1 mmol/kg of Gd-DTPA-BMA) was given as a manual intravenous bolus injection over a period of 4 seconds and was immediately followed by a bolus of 35 ml of normal saline injected at the same rate. The injection was started as the dynamic imaging sequence was initiated. The images were all collected during breath holding. The first three images providing the variable flip angle data were collected in one breath-hold (19 s) and the baseline images were collected in a second breath-hold (18 s). The dynamic enhancement data was collected using a 41 s data acquisition and the patient was asked to hold their breath for as long as was comfortable during this acquisition. Data for the analysis is adequate if the data collection covers the initial pre-contrast baseline to the first two collection points after the recirculation bolus. This can be achieved in as little as 25 s if the timing of the bolus arrival and the image collection coincide. Additional data collected after the patient begins to breath was easily identified by the presence of movement artefact and was discarded.

In order for the data to be correctly analysed the image datasets must all spatially co-register. However, asking a patient to take a deep breath and hold it on a series of scans carries the possibility of the patient not holding their breath at the same depth every time and therefore causing spatial difference in successive scans. The spatial positions of the liver in the three separate breath-hold acquisitions were compared by performing spatial coregistration of the hepatic component of each data set to the baseline scan. The coregistration algorithm chosen uses a calculation of the dot product of gradient edge strengths and is therefore suitable for comparison of images with divergent contrast characteristics. The transformation matrices from the coregistration procedure were used to identify patients with significant misregistration (greater than one voxel in any direction) between the breath-hold sequences. Misregistration of this magnitude was seen in two cases and misregistered data was realigned using a scaled sinc kernel.

All patients were rehearsed in the MR protocol immediately prior to the examination. Patients were not imaged at any specific time of day and no attempt was made to control their dietary intake prior to scanning.

Analysis of image data was carried out by applying a first pass leakage profile [9] pharmacokinetic model, to generate estimates of the transfer constant K^{trans} [7] from first pass dynamic data – K_{fp} – and blood volume from the same T_1-weighted data – BV_{T_1}.

Image data were analyzed in four steps. First, dynamic data were reviewed to exclude patients who moved substantially during image acquisition. Second, baseline maps of baseline T_1 were calculated by using the three images with varying flip angles. Third, an arterial input function (AIF) was manually identified from the dynamic series. Fourth, relative tumoural blood volume and K_{fp} were calculated pixel by pixel for the entire data set on the basis of the changes in contrast concentration during the first passage of the contrast bolus. The calculation of K_{fp} and relative tumoural blood volume uses an iterative fitting technique that decomposes the intra- and extravascular components of the signal change during the passage of the contrast bolus.

The AIF was measured on MR-DCE images either in the descending aorta, for thoracic tumours, or in a femoral artery, for tumours in the pelvic region. These blood vessels were the major supplying vessels for the tumours of interest. There is evidence that hepatic neoplasms are supplied by the hepatic arterial system (fed by the descending aorta) rather than the portal venous system, which supplies normal hepatic parenchyma [65].

An expert radiologist defined regions of interest (ROI) of tumour. The ROIs were subsampled to exclude non-enhancing tissue by identifying pixels that showed a signal increase of 20% or greater between pre- and post-contrast T_1-weighted magnetic resonance scans. These ROIs were then applied to parametric maps to extract mean and standard deviations of K_{fp} and relative tumoral blood volume.

The trial was an open label, multiple dose, dose escalation phase I study in which the antibody was administered in 0.9% saline (up to 250 mL) over 1 hour on days 1, 15, 22, and 29. Four dose levels were administered: 0.3, 1, 3, and 10 mg/kg. Patients partaking in the antibody trial were imaged with MR on day 0 (before treatment), day 2 (after initiating treatment) and day 35. The patients were imaged in the same location in each visit centred on the tumours they had. Measurements of K_{fp} and BV_{T_1} were taken on each visit from the defined ROIs. Parametric maps provided the ability to visually appreciate changes from one visit to another in a particular section of a patient across the whole section imaged.

6.3 RESULTS

Twenty patients were entered into this phase I study to evaluate the distribution and biologic effects of HuMV833. The median age of the patients was 51.5 years. Six of the patients included in the study had been diagnosed with colorectal cancer, five with ovarian cancer, two with breast carcinoma, two with melanoma, one with angiosarcoma, one with neuroblastoma, one with laryngeal cancer, one with osteosarcoma, and one with metastatic carcinoma of unknown primary. All patients had undergone initial surgery and had received chemotherapy and/or radiotherapy, depending on their disease. Of the 20 patients, four patients were treated with HuMV833 at dose level 1 (0.3 mg/kg), six at dose level 2 (1 mg/kg), six at dose level 3 (3 mg/kg), and four at dose level 4 (10 mg/kg). Nineteen patients were evaluable.

VEGF is known to regulate vascular endothelial permeability and HuMV833 inhibits VEGF *in vitro*, thus we hypothesised that HuMV833 would reduce vascular permeability *in vivo*. Magnetic resonance determinations of K_{fp}, related to the microvascular endothelial permeability-surface area product, were performed before treatment, 48 hours after treatment, and at day 35 (6 days after the final drug administration).

We successfully obtained good quality dynamic contrast enhanced magnetic resonance images from all patients, having either thoracic or pelvic imaging protocols. Any minor misregistration between consecutive image datasets in a single visit were realigned using sinc reslicing. Parametric images from all patients were of good quality without movement and artefact. Parametric images from thoracic acquisitions appear more smoother and anatomically better defined, mainly due to the dominance of the liver and presence of kidneys and other organs in the axial sections being homogeneous in normal tissue. Parametric images from pelvic acquisitions are much more sparse and structure/anatomy are difficult to perceive. Tumour was very clear in liver and other thoracic tissues but not always easily discernible in tissues within the pelvic region.

Representative color-rendered K_{fp} maps of a liver metastasis are shown in Figure 6.1. In Fig. 6.1(B) the hepatic metastasis in the left lobe of this patient's liver is easily observed as a patch of green reflecting elevated K_{fp} values as compared to the normal liver tissue in blue, before the initiation of anti-VEGF treatment. In Fig. 6.1(C) the same section is shown from the same patient 48 hours after the initiation of anti-VEGF treatment. The majority of the elevated K_{fp} green patch has now diminished to the lower K_{fp} blue level of normal liver tissue, directly demonstrating (visually) the dramatic reduction in vascular endothelial permeability due to the anti-VEGF antibody. The patient's left kidney also showed areas of elevated and very high (red) K_{fp} values compared to the right kidney in Fig. 6.1(B), but the left kidney shows no significant reduction in K_{fp} in Fig. 6.1(C) on this patient's second visit even after administration of anti-VEGF antibody. It was discovered that there was an inflammation, and not a tumour, in the left kidney causing the increased endothelial permeability, not promoted by VEGF.

We detected changes in tumoural K_{fp} in all patients at each of the antibody doses, as shown in Figure 6.2. All patients had a substantial decrease in K_{fp} at 48 hours (median: 44%; range: 5%–91%). Absolute values of K_{fp} varied greatly from one patient to another, with an order of magnitude difference in baseline (pre-treatment values). We did not observe a dose–K_{fp} relationship between patients receiving different antibody dose levels (Fig. 6.2). However, when we examined the data for a particular patient, the K_{fp} value at 48 hours in 11 of 12 measurements in individual patients was less than that at 35 days, which is consistent with a concentration–response relationship. Fig. 6.2, also shows that, unlike K_{fp} responses at higher antibody doses, the change in K_{fp} at a dose of 0.3 mg/kg at 48 hours was not sustained on the day 35 scan.

The PET and magnetic resonance data obtained allowed us to test the hypothesis that regional vascular permeability was associated with the antibody localization in the tumor. In Figure 6.3 are illustrated the results of affine image co-registration performed between magnetic resonance-derived maps of K_{fp} and PET data in a woman with a pelvic deposit of ovarian cancer. The presence of the pelvic girdle in the images facilitates registration of these images. The data show that the distribution of antibody, as estimated by PET, was qualitatively associated with the regional vascular endothelial permeability and the distribution of K_{fp}. A quantitative analysis of this co-registered data was precluded by differences in axial rotation and nonlinear distortions.

6.4 DISCUSSION

There has been a worldwide research program to develop antiangiogenic agents for the treatment of cancer. Many families of antiangiogenic drugs now exist, but their clinical development has been hampered by a paucity of data concerning the optimum biologically active dose. In addition, although the classical phase I study design focuses on toxicity as an endpoint to establish the maximum tolerated dose, many humanised monoclonal antibodies have no clinically significant toxicity, which precludes identification of the maximum tolerated dose. Furthermore, biologic dose–response relationships may follow a bell-shaped curve [165], and therefore the maximum tolerated dose may not even be the best dose for clinical applications. To overcome these issues, biologic pharmacokinetic and pharmacodynamic investigations [166] have entered phase I clinical trial design with the goal of establishing the optimum biologically active dose. However, the present study has shown that tumor deposits, even within the same patient, can behave differently with respect to drug uptake, drug clearance, and biologic response. Thus, it is difficult to establish a standard dose in the way that is practiced for most cytotoxic agents.

Advanced magnetic resonance imaging and algorithms were used to measure K_{fp}, which reflects both local blood flow and vascular permeability surface area product, a parameter that is controlled by VEGF, and one we anticipated would decrease if the antibody were biologically active. We had previously shown these algorithms to be reproducible [65], and the differences in pretreatment versus maximum reduction in K_{fp} that we recorded here exceeded 15%, which was the established coefficient of variance for liver metastases, suggesting that the antibody was biologically active. The K_{fp} maps of the patients' tumours showed distinct anatomic variation, suggesting that K_{fp}, and therefore perhaps VEGF activity, varies from one area to another. The variability was noticeable not only within tumours but also between patients, because the baseline permeability measurements across all patients varied by a factor of 10.

Taken together with the PET-pharmacokinetic data, these data reveal a marked variation in functional anatomy and pathophysiology within human tumors. The implication is that it is inappropriate to compare the biologic response of a patient with one tumor histology, treated with a particular dose of antibody, with another patient with another or even the same tumor type who received a different dose. The difference in biology may prevent any observation of a dose–response effect. If pharmacokinetic and pharmacodynamic endpoints are to be used to identify the optimum biologically active dose, then two strategies may be needed to deal with these functional anatomic issues. The variation in biology could be controlled for by treating a cohort of patients with an intra-patient dose escalation strategy and applying the pharmacokinetic measurements to the same tumor mass, which is thereby exposed to different antibody concentrations. Such a cohort would not replace the existing phase I trial design, which identifies pharmacodynamics (including saturation of clearance upon prolonged exposure), dose-limiting toxicity, and the maximum tolerated dose but would be an additional part of the phase I trial design and one that might be appropriate for cytostatic antiangiogenic agents. Data from this study support the adoption of this intra-patient dose escalation strategy because greater permeability (K_{fp}) changes were seen 48 hours after the initiation of treatment than were seen at day 35, 6 days after the fourth treatment, implying that there is a concentration–response relationship within patients. A second strategy, which may be more suitable for drugs that have a long half-life with respect to tumor growth, would be to reduce the heterogeneity among patients by using stricter selection criteria and entering larger numbers of patients into conventional cohort-based phase I trials. Such selection parameters might include tumor histology, tumor size, and tumor location. This type of approach was used in an investigation of a VEGF receptor tyrosine kinase inhibitor [166, 167] that revealed a dose–permeability relationship in the liver metastases of patients with metastatic colon carcinoma.

This study has revealed striking variation in human tumor behavior within individual patients, which may account for apparent resistance to antiangiogenic antibody therapies. Our observations have implications for future studies of cytostatic antiangiogenics agents.

Whether it will be necessary to tailor individual therapy regimens to individual patients can be determined only in a randomized trial that compares the maximum tolerated dose-guided therapy with pharmacodynamically determined dosing.

DCE-MR imaging has made a very valuable contribution to this phase I trial. Using a suitable pharmacokinetic analysis model it has allowed us to make *in vivo* measurements of K_{fp} and thereby estimate directly the localised biologic effect of the anti-VEGF antibody on the endothelial permeability of the microvasculature in lesions. The ability to produce images makes the observation of the heterogeneous and distributed biological effect clear and easily observable. This clinically important information is complimentary to the distributional information of the antibody available from PET. Where a significant uptake concentration is observed with PET there also is observed regions of significantly high K_{fp}, demonstrating that the HuMV833 antibody was indeed targeting areas of increased angiogenesis promoted by VEGF (see Fig. 6.3). The subsequent decrease in K_{fp} in the same areas was also clearly evident in post-treatment data. Therefore the use of DCE-MRI and the K_{fp} parameter in the pharmacokinetic evaluation of the HuMV833 anti-VEGF antibody in our cohort of tumour patients has been vital in the biological conclusions drawn by this trial study, which would not have been possible otherwise. We have established the role of DCE-MRI in clinical trials. Hence, the use of DCE-MRI and appropriate pharmacokinetic analysis would be strongly encouraged for such studies in the future, if appropriate facilities are available.

We have conducted this trial study on a multicentre level. Since the measurements we have taken using MR data were quantitative it was essential that the hardware, software and sequences on the MR scanners in the centres involved were compatible, and the protocol is implemented in the same way across all. This required setting-up visits and regular contact with the centres, and was difficult to maintain. For example, one centre that sent MR data for analysis had used a surface phased array coil for receiving MR signal rather than the scanner's body coil. Using a surface coil means that the signal received is inhomogeneous and dependent on the phase array position and coil gain. This can be advantageous radiologically as better signal-to-noise can be obtained in the tissue of interest when the receive coil is nearer to it. However the problems are in quantifying the data, when the coil gain and the relationship between signal drop-off and distance from the coil are not known it is impossible to correct for the spatial dependence of the actual signal, and therefore the change of signal with the arrival and departure of contrast agent in the blood is undeterminable. This was the case with the Philips Scanners used in participating centres, which do not give satisfactory scaling factors for their phased array coils. Also, it is advisable to ensure that the same contrast agent is used as the relaxivity of the contrast agent is a factor used in the calculation of contrast concentration, and that the same dosage is injected for every scan with the same delivery for consistency of data quality (i.e. signal-to-noise). The benefit of running a trial in multiple centres is the increased number of patients that can be recruited and a greater likelihood of having tumours in the areas of interest.

The software we used to derive estimates of K_{fp} has *a priori* assumptions built-in to simplify the calculation process and these had to be met by the data received for it to be analysable. These assumptions include MR field strength, relaxivity of contrast agent, contrast agent dosage, bolus injection of contrast agent, data acquisition at a temporal resolution that allows the shape of the first pass of bolus to be identified, and the use of the breath-hold acquisition technique in the abdomen. Field MR field strength, contrast agent relaxivity and dosage could be adjusted for if known. As well as making sure that MR scanner hardware was compatible between centres, it was also essential to make sure the scanners in the centres were of high enough specification to be able to acquire the data at the necessary speed and quality. This requirement made some sites unsuitable to be included.

This was the first time DCE-MRI has been used to assess the effectiveness of an anti-VEGF antibody in a clinical trial. More recently, as a subsequent study to our own, another group have employed DCE-MRI as a novel biomarker in a phase one clinical trial of PTK787/ZK 222584 [166], which is a VEGF receptor antibody [167]. This study conducted on metastatic liver disease from primary colonic carcinoma used measurement of the bi-directional transfer constant K_i. These workers found significant negative correlations between the percentage of baseline K_i and the increase in oral dosage and plasma levels.

The first PET-pharmacodynamic study of an antiangiogenic agent was undertaken in this trial, using the anti-VEGF antibody HuMV833 radiolabelled with ^{124}I. Thus we have made the very first simultaneous assessment of the distribution and clearance of an anti-VEGF antibody, using PET, and its biologic effect, using MRI.

Magnetic resonance imaging offers the safest method for repetitive scans of human patients, having no risk associated with ionising radiation, unlike X-ray computed tomography (CT), nuclear medicine and PET. Fast MR imaging and computational modelling techniques allow the estimation of important pharmacokinetic parameters that are reliable and reproducible. We have used the speed available on modern scanners to acquire the required first-pass data in breath holds and avoid the motion artefacts inherent in abdominal imaging.

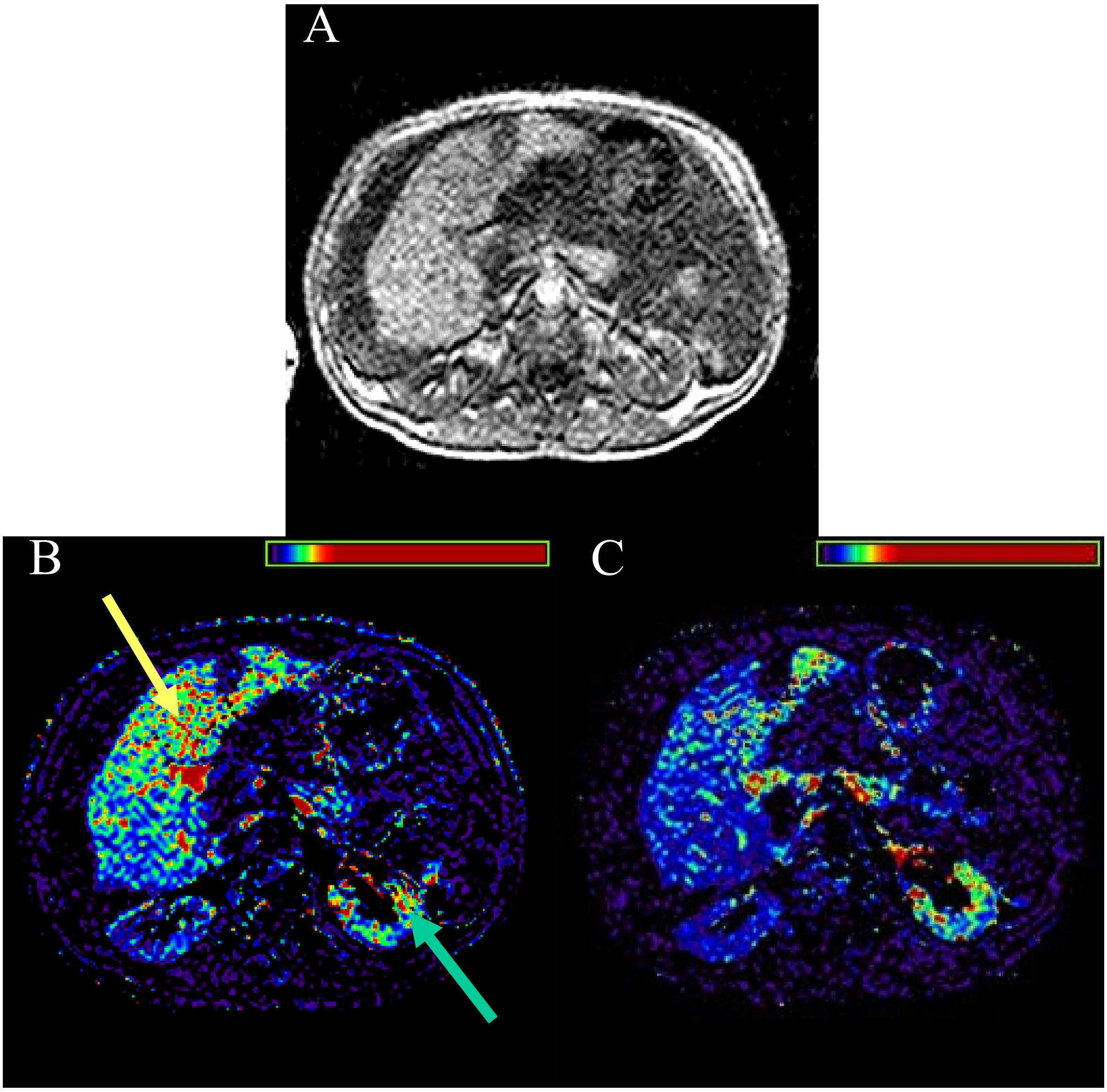

Figure 6.1. Magnetic resonance images were used to determine tumour endothelial permeability surface area product K_{fp} before (B) and after (C) patients were treated with the humanised antivascular endothelial growth factor (VEGF) antibody HuMV833. Representative images are shown in (B) and (C). A) A 10° flip-angle pre-contrast T_1-weighted magnetic resonance image acquired before treatment at the same location as B. B) The magnetic resonance imaging-derived map showing the K_{fp} of a metastasis (yellow arrow) in the left lobe of the liver in a patient before receiving HuMV833 (1 mg/kg). C) The magnetic resonance imaging-derived map showing the vascular permeability of the same metastasis from the same patient 48 hours after receiving HuMV833. The areas of green and blue represent high and low vascular permeability, respectively. Red and yellow pixels represent artefactually high measurements in the hepatic vein. The left kidney (green arrow) showing high values of K_{fp} in B and C was discovered to be a renal inflammation, presenting no response to the HuMV833 administered.

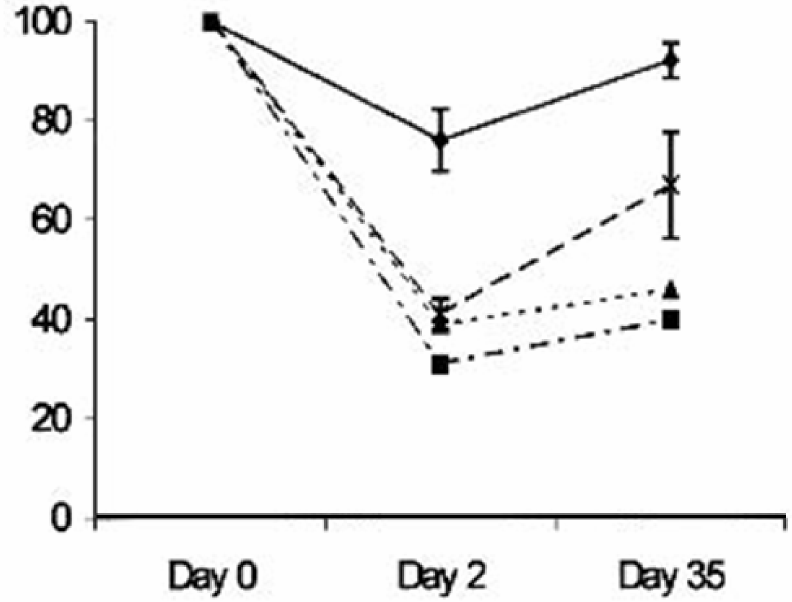

Figure 6.2. The K_{fp} of representative tumours was determined for all patients before treatment, 2 days after the first treatment was initiated, and 35 days after the first treatment was initiated. The vascular permeability of the tumour after treatment was compared with that before treatment, and the data were expressed as the mean percent change relative to the value before treatment for each different treatment dose level, with 95% confidence intervals. Each treatment dose level is represented by a different symbol. Solid diamonds 0.3 mg/kg; solid squares 1 mg/kg; solid triangles 3 mg/kg; crosses 10 mg/kg. K_{fp} (min^{-1}) reflects vascular endothelial permeability.

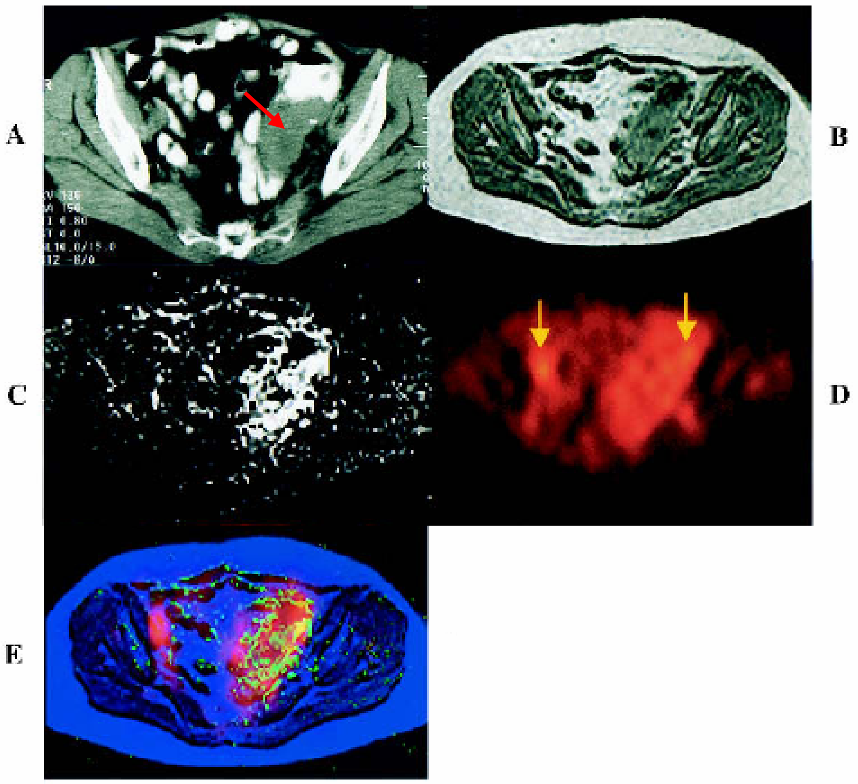

Figure 6.3. Co-registration (superimposition) of positron emission tomography (PET)–pharmacodynamic and magnetic resonance–pharmacokinetic measurements. Axial images through the same level of the pelvis of a woman with a deposit of ovarian cancer who received the humanised anti-vascular endothelial growth factor (VEGF) antibody HuMV833 (10 mg/kg) are shown. A) A contrast-enhanced X-ray computed tomographic scan image with a deposit of ovarian cancer identified (red arrow). B) A 10° flip-angle pre-contrast T_1-weighted magnetic resonance image of the same region of the pelvis as shown in A. C) The vascular permeability (K_{fp} [min^{-1}]) map of the same section of the pelvis. High vascular permeability is represented by white pixels. The tumour is the most permeable structure in the pelvis. D) The PET distribution of HuMV833 in same region of the pelvis as shown in A. The symmetrical uptake (yellow arrows) of antibody in the pelvis results from antibody in the femoral vessels. E) The co-registered (merged) images of T_1-weighted magnetic resonance are shown in blue, the magnetic resonance-determined vascular permeability in green, and the PET-determined antibody distribution in red.

CHAPTER 7 :

GENERAL DISCUSSION

Dynamic contrast enhanced (DCE) imaging is a rapidly developing area in the field of magnetic resonance imaging (MRI). The potential of deriving physiological parameters by the application of pharmacokinetic models to DCE-MRI data has lead to an overwhelming amount of interest in these techniques. This is indicated by the large number of groups becoming involved in this area around the world and the growing number of publications that have appeared since the techniques were first described. Studies have largely centred on: 1) The scientific and methodological aspects of DCE-MRI, and the accuracy and reproducibility of the derived physiological parameters. 2) The application of the derived physiological parameters to the clinical evaluation of disease states, such as diagnosing the grade and type of tumours. The studies presented in this Thesis span these categories.

We have concentrated our studies on K_{fp} – the volume transfer constant (K^{trans}) from the First Pass Leakage Profile (FP) pharmacokinetic model of Li et al. [9] – and CBV_{T_1} – cerebral blood volume estimates from the same model. The FP model allows both parameters to be estimated simultaneously, by iterative voxelwise time-course decomposition, from the same T_1-weighted DCE-MRI data collected during the first pass of contrast bolus following intravenous injection [66]. A high temporal resolution but short DCE-MRI data acquisition is required for this technique.

Our studies have shown that K_{fp} and CBV_{T_1} offer independent biological information about microvasculature in tumours. In gliomas K_{fp} estimates have been shown to be more accurate than conventional K^{trans} measures, due to their typically low extraction fraction, although both correlated well in areas dominated by extravasated contrast concentration

[70]. CBV_{T_1} has been shown to be a better predictor and discriminator between glioma grades than K_{fp}, which supports many previous studies but is in contrast to some recently reported ones (as demonstrated in Chapter 3). We have also demonstrated that CBV_{T_1} maps give the same biological information as CBV maps conventionally obtained from T_2*-weighted images, but that CBV_{T_1} maps offer higher spatial resolution, 3D volume coverage, do not suffer from susceptibility artefacts, and are corrected for extravasated contrast in tumour tissue, making CBV_{T_1} maps ideal for surgical and radiotherapy planning. Due to the short time course required for the FP model, we have successfully implemented a breath-hold acquisition for collection of motion-free first pass DCE-MRI data in patients with liver metastases, and have shown the high reproducibility of K_{fp} and CBV_{T_1} measurements in this technique [65]. Finally, we have applied the FP model to DCE-MRI data collected in patients with abdominal tumours before and after treatment with an anti-VEGF (anti-angiogenic) antibody (HuMV833), as part of a pre-clinical phase I trial, and have established the crucial role that pharmacokinetic analysis can play in measuring the biological effect of anti-angiogenic drugs *in vivo*, having seen localised decreases in K_{fp} intrinsically related to VEGF expression where the antibody has taken affect [77].

Pharmacokinetic modelling of DCE-MRI data has found major application in anti-angiogenic drug trials. Thus the development of pharmacokinetic modelling techniques has been largely driven by the requirements of the pharmacological industry. Many of the anti-angiogenic drug trials were in pre-clinical phase I stages, where a deep appreciation of the biological mechanisms of the drug needed to be gained. This relied on complex models and complex analysis methods to yield as many independent parameters related to biological features as possible. However, at the present time, phase I trials of anti-angiogenic drugs are becoming less common and these are now moving into phase II and phase III clinical trials in anticipation of commercial use. In these phases of clinical trial the pharmacological industry is no longer interested in complex biological information concerning their drug but about its overall effectiveness in inhibiting angiogenesis. Pharmacokinetic modelling of DCE-MRI still has the same role to play in these multi-centre trials, which requires good stability across multiple centres and the ability to implement data acquisition and analysis on many different machines. Since simpler information on a drug's general effectiveness is necessary, the models required to provide this information are also much simpler. A retrogressive development has taken place in that basic methods such as IAUC (initial area under the curve), Brix's model or Tofts' model are increasingly being implemented in these clinical trials because substantial changes in measured parameters are expected in the measured parameters [168]. Due to the simplicity of the techniques used the measured parameters will represent a mixture of a number of biological characteristics that will be inseparable, such as microvascular endothelial permeability-surface area product (PS), blood flow, blood volume and the size of the extravascular extracellular space (EES) [73]. This approach seems adequate to measure large changes in vascular characteristics to satisfy drug trial requirements. For example, one group investigating the biological effect of an inhibitor of the VEGF receptor tyrosine kinases (PTK787/ZK 222584) in patients with advanced colorectal cancer and liver metastases [166, 167] used a DCE-MRI protocol involving acquisition of single slice gradient echo images and analysis of regions of interest only, using Tofts' model. It seems that the errors introduced with this methodology (such as undersampling of the tumour volume, movement, undersampling tumour heterogeneity, no measured AIF) were not considered significant factors in the study. At the same time, however, this move towards simpler techniques for DCE-MRI based studies has lead to the emergence in the scientific community of a new area of interest in understanding the underlying mechanisms involved in signal changes observed, which is having an impact in other areas of application.

Clinicians have been impressed by the potential of DCE-MRI and pharmacokinetic modelling, particularly for the *in vivo* characterisation of pathological tissues. The requirements of clinicians are in contrast with those of the pharmacological industry. Clinicians are interested in the value of the physiological parameters derived from pharmacokinetic modelling of DCE-MRI data for differentiating the type of a tumour, for grading them, for determining prognosis for the tumour patient, and for planning treatment. They are therefore interested in complex modelling approaches that generate parameters related to real, distinct, separate physiological factors and in the relationship that might exist between these parameters and the clinical assessment of tumours. On the other hand the time for collecting data and the expertise for analysing the data are both restricted in the clinical environment. Thus the methods for DCE-MRI acquisition and pharmacokinetic analysis must be fast, efficient, simple and robust. The first three experimental chapters of this Thesis address these issues in depth.

Due mainly to the developments of DCE-MRI and pharmacokinetic methods for clinical trials, there has been a great deal of emphasis placed on the general reproducibility and extensibility of these methods for implementation in multiple centres. The First Pass Leakage Profile model of Li et al. is one of very few techniques for which the reproducibility has been established [9, 66, 76, 78]. It is noticeable that physiological parameter values reported in the literature from different groups using different pharmacokinetic models and various acquisition protocols in brain tumours show a wide range of values for tumour type and within glioma grades, although a general trend can be seen of higher CBV and K^{trans} values being observed as the grade of a glioma increases (but this is not true in every study). Amongst all the literature to date, CBV seems to be the most diagnostically useful in terms of distinguishing between glioma grades, particularly between the higher grades (grade III and grade IV), which is certainly what we have shown. Why is this so important? Histopathological analysis of tumours is carried out because the histological grade of tumour is related to prognosis and more importantly to the choice of effective treatment. However, the conventional procedure of taking a biopsy sample from a brain tumour for histopathological analysis, by drilling a hole through a patient's skull and inserting needles, is a highly invasive procedure accompanied by many risks in terms of damage to healthy brain tissue, etc. More importantly, the heterogeneity of (especially high grade) tumour tissue means that, the sample taken is not guaranteed to be a representative portion of tumour tissue, which should preferably be from the part that is the most histologically aggressive. Imaging potentially offers a completely non-invasive alternative for this conventional procedure. A relationship between parameters from pharmacokinetic modelling and tumour grade would mean that DCE-MRI could be used to grade tumour tissue using parametric maps, thereby allowing spatially-varying grading in-keeping with tumour heterogeneity. Parametric maps could then also be used to guide radiotherapy and/or surgical resection in order to target the procedure accordingly, and to spare normal, healthy tissue. However, it seems that, just as grading a tumour histologically involves different features of the tumour tissue as observed under the microscope, no one parameter from pharmacokinetic analysis can clearly distinguish glioma grade. However, use of a combination of parameters can improve specificity. The real physiological relationship of the parameters obtained also has to be better understood. K^{trans} is often quoted as being "microvascular endothelial permeability", as it has been in this Thesis, but it is not always. Under low blood flow K^{trans} reflects flow, but under high blood flow K^{trans} is a product of endothelial permeability and endothelial surface area [73]. Thus K^{trans} is a mixture of extraction fraction and flow [73]. We have successfully shown decomposition of our measurements into independent estimates of CBV and K_{fp} [66, 76]. To separate flow from K^{trans} requires more complex modelling. Buckley et al. [169] used the pharmacokinetic model of St. Lawrence and Lee [6] to analyse the DCE-MRI time-course data from gliomas, which allowed estimation of blood flow, extraction fraction, permeability, blood volume and extravascular extracellular volume as separate parameters. This involves defining ROIs in enhancing portions of tumour and measuring overall values – however this analysis technique is not stable enough to produce parametric maps. The values obtained showed that when flow, blood volume and permeability-surface area product were separated out that flow actually showed a much stronger correlation with histological grade than either blood volume or permeability [169]. The vast heterogeneity in the parametric values obtained from high grade tumours, both within individual tumour tissue and among mean/median values from glioblastomas, is observed to reduce among permeability values when flow is separated. However this technique is very sensitive to signal-to-noise and temporal resolution in the acquired data so the results are not dependable. There is a clear need to develop this technique to make it more robust and capable of generating parametric maps, as much information could be added to the characterisation of tumour tissue.

A major problem with multi-parametric analysis is the high occurrence of fitting errors because of the number of parameters being estimated on a voxelwise basis from a single (usually signal) time-course. Pharmacokinetic models generally use time-course data (signal or contrast concentration) in purely vascular voxels to drive the fitting procedure in tissue voxels – the arterial (or vascular) input function (AIF). The form of the AIF is essential to providing an accurate estimation of the contrast concentration time-course in the vascular compartment to allow accurate estimation of the contribution of the interstitial space to the contrast concentration in tissue voxels. We have found that the acquisition sequence and temporal resolution for data collection have a striking affect on the AIF that can be obtained. Also, the site where the AIF is measured has an impact on the pharmacokinetic analysis. As shown in Chapter 2 with the model of Tofts and Kermode [52], many of the conventional (or conventionally-based) models assume that the AIF follows a biexponential form [45, 53, 54, 157]. This results from low temporal resolution data acquisition which was common when these techniques were developed. This meant that contrast concentration measurements over time in an artery were in effect an averaging of time-course features. With improvements to the hardware and software of modern scanners, sequences with high temporal resolution can be implemented, and acquired DCE data shows that the contrast concentration time-course in the major vessels actually demonstrates phases in the first 30 seconds after injection of contrast bolus. A first pass peak is observed as the bolus makes its initial journey throughout the body's vasculature, and then recirculation occurs causing a second much less pronounced peak, due to leakage and mixing in the blood, followed by a steady clearance. Low temporal resolution imaging causes these peaks to be smoothed out, and a biexponential curve fitted to such data means that the gamma-variate shape of the first pass peak is seriously underestimated with the clearance portion being fitted best [73]. Underestimating the vascular contrast concentration time course in the first pass phase leads to overestimation of K^{trans}, since intravascular contrast concentration will be attributed to extravasated contrast [73]. As presented in Chapter 2, the FP technique uses high temporal resolution data up to the recirculation phase and uses a gamma-variate function to fit to the first pass peak only (hence this model's name), which results in a more accurate fit to the time points, giving a better estimation of intra- and extravascular contributions to intravoxel contrast concentration. The other consideration for AIFs is the site where they are measured. It would be ideal to measure the AIF from an artery feeding the tumour tissue, but it is rarely possible to identify the feeding artery in every dataset. Therefore it is commonplace to measure the AIF from a major artery, or even a vein, that is easily identifiable in every dataset for consistency. In the datasets we analysed we used the superior sagittal sinus to measure our AIF from. In some of the very early models an AIF was not measured individually, but a standard AIF was employed which was taken from published data based on blood samples taken at various time intervals to measure the amount of Gd-DTPA [56]. Measuring the AIF from a vein means that the first pass peak will be broader and delayed, but this was adjusted for by the FP algorithms [9]. The acquisition technique is a major factor affecting the AIF measurement, because in-flow effects, susceptibilities, T_1 saturation, water shift effects, etc., have to be considered. For example, when we measured our AIF from the superior sagittal sinus we would always avoid measuring it in slices near either end of the acquired volume in order to minimise the likelihood of in-flow and other effects. One group has used the spleen to measure their input function [170] (which they term the vascular normalization function (VNF)) claiming that the reproducibility is much better than if an artery is used as commonly done. However the VNF shown by this group contains none of the phases or features characteristic of intra-vascular contrast bolus passage clearly seen in the AIF that they compare it with [170].

It is worth stating here that DCE imaging has also been implemented on X-ray CT scanners and pharmacokinetic modelling has been applied to CT data [171-174]. From the imaging perspective the problems and artefacts associated with MRI do not apply to CT imaging. Simple subtraction of pre-contrast images from contrast-enhanced images gives the distribution of contrast agent and the signal measured is directly proportional to concentration. The development of multi-slice CT has made contrast-enhanced volume acquisitions possible. However, the most important consideration with CT is the radiation dosage, therefore a compromise has to be made between anatomic coverage and the number of repeated scans to follow the time course of the contrast medium. The same problems for pharmacokinetic analysis remain with CT as with MRI. Also, a limited number of visits for rescanning with CT would be possible in a given time period, for example in a study of the effectiveness of an anti-angiogenic agent in reducing K^{trans}, simply because of the cumulative radiation that the patient would be exposed to (radiation generates free radicals *in vivo* which can cause tumours). In the clinical environment there seems to be a move towards using CT to characterise tumours at presentation rather than using MRI, possibly because of MRI scans being rather protracted and relatively expensive and CT images being much easier to interpret by clinicians. Nevertheless the radiation dosage with CT and all the benefits and potential for development with MRI will mean that MRI can never be replaced by CT and the scientific work, of which this Thesis demonstrates a fraction, will continue in MRI research.

A large body of the literature suggests that in order to obtain estimates of the volume transfer constant (K^{trans}) and blood volume (BV) it is necessary to acquire two DCE datasets, one T_1-weighted to calculate K^{trans} and the other T_2*-weighted to calculate BV. We have demonstrated that this is not necessary when using the FP pharmacokinetic model [43]. From a single, short, volumetric T_1-weighted DCE dataset it is capable of generating maps of K_{fp} and BV corrected for contrast leakage. K_{fp} maps correlate well with conventional K^{trans} measurements in voxels dominated by extravasated contrast, and CBV maps from the FP method demonstrate the same biological information as conventional CBV maps from T_2*-weighted maps. This is a major benefit of the FP technique. Due to the short time-course of data that is required for analysis with the FP model it is not possible to derive estimates for v_e (the intravoxel fractional volume of extravascular extracellular space) using this technique [9, 76] – a good estimate requires enough time for the extravascular extracellular volume (in tumour tissue) to fill with contrast agent. The clinical role of v_e is, as yet, unknown. v_e estimates have been shown to vary between different tumour types, but its actual clinical value requires careful investigation.

Modelling and simulation have shown that the FP model's assumption that C_e is negligible during the first pass of contrast bolus causes K_{fp} to underestimate true K^{trans} when true K^{trans}/v_e is high (i.e. when K^{trans} is large and/or v_e is small) [73, 76]. Specifically, when true K^{trans} is approximately 0.2 min^{-1} or larger then K_{fp} is systematically underestimated. Recognising this, a new pharmacokinetic method has been proposed, known as the "Hybrid" technique [76]. This technique uses the FP model as well as a two-compartment multiparametric curve-fitting (MPCF) model to estimate values of K^{trans}. The two-compartment model that is fitted to by the MPCF technique is given by [76]

$$C(t) = K^{trans} C_p(t) \otimes e^{-\frac{K^{trans}}{v_e}t} + v_p C_p(t) \qquad \textbf{7.1}$$

Monte Carlo modelling has shown that MPCF gives better accuracy of K^{trans} estimates when true K^{trans} is high (approximately greater than 0.1 min^{-1}) [76]. The Hybrid method uses the properties of both methods to ensure accuracy in the parameters estimated across a wide range of values. A threshold is used so that pharmacokinetic parameter values below the threshold are derived from the FP method and those above from the MPCF technique. The threshold value was determined from a collection of simulation studies. Initially first-pass DCE data is analysed using the FP method, with the leakage profile (LP) calculated ignoring backflow, and then subsequently analysed with the MPCF method taking the initial parameter estimates from the FP results and the shape of the tissue uptake curves. If K^{trans} from the FP method is lower than the threshold then it is accepted as the final result, otherwise the fitted K^{trans} from the MPCF technique is accepted. Where the fitted K^{trans} from MPCF are large enough to assume that fitted v_e values are accurate, then K^{trans} and v_e from MPCF are output. These values are then used to recalculate the leakage profile to include backflow given by[76]

$$LP = \int_0^t C_p(t') \cdot e^{-\frac{K^{trans}}{v_e}(t-t')} dt' \qquad \textbf{7.2}$$

This modified LP is then used to drive an improved decomposition of the intra- and extravascular contributions to the tissue residue function by repeating the FP analysis. Systematic underestimation of K^{trans} by the FP model when backflow of contrast medium from extravascular space to the plasma space during the first pass of contrast bolus cannot be ignored should be surmounted by applying the modified LP. Further details on the Hybrid method can be found in [76]. However, the conventional MPCF method was found to be affected by "covariance" (or fitting) errors that are more significant with low SNR, which may be particularly significant when the technique is used for pixel-by-pixel fitting, and could result in parameters being derived that have no bearing on real physiology. Conversely, the FP method is highly reproducible and less affected by low SNR, but it does underestimate K^{trans} at higher values (higher than approx. 0.2 min^{-1}) [76]. Thus the Hybrid method, using a combination of both models, implemented on the basis of initial parameter estimates, is able to achieve higher precision and accuracy across a wide range of values. Much work is required for assessing this technique further but it offers significant benefits for clinical applications, especially because DCE data is required to be collected only during the first pass of contrast bolus [79].

The main basis in the development of the First Pass Leakage Profile (FP) model was the iterative process for decomposing voxel-wise contrast concentration time courses into intra- and extravascular components based on shape analysis [66]. This means that the temporal data could be split into two data streams instead of just one, and so, for example, instead of having five parameters to fit to a single data stream only two would need to be fitted to the intravascular data stream to estimate CBV and three would need to be fitted to the extravascular data stream to estimate K^{trans} (or K_{fp}). This reduces the false minima steps, lowering the probability of mis-fitting pixels, and increases statistical stability, which has been shown. In the experimental chapters of this Thesis we have demonstrated the advantages and validity of the FP method under various applications. We have shown that K_{fp} and CBV are independent parameters that give comparable biological information to conventional pharmacokinetic models [70]. When true K^{trans}/v_e is low then K_{fp} is an accurate estimate of K^{trans}, better than K^{trans} from conventional models [70, 73]. The decomposition process allows the FP method to distinguish those voxels that are dominated by intravascular contrast concentration preventing erroneously high estimation of K^{trans} as is observed with conventional models. We have shown that some features of the distribution of K_{fp} and CBV in glioma tissue do have a relationship with histological grade. We have successfully acquired good quality breath-hold data and have applied the FP method to generate maps of K_{fp} and CBV [65], which have not been done previously. Finally, we have successfully applied the FP method in a clinical drug trial and observed significant reductions in K_{fp} under the action of an anti-angiogenic antibody, which was verified by PET and haematologic data [77]. Much work has gone on, and continues to go on, to validate the FP method, and the Hybrid method, by our centre, both by simulation and Monte Carlo modelling and by application to *in vivo* DCE data in various disease states. It would be fair to say that, although conventional models like that of Tofts and Kermode [52] are well published and extensively used, the First Pass Leakage Profile technique has been one of the most thoroughly scrutinised and tested.

Having successfully separated the volume transfer constant and blood volume into two independent parameters, a major remaining “Holy Grail” is to separate flow from K^{trans}. This is possible at present [6] but not stably enough for pixel-by-pixel analysis [169]. We would hope to see in the future a method similar in approach to the FP model that is able to decompose the time course further to estimate flow as well. And in like manner to the FP method, this must be statistically stable, highly reproducible, reduces the number of fitting parameters, applicable to 3D data acquisitions, yield pixelwise parametric maps covering the whole volume, and applicable to data capable of being acquired on many different scanners at many different sites. The goal of having a simple and fast piece of software that can apply a reliable pharmacokinetic model to DCE-MRI data and generate a comprehensive and accurate set of physiologically-related parametric maps is still a long way from being realised.

REFERENCES

1. Folkman, J., *Endothelial cells and angiogenic growth factors in cancer growth and metastasis. Introduction.* Cancer Metastasis Rev, 1990. **9**(3): p. 171-4.
2. Folkman, J., *What is the evidence that tumors are angiogenesis dependent?* J Natl Cancer Inst, 1990. **82**(1): p. 4-6.
3. Folkman, J., *Role of angiogenesis in tumor growth and metastasis.* Semin Oncol, 2002. **29**(6 Suppl 16): p. 15-8.
4. Thurston, G. and Gale, N.W., *Vascular endothelial growth factor and other signaling pathways in developmental and pathologic angiogenesis.* Int J Hematol, 2004. **80**(1): p. 7-20.
5. Ziche, M., Donnini, S., and Morbidelli, L., *Development of new drugs in angiogenesis.* Curr Drug Targets, 2004. **5**(5): p. 485-93.
6. St Lawrence, K.S. and Lee, T.Y., *An adiabatic approximation to the tissue homogeneity model for water exchange in the brain: I. Theoretical derivation.* J Cereb Blood Flow Metab, 1998. **18**(12): p. 1365-77.
7. Tofts, P.S., Brix, G., Buckley, D.L., Evelhoch, J.L., Henderson, E., Knopp, M.V., Larsson, H.B., Lee, T.Y., Mayr, N.A., Parker, G.J., Port, R.E., Taylor, J., and Weisskoff, R.M., *Estimating kinetic parameters from dynamic contrast-enhanced T(1)-weighted MRI of a diffusable tracer: standardized quantities and symbols.* J Magn Reson Imaging, 1999. **10**(3): p. 223-32.
8. Hinshaw, W.S., Andrew, E.R., Bottomley, P.A., Holland, G.N., and Moore, W.S., *Display of cross sectional anatomy by nuclear magnetic resonance imaging.* Br J Radiol, 1978. **51**(604): p. 273-80.
9. Li, K.L., Zhu, X.P., Waterton, J., and Jackson, A., *Improved 3D quantitative mapping of blood volume and endothelial permeability in brain tumors.* J Magn Reson Imaging, 2000. **12**(2): p. 347-57.
10. *What is cancer?* CancerBACUP, 2003, http://www.cancerbacup.org.uk/Aboutcancer/Whatiscancer/Whatiscancer
11. Kaye, A.H. and Laws, E.R., Jr, *Brain Tumors: An encyclopedic approach*. Second ed. 2001, London: Churchill Livingstone.
12. *Clinical considerations.* Pennsylvania State University, 2004, http://www.bmb.psu.edu/courses/bisci004a/nerve/nerveb4.htm
13. Kleihues, P., Burger, P.C., and Scheithauer, B.W., *The new WHO classification of brain tumours.* Brain Pathol, 1993. **3**(3): p. 255-68.
14. Kleihues, P., Louis, D.N., Scheithauer, B.W., Rorke, L.B., Reifenberger, G., Burger, P.C., and Cavenee, W.K., *The WHO classification of tumors of the nervous system.* J Neuropathol Exp Neurol, 2002. **61**(3): p. 215-25; discussion 226-9.
15. Asano, M., Yukita, A., Matsumoto, T., Hanatani, M., and Suzuki, H., *An anti-human VEGF monoclonal antibody, MV833, that exhibits potent anti-tumor activity in vivo.* Hybridoma, 1998. **17**(2): p. 185-90.
16. *About Liver Cancer.* RITA Medical Systems, Inc., 2004, http://www.livertumor.org/about.asp
17. *Cancer of Liver.* Tirgan, 2004, http://www.tirgan.com/hepatoma.htm
18. *Liver Metastasis.* Tirgan, 2004, http://www.tirgan.com/livermts.htm
19. *Angiogenesis Foundation: Understanding Angiogenesis.* The Angiogenesis Foundation, 2004, www.angio.org/understanding/understanding.html
20. *Understanding Angiogenesis.* National Cancer Institute, 2004, http://press2.nci.nih.gov/sciencebehind/angiogenesis/angio00.htm
21. Folkman, J., *Tumor angiogensis: role in regulation of tumor growth.* Symp Soc Dev Biol, 1974. **30**(0): p. 43-52.

22. Greenblatt, M. and Shubi, P., *Tumor angiogenesis: transfilter diffusion studies in the hamster by the transparent chamber technique.* J Natl Cancer Inst, 1968. **41**(1): p. 111-24.
23. Amoroso, A., Del Porto, F., Di Monaco, C., Manfredini, P., and Afeltra, A., *Vascular endothelial growth factor: a key mediator of neoangiogenesis. A review.* Eur Rev Med Pharmacol Sci, 1997. **1**(1-3): p. 17-25.
24. Ferrara, N., *Vascular endothelial growth factor and the regulation of angiogenesis.* Recent Prog Horm Res, 2000. **55**: p. 15-35; discussion 35-6.
25. De Coene, B., Hajnal, J.V., Gatehouse, P., Longmore, D.B., White, S.J., Oatridge, A., Pennock, J.M., Young, I.R., and Bydder, G.M., *MR of the brain using fluid-attenuated inversion recovery (FLAIR) pulse sequences.* AJNR Am J Neuroradiol, 1992. **13**(6): p. 1555-64.
26. Buckley, D.L. and Parker, G.J.M., *Measuring contrast agent concentration in T1-weighted dynamic contrast-enhanced MRI*, in *Dynamic Contrast-Enhanced Magnetic Resonance Imaging in Oncology*, A. Jackson, D.L. Buckley, and G.J.M. Parker, Editors. 2004, Springer-Verlag: Heidelberg.
27. Springer, C.S., Jr, in *NMR in Physiology and Biomedicine*, R.J. Gillies, Editor. 1994, Academic Press: San Diego. p. 75-100.
28. *MR Contrast Medium.* Amersham Health, 2004, http://www.amershamhealth.com/medcyclopaedia/medical/volume%20i/mr%20contrast%20medium.asp
29. *Magnetic Resonance Technology Information Portal.* Softways, 2004, http://www.mr-tip.com/serv1.php?type=db1&dbs=Contrast%20Agents
30. Gowland, P. and Mansfield, P., *Accurate measurement of T1 in vivo in less than 3 seconds using echo-planar imaging.* Magn Reson Med, 1993. **30**(3): p. 351-4.
31. Rosen, B.R., Belliveau, J.W., Vevea, J.M., and Brady, T.J., *Perfusion imaging with NMR contrast agents.* Magn Reson Med, 1990. **14**(2): p. 249-65.
32. Donahue, K.M., Burstein, D., Manning, W.J., and Gray, M.L., *Studies of Gd-DTPA relaxivity and proton exchange rates in tissue.* Magn Reson Med, 1994. **32**(1): p. 66-76.
33. Judd, R.M., Atalay, M.K., Rottman, G.A., and Zerhouni, E.A., *Effects of myocardial water exchange on T1 enhancement during bolus administration of MR contrast agents.* Magn Reson Med, 1995. **33**(2): p. 215-23.
34. Wedeking, P., Sotak, C.H., Telser, J., Kumar, K., Chang, C.A., and Tweedle, M.F., *Quantitative dependence of MR signal intensity on tissue concentration of Gd(HP-DO3A) in the nephrectomized rat.* Magn Reson Imaging, 1992. **10**(1): p. 97-108.
35. Matthaei, D., Frahm, J., Haase, A., Merboldt, K.D., and Hanicke, W., *[FLASH-tomography. A rapid imaging procedure for magnetic resonance tomography].* Dtsch Med Wochenschr, 1986. **111**(23): p. 909-14.
36. Bluml, S., Schad, L.R., Stepanow, B., and Lorenz, W.J., *Spin-lattice relaxation time measurement by means of a TurboFLASH technique.* Magn Reson Med, 1993. **30**(3): p. 289-95.
37. Parker, G.J., Baustert, I., Tanner, S.F., and Leach, M.O., *Improving image quality and T(1) measurements using saturation recovery turboFLASH with an approximate K-space normalisation filter.* Magn Reson Imaging, 2000. **18**(2): p. 157-67.
38. Freeman, A., Gowland, P., Jellineck, D., Wilcock, D., Frith, J., Worthington, B., Mansfield, P., and Ratcliffe, G. *Application of fast T1 mapping using LL_EPI.* in *Proc Soc Magn Reson*. 1994. San Francisco, CA.
39. Fram, E.K., Herfkens, R.J., Johnson, G.A., Glover, G.H., Karis, J.P., Shimakawa, A., Perkins, T.G., and Pelc, N.J., *Rapid calculation of T1 using variable flip angle gradient refocused imaging.* Magn Reson Imaging, 1987. **5**(3): p. 201-8.

40. Wang, H.Z., Riederer, S.J., and Lee, J.N., *Optimizing the precision in T1 relaxation estimation using limited flip angles.* Magn Reson Med, 1987. **5**(5): p. 399-416.
41. Hittmair, K., Gomiscek, G., Langenberger, K., Recht, M., Imhof, H., and Kramer, J., *Method for the quantitative assessment of contrast agent uptake in dynamic contrast-enhanced MRI.* Magn Reson Med, 1994. **31**(5): p. 567-71.
42. Brookes, J.A., Redpath, T.W., Gilbert, F.J., Murray, A.D., and Staff, R.T., *Accuracy of T1 measurement in dynamic contrast-enhanced breast MRI using two- and three-dimensional variable flip angle fast low-angle shot.* J Magn Reson Imaging, 1999. **9**(2): p. 163-71.
43. Zhu, X.P., Li, K.L., Kamaly-Asl, I.D., Checkley, D.R., Tessier, J.J., Waterton, J.C., and Jackson, A., *Quantification of endothelial permeability, leakage space, and blood volume in brain tumors using combined* T_1 *and* T_2** *contrast-enhanced dynamic MR imaging.* J Magn Reson Imaging, 2000. **11**(6): p. 575-85.
44. Evelhoch, J.L., *Key factors in the acquisition of contrast kinetic data for oncology.* J Magn Reson Imaging, 1999. **10**(3): p. 254-9.
45. Parker, G.J., Suckling, J., Tanner, S.F., Padhani, A.R., Revell, P.B., Husband, J.E., and Leach, M.O., *Probing tumor microvascularity by measurement, analysis and display of contrast agent uptake kinetics.* J Magn Reson Imaging, 1997. **7**(3): p. 564-74.
46. Parker, G.J.M. and Buckley, D.L., *Tracer kinetic modelling for T1-weighted dynamic contrast-enhanced MRI*, in *Dynamic Contrast-Enhanced Magnetic Resonance Imaging in Oncology*, A. Jackson, D.L. Buckley, and G.J.M. Parker, Editors. 2004, Springer-Verlag: Heidelberg.
47. Crone, C., *The Permeability Of Capillaries In Various Organs As Determined By Use Of The 'Indicator Diffusion' Method.* Acta Physiol Scand, 1963. **58**: p. 292-305.
48. Kety, S.S., *The theory and applications of the exchange of inert gas at the lungs and tissues.* Pharmacol Rev, 1951. **3**(1): p. 1-41.
49. Renkin, E.M., *Transport of potassium-42 from blood to tissue in isolated mammalian skeletal muscles.* Am J Physiol, 1959. **197**: p. 1205-10.
50. Sha'afi, R.I., *Permeability for water and other polar molecules*, in *Membrane transport*, S.L. Bonting and J.J.H.H.M. de Pont, Editors. 1981, Elsevier / North Holland Biomedical Press: Amsterdam. p. 29-60.
51. Mitchell, D.G., *MR imaging contrast agents--what's in a name?* J Magn Reson Imaging, 1997. **7**(1): p. 1-4.
52. Tofts, P.S. and Kermode, A.G., *Measurement of the blood-brain barrier permeability and leakage space using dynamic MR imaging. 1. Fundamental concepts.* Magn Reson Med, 1991. **17**(2): p. 357-67.
53. Brix, G., Semmler, W., Port, R., Schad, L.R., Layer, G., and Lorenz, W.J., *Pharmacokinetic parameters in CNS Gd-DTPA enhanced MR imaging.* J Comput Assist Tomogr, 1991. **15**(4): p. 621-8.
54. Larsson, H.B., Stubgaard, M., Frederiksen, J.L., Jensen, M., Henriksen, O., and Paulson, O.B., *Quantitation of blood-brain barrier defect by magnetic resonance imaging and gadolinium-DTPA in patients with multiple sclerosis and brain tumors.* Magn Reson Med, 1990. **16**(1): p. 117-31.
55. Tofts, P.S., *Modeling tracer kinetics in dynamic Gd-DTPA MR imaging.* J Magn Reson Imaging, 1997. **7**(1): p. 91-101.
56. Weinmann, H.J., Laniado, M., and Mutzel, W., *Pharmacokinetics of GdDTPA/dimeglumine after intravenous injection into healthy volunteers.* Physiol Chem Phys Med NMR, 1984. **16**(2): p. 167-72.
57. Su, M.Y., Jao, J.C., and Nalcioglu, O., *Measurement of vascular volume fraction and blood-tissue permeability constants with a pharmacokinetic model: studies in*

rat muscle tumors with dynamic Gd-DTPA enhanced MRI. Magn Reson Med, 1994. **32**(6): p. 714-24.

58. Degani, H., Gusis, V., Weinstein, D., Fields, S., and Strano, S., *Mapping pathophysiological features of breast tumors by MRI at high spatial resolution.* Nat Med, 1997. **3**(7): p. 780-2.
59. Fritz-Hansen, T., Rostrup, E., Sondergaard, L., Ring, P.B., Amtorp, O., and Larsson, H.B., *Capillary transfer constant of Gd-DTPA in the myocardium at rest and during vasodilation assessed by MRI.* Magn Reson Med, 1998. **40**(6): p. 922-9.
60. Daldrup, H.E., Shames, D.M., Husseini, W., Wendland, M.F., Okuhata, Y., and Brasch, R.C., *Quantification of the extraction fraction for gadopentetate across breast cancer capillaries.* Magn Reson Med, 1998. **40**(4): p. 537-43.
61. Henderson, E., Rutt, B.K., and Lee, T.Y., *Temporal sampling requirements for the tracer kinetics modeling of breast disease.* Magn Reson Imaging, 1998. **16**(9): p. 1057-73.
62. Parker, G.J.M., *PhD Thesis: Monitoring contrast agent kinetics using dynamic MRI: Quantitative and qualitative analysis*, in *Institute of Cancer Research.* 1997, University of London: London.
63. Vonken, E.P., van Osch, M.J., Bakker, C.J., and Viergever, M.A., *Simultaneous quantitative cerebral perfusion and Gd-DTPA extravasation measurement with dual-echo dynamic susceptibility contrast MRI.* Magn Reson Med, 2000. **43**(6): p. 820-7.
64. Patlak, C.S., Blasberg, R.G., and Fenstermacher, J.D., *Graphical evaluation of blood-to-brain transfer constants from multiple-time uptake data.* J Cereb Blood Flow Metab, 1983. **3**(1): p. 1-7.
65. Jackson, A., Haroon, H., Zhu, X.P., Li, K.L., Thacker, N.A., and Jayson, G., *Breath-hold perfusion and permeability mapping of hepatic malignancies using magnetic resonance imaging and a first-pass leakage profile model.* NMR Biomed, 2002. **15**(2): p. 164-73.
66. Li, K.L., Zhu, X.P., Checkley, D.R., Tessier, J.J., Hillier, V.F., Waterton, J.C., and Jackson, A., *Simultaneous mapping of blood volume and endothelial permeability surface area product in gliomas using iterative analysis of first-pass dynamic contrast enhanced MRI data.* Br J Radiol, 2003. **76**(901): p. 39-50.
67. Roberts, T.P., *Physiologic measurements by contrast-enhanced MR imaging: expectations and limitations.* J Magn Reson Imaging, 1997. **7**(1): p. 82-90.
68. Tofts, P.S., Berkowitz, B., and Schnall, M.D., *Quantitative analysis of dynamic Gd-DTPA enhancement in breast tumors using a permeability model.* Magn Reson Med, 1995. **33**(4): p. 564-8.
69. Parker, G.J.M., Tanner, S.F., and Leach, M.O. *Pitfalls in the measurement of tissue permeability over short time-scales using multi-compartment models with a low temporal resolution blood input function.* in *Proc Intl Soc Magn Reson Med.* 1996. New York, New York, USA.
70. Haroon, H.A., Buckley, D.L., Patankar, T.A., Dow, G.R., Rutherford, S.A., Baleriaux, D., and Jackson, A., *A comparison of K^{trans} measurements obtained with conventional and first pass pharmacokinetic models in human gliomas.* J Magn Reson Imaging, 2004. **19**(5): p. 527-36.
71. Yamagishi, S., Okamoto, T., Amano, S., and Inagaki, Y., *Can we identify novel angiogenesis inhibitors from cultured embryonic cells?* Med Hypoth, 2003. **60**(3): p. 389-90.
72. Behzadian, M.A., Windsor, L.J., Ghaly, N., Liou, G., Tsai, N.T., and Caldwell, R.B., *VEGF-induced paracellular permeability in cultured endothelial cells involves urokinase and its receptor.* FASEB J, 2003. **17**(6): p. 752-4.

73. Buckley, D.L., *Uncertainty in the analysis of tracer kinetics using dynamic contrast-enhanced T1-weighted MRI.* Magn Reson Med, 2002. **47**(3): p. 601-6.
74. Li, K.L., Zhu, X.P., Waterton, J.C., Checkley, D., Tessier, J.J.L., Watson, Y., and Jackson, A. *Improving estimates of endothelial permeability surface area product using constrained fitting parameters for the estimation of the plasma tracer concentration function (PTCF).* in *Proc Intl Soc Magn Reson Med*. 2000. Denver, Colorado, USA.
75. Fritz-Hansen, T., Rostrup, E., Larsson, H.B., Sondergaard, L., Ring, P., and Henriksen, O., *Measurement of the arterial concentration of Gd-DTPA using MRI: a step toward quantitative perfusion imaging.* Magn Reson Med, 1996. **36**(2): p. 225-31.
76. Li, K. and Jackson, A., *New hybrid technique for accurate and reproducible quantitatation of dynamic contrast-enhanced MRI data.* Magn Reson Med, 2003. **50**(6): p. 1286-95.
77. Jayson, G.C., Zweit, J., Jackson, A., Mulatero, C., Julyan, P., Ranson, M., Broughton, L., Wagstaff, J., Hakannson, L., Groenewegen, G., Bailey, J., Smith, N., Hastings, D., Lawrance, J., Haroon, H., Ward, T., McGown, A.T., Tang, M., Levitt, D., Marreaud, S., Lehmann, F.F., Herold, M., and Zwierzina, H., *Molecular imaging and biological evaluation of HuMV833 anti-VEGF antibody: implications for trial design of antiangiogenic antibodies.* J Natl Cancer Inst, 2002. **94**(19): p. 1484-93.
78. Jackson, A., Jayson, G.C., Li, K.L., Zhu, X.P., Checkley, D.R., Tessier, J.J., and Waterton, J.C., *Reproducibility of quantitative dynamic contrast-enhanced MRI in newly presenting glioma.* Br J Radiol, 2003. **76**(903): p. 153-62.
79. Harrer, J.U., Parker, G.J., Haroon, H.A., Buckley, D.L., Embelton, K., Roberts, C., Baleriaux, D., and Jackson, A., *Comparative study of methods for determining vascular permeability and blood volume in human gliomas.* J Magn Reson Imaging, 2004. **20**(5): p. 748-57.
80. Shin, J.H., Lee, H.K., Kwun, B.D., Kim, J.S., Kang, W., Choi, C.G., and Suh, D.C., *Using relative cerebral blood flow and volume to evaluate the histopathologic grade of cerebral gliomas: preliminary results.* AJR Am J Roentgenol, 2002. **179**(3): p. 783-9.
81. Ludemann, L., Grieger, W., Wurm, R., Budzisch, M., Hamm, B., and Zimmer, C., *Comparison of dynamic contrast-enhanced MRI with WHO tumor grading for gliomas.* Eur Radiol, 2001. **11**(7): p. 1231-41.
82. Law, M., Yang, S., Wang, H., Babb, J.S., Johnson, G., Cha, S., Knopp, E.A., and Zagzag, D., *Glioma grading: sensitivity, specificity, and predictive values of perfusion MR imaging and proton MR spectroscopic imaging compared with conventional MR imaging.* AJNR Am J Neuroradiol, 2003. **24**(10): p. 1989-98.
83. Law, M., Cha, S., Knopp, E.A., Johnson, G., Arnett, J., and Litt, A.W., *High-grade gliomas and solitary metastases: differentiation by using perfusion and proton spectroscopic MR imaging.* Radiology, 2002. **222**(3): p. 715-21.
84. Knopp, E.A., Cha, S., Johnson, G., Mazumdar, A., Golfinos, J.G., Zagzag, D., Miller, D.C., Kelly, P.J., and Kricheff, II, *Glial neoplasms: dynamic contrast-enhanced T2*-weighted MR imaging.* Radiology, 1999. **211**(3): p. 791-8.
85. Fuss, M., Wenz, F., Essig, M., Muenter, M., Debus, J., Herman, T.S., and Wannenmacher, M., *Tumor angiogenesis of low-grade astrocytomas measured by dynamic susceptibility contrast-enhanced MRI (DSC-MRI) is predictive of local tumor control after radiation therapy.* Int J Radiat Oncol Biol Phys, 2001. **51**(2): p. 478-82.
86. Aronen, H.J. and Perkio, J., *Dynamic susceptibility contrast MRI of gliomas.* Neuroimaging Clin N Am, 2002. **12**(4): p. 501-23.

87. Aronen, H.J., Gazit, I.E., Louis, D.N., Buchbinder, B.R., Pardo, F.S., Weisskoff, R.M., Harsh, G.R., Cosgrove, G.R., Halpern, E.F., Hochberg, F.H., and et al., *Cerebral blood volume maps of gliomas: comparison with tumor grade and histologic findings.* Radiology, 1994. **191**(1): p. 41-51.

88. Provenzale, J.M., Wang, G.R., Brenner, T., Petrella, J.R., and Sorensen, A.G., *Comparison of permeability in high-grade and low-grade brain tumors using dynamic susceptibility contrast MR imaging.* AJR Am J Roentgenol, 2002. **178**(3): p. 711-6.

89. Roberts, H.C., Roberts, T.P., Brasch, R.C., and Dillon, W.P., *Quantitative measurement of microvascular permeability in human brain tumors achieved using dynamic contrast-enhanced MR imaging: correlation with histologic grade.* AJNR Am J Neuroradiol, 2000. **21**(5): p. 891-9.

90. Sugahara, T., Korogi, Y., Kochi, M., Ikushima, I., Hirai, T., Okuda, T., Shigematsu, Y., Liang, L., Ge, Y., Ushio, Y., and Takahashi, M., *Correlation of MR imaging-determined cerebral blood volume maps with histologic and angiographic determination of vascularity of gliomas.* AJR Am J Roentgenol, 1998. **171**(6): p. 1479-86.

91. Croteau, D., Scarpace, L., Hearshen, D., Gutierrez, J., Fisher, J.L., Rock, J.P., and Mikkelsen, T., *Correlation between magnetic resonance spectroscopy imaging and image-guided biopsies: semiquantitative and qualitative histopathological analyses of patients with untreated glioma.* Neurosurgery, 2001. **49**(4): p. 823-9.

92. Wong, E.T., Jackson, E.F., Hess, K.R., Schomer, D.F., Hazle, J.D., Kyritsis, A.P., Jaeckle, K.A., Yung, W.K., Levin, V.A., and Leeds, N.E., *Correlation between dynamic MRI and outcome in patients with malignant gliomas.* Neurology, 1998. **50**(3): p. 777-81.

93. Wong, J.C., Provenzale, J.M., and Petrella, J.R., *Perfusion MR imaging of brain neoplasms.* AJR Am J Roentgenol, 2000. **174**(4): p. 1147-57.

94. Cha, S., Knopp, E.A., Johnson, G., Wetzel, S.G., Litt, A.W., and Zagzag, D., *Intracranial mass lesions: dynamic contrast-enhanced susceptibility-weighted echo-planar perfusion MR imaging.* Radiology, 2002. **223**(1): p. 11-29.

95. Lev, M.H. and Rosen, B.R., *Clinical applications of intracranial perfusion MR imaging.* Neuroimaging Clin N Am, 1999. **9**(2): p. 309-31.

96. Petrella, J.R. and Provenzale, J.M., *MR perfusion imaging of the brain: techniques and applications.* AJR Am J Roentgenol, 2000. **175**(1): p. 207-19.

97. Aronen, H.J., Pardo, F.S., Kennedy, D.N., Belliveau, J.W., Packard, S.D., Hsu, D.W., Hochberg, F.H., Fischman, A.J., and Rosen, B.R., *High microvascular blood volume is associated with high glucose uptake and tumor angiogenesis in human gliomas.* Clin Cancer Res, 2000. **6**(6): p. 2189-200.

98. Lev, M.H., Ozsunar, Y., Henson, J.W., Rasheed, A.A., Barest, G.D., Harsh, G.R.t., Fitzek, M.M., Chiocca, E.A., Rabinov, J.D., Csavoy, A.N., Rosen, B.R., Hochberg, F.H., Schaefer, P.W., and Gonzalez, R.G., *Glial tumor grading and outcome prediction using dynamic spin-echo MR susceptibility mapping compared with conventional contrast-enhanced MR: confounding effect of elevated rCBV of oligodendrogliomas [corrected].* AJNR Am J Neuroradiol, 2004. **25**(2): p. 214-21.

99. Johnson, G., Wetzel, S.G., Cha, S., Babb, J., and Tofts, P.S., *Measuring blood volume and vascular transfer constant from dynamic, T(2)*-weighted contrast-enhanced MRI.* Magn Reson Med, 2004. **51**(5): p. 961-8.

100. Weisskoff, R., Boxermann, J., Sorensen, A., Kulke, S., Campbell, T., and Rosen, B. *Simultaneous blood volume and permeability mapping using a single Gd-based contrast injection.* in *Proc Intl Soc Magn Reson Med.* 1994. Berkley, California, USA.

101. Nasel, C. and Schindler, E., *[Xenon-CT and perfusion MRI in the diagnosis of cerebral gliomas]*. Radiologe, 1998. **38**(11): p. 930-4.

102. Nakagawa, T., Tanaka, R., Takeuchi, S., and Takeda, N., *Haemodynamic evaluation of cerebral gliomas using XeCT.* Acta Neurochir (Wien), 1998. **140**(3): p. 223-33; discussion 233-4.

103. van Dijke, C.F., Brasch, R.C., Roberts, T.P., Weidner, N., Mathur, A., Shames, D.M., Mann, J.S., Demsar, F., Lang, P., and Schwickert, H.C., *Mammary carcinoma model: correlation of macromolecular contrast-enhanced MR imaging characterizations of tumor microvasculature and histologic capillary density.* Radiology, 1996. **198**(3): p. 813-8.

104. Schwickert, H.C., Stiskal, M., Roberts, T.P., van Dijke, C.F., Mann, J., Muhler, A., Shames, D.M., Demsar, F., Disston, A., and Brasch, R.C., *Contrast-enhanced MR imaging assessment of tumor capillary permeability: effect of irradiation on delivery of chemotherapy.* Radiology, 1996. **198**(3): p. 893-8.

105. Dvorak, H.F., Detmar, M., Claffey, K.P., Nagy, J.A., van de Water, L., and Senger, D.R., *Vascular permeability factor/vascular endothelial growth factor: an important mediator of angiogenesis in malignancy and inflammation.* Int Arch Allergy Immunol, 1995. **107**(1-3): p. 233-5.

106. Law, M., Yang, S., Babb, J.S., Knopp, E.A., Golfinos, J.G., Zagzag, D., and Johnson, G., *Comparison of cerebral blood volume and vascular permeability from dynamic susceptibility contrast-enhanced perfusion MR imaging with glioma grade.* AJNR Am J Neuroradiol, 2004. **25**(5): p. 746-55.

107. Tabachnick, B. and Fidell, L., *Using multivariate statistics*. 1996, New York: Harper Collins College Publishers.

108. Ewing, J.R., Knight, R.A., Nagaraja, T.N., Yee, J.S., Nagesh, V., Whitton, P.A., Li, L., and Fenstermacher, J.D., *Patlak plots of Gd-DTPA MRI data yield blood-brain transfer constants concordant with those of 14C-sucrose in areas of blood-brain opening.* Magn Reson Med, 2003. **50**(2): p. 283-92.

109. Jackson, A., Kassner, A., Annesley-Williams, D., Reid, H., Zhu, X.P., and Li, K.L., *Abnormalities in the recirculation phase of contrast agent bolus passage in cerebral gliomas: comparison with relative blood volume and tumor grade.* AJNR Am J Neuroradiol, 2002. **23**(1): p. 7-14.

110. Sugahara, T., Korogi, Y., Kochi, M., Ushio, Y., and Takahashi, M., *Perfusion-sensitive MR imaging of gliomas: comparison between gradient-echo and spin-echo echo-planar imaging techniques.* AJNR Am J Neuroradiol, 2001. **22**(7): p. 1306-15.

111. Ludemann, L., Hamm, B., and Zimmer, C., *Pharmacokinetic analysis of glioma compartments with dynamic Gd-DTPA-enhanced magnetic resonance imaging.* Magn Reson Imaging, 2000. **18**(10): p. 1201-14.

112. Kassner, A., Annesley, D.J., Zhu, X.P., Li, K.L., Kamaly-Asl, I.D., Watson, Y., and Jackson, A., *Abnormalities of the contrast re-circulation phase in cerebral tumors demonstrated using dynamic susceptibility contrast-enhanced imaging: a possible marker of vascular tortuosity.* J Magn Reson Imaging, 2000. **11**(2): p. 103-13.

113. Jackson, A., Kassner, A., Zhu, X.P., and Li, K.L., *Reproducibility of T2* blood volume and vascular tortuosity maps in cerebral gliomas.* J Magn Reson Imaging, 2001. **14**(5): p. 510-6.

114. Bruening, R., Kwong, K.K., Vevea, M.J., Hochberg, F.H., Cher, L., Harsh, G.R.t., Niemi, P.T., Weisskoff, R.M., and Rosen, B.R., *Echo-planar MR determination of relative cerebral blood volume in human brain tumors: T1 versus T2 weighting.* AJNR Am J Neuroradiol, 1996. **17**(5): p. 831-40.

115. Hacklander, T., Hofer, M., Reichenbach, J.R., Rascher, K., Furst, G., and Modder, U., *Cerebral blood volume maps with dynamic contrast-enhanced T1-weighted*

FLASH imaging: normal values and preliminary clinical results. J Comput Assist Tomogr, 1996. **20**(4): p. 532-9.

116. Shweiki, D., Neeman, M., Itin, A., and Keshet, E., *Induction of vascular endothelial growth factor expression by hypoxia and by glucose deficiency in multicell spheroids: implications for tumor angiogenesis.* Proc Natl Acad Sci U S A, 1995. **92**(3): p. 768-72.
117. Plate, K.H. and Risau, W., *Angiogenesis in malignant gliomas.* Glia, 1995. **15**(3): p. 339-47.
118. Brasch, R. and Turetschek, K., *MRI characterization of tumors and grading angiogenesis using macromolecular contrast media: status report.* Eur J Radiol, 2000. **34**(3): p. 148-55.
119. Padhani, A.R., *Dynamic contrast-enhanced MRI in clinical oncology: current status and future directions.* J Magn Reson Imaging, 2002. **16**(4): p. 407-22.
120. Sugahara, T., Korogi, Y., Shigematsu, Y., Liang, L., Yoshizumi, K., Kitajima, M., and Takahashi, M., *Value of dynamic susceptibility contrast magnetic resonance imaging in the evaluation of intracranial tumors.* Top Magn Reson Imaging, 1999. **10**(2): p. 114-24.
121. Cha, S., Pierce, S., Knopp, E.A., Johnson, G., Yang, C., Ton, A., Litt, A.W., and Zagzag, D., *Dynamic contrast-enhanced T2*-weighted MR imaging of tumefactive demyelinating lesions.* AJNR Am J Neuroradiol, 2001. **22**(6): p. 1109-16.
122. Miyati, T., Banno, T., Mase, M., Kasai, H., Shundo, H., Imazawa, M., and Ohba, S., *Dual dynamic contrast-enhanced MR imaging.* J Magn Reson Imaging, 1997. **7**(1): p. 230-5.
123. Uematsu, H., Maeda, M., Sadato, N., Matsuda, T., Ishimori, Y., Koshimoto, Y., Yamada, H., Kimura, H., Kawamura, Y., Hayashi, N., Yonekura, Y., and Ishii, Y., *Vascular permeability: quantitative measurement with double-echo dynamic MR imaging--theory and clinical application.* Radiology, 2000. **214**(3): p. 912-7.
124. Johnson, G., Wetzel, S., Cha, S., and Tofts, P.S. *Simultaneous Measurement of Blood Volume and Vascular Transfer Constant by First Pass Pharmacokinetic Modelling*. in *Proc Intl Soc Magn Reson Med*. 2002. Honolulu, Hawai'i, USA.
125. Rosen, B.R., Belliveau, J.W., Aronen, H.J., Kennedy, D., Buchbinder, B.R., Fischman, A., Gruber, M., Glas, J., Weisskoff, R.M., Cohen, M.S., and et al., *Susceptibility contrast imaging of cerebral blood volume: human experience.* Magn Reson Med, 1991. **22**(2): p. 293-9; discussion 300-3.
126. Maeda, M., Itoh, S., Kimura, H., Iwasaki, T., Hayashi, N., Yamamoto, K., Ishii, Y., and Kubota, T., *Tumor vascularity in the brain: evaluation with dynamic susceptibility-contrast MR imaging.* Radiology, 1993. **189**(1): p. 233-8.
127. Wetzel, S.G., Cha, S., Law, M., Johnson, G., Golfinos, J., Lee, P., and Nelson, P.K., *Preoperative assessment of intracranial tumors with perfusion MR and a volumetric interpolated examination: a comparative study with DSA.* AJNR Am J Neuroradiol, 2002. **23**(10): p. 1767-74.
128. Barbier, E.L., Lamalle, L., and Decorps, M., *Methodology of brain perfusion imaging.* J Magn Reson Imaging, 2001. **13**(4): p. 496-520.
129. Aronen, H.J., Glass, J., Pardo, F.S., Belliveau, J.W., Gruber, M.L., Buchbinder, B.R., Gazit, I.E., Linggood, R.M., Fischman, A.J., Rosen, B.R., and et al., *Echo-planar MR cerebral blood volume mapping of gliomas. Clinical utility.* Acta Radiol, 1995. **36**(5): p. 520-8.
130. Hacklander, T., *Parametric images of cerebral blood volume with T1 FLASH sequences (German).* Rontgenpraxis, 1995. **48**(5): p. 146-52.
131. Hacklander, T., Reichenbach, J.R., Hofer, M., and Modder, U., *Measurement of cerebral blood volume via the relaxing effect of low-dose gadopentetate dimeglumine during bolus transit.* AJNR Am J Neuroradiol, 1996. **17**(5): p. 821-30.

132. Hacklander, T., Reichenbach, J.R., and Modder, U., *Comparison of cerebral blood volume measurements using the T1 and T2* methods in normal human brains and brain tumors.* J Comput Assist Tomogr, 1997. **21**(6): p. 857-66.

133. Schaefer, P.W., Hunter, G.J., He, J., Hamberg, L.M., Sorensen, A.G., Schwamm, L.H., Koroshetz, W.J., and Gonzalez, R.G., *Predicting cerebral ischemic infarct volume with diffusion and perfusion MR imaging.* AJNR Am J Neuroradiol, 2002. **23**(10): p. 1785-94.

134. Kim, J.H., Lee, E.J., Lee, S.J., Choi, N.C., Lim, B.H., and Shin, T., *Comparative evaluation of cerebral blood volume and cerebral blood flow in acute ischemic stroke by using perfusion-weighted MR imaging and SPECT.* Acta Radiol, 2002. **43**(4): p. 365-70.

135. Helenius, J., Perkio, J., Soinne, L., L, O.S., Carano, R.A., Salonen, O., Savolainen, S., Kaste, M., Aronen, H.J., and Tatlisumak, T., *Cerebral Hemodynamics in a Healthy Population Measured by Dynamic Susceptibility Contrast Mr Imaging.* Acta Radiol, 2003. **44**(5): p. 538-546.

136. Liu, G., Sobering, G., Duyn, J., and Moonen, C.T., *A functional MRI technique combining principles of echo-shifting with a train of observations (PRESTO).* Magn Reson Med, 1993. **30**(6): p. 764-8.

137. Thacker, N.A., Scott, M.L., and Jackson, A., *Can dynamic susceptibility contrast magnetic resonance imaging perfusion data be analyzed using a model based on directional flow?* J Magn Reson Imaging, 2003. **17**(2): p. 241-55.

138. Bicknell, R., Lewis, C.E., and Ferrara, N., *Introduction*, in *Tumour Angiogenesis*. 1997, Oxford University Press: Oxford. p. 15.

139. Brasch, R., Pham, C., Shames, D., Roberts, T., van Dijke, K., van Bruggen, N., Mann, J., Ostrowitzki, S., and Melnyk, O., *Assessing tumor angiogenesis using macromolecular MR imaging contrast media.* J Magn Reson Imaging, 1997. **7**(1): p. 68-74.

140. Delorme, S. and Knopp, M.V., *Non-invasive vascular imaging: assessing tumour vascularity.* Eur Radiol, 1998. **8**(4): p. 517-27.

141. Lund, E.L., Spang-Thomsen, M., Skovgaard-Poulsen, H., and Kristjansen, P.E., *Tumor angiogenesis--a new therapeutic target in gliomas.* Acta Neurol Scand, 1998. **97**(1): p. 52-62.

142. Winlaw, D.S., *Angiogenesis in the pathobiology and treatment of vascular and malignant diseases.* Ann Thorac Surg, 1997. **64**(4): p. 1204-11.

143. Mergo, P.J., Engelken, J.D., Helmberger, T., and Ros, P.R., *MRI in focal liver disease: a comparison of small and ultra-small superparamagnetic iron oxide as hepatic contrast agents.* J Magn Reson Imaging, 1998. **8**(5): p. 1073-8.

144. Seneterre, E., Taourel, P., Bouvier, Y., Pradel, J., Van Beers, B., Daures, J.P., Pringot, J., Mathieu, D., and Bruel, J.M., *Detection of hepatic metastases: ferumoxides-enhanced MR imaging versus unenhanced MR imaging and CT during arterial portography.* Radiology, 1996. **200**(3): p. 785-92.

145. Scharf, J., Zapletal, C., Hess, T., Hoffmann, U., Mehrabi, A., Mihm, D., Hoffmann, V., Brix, G., Kraus, T., Richter, G.M., and Klar, E., *Assessment of hepatic perfusion in pigs by pharmacokinetic analysis of dynamic MR images.* J Magn Reson Imaging, 1999. **9**(4): p. 568-72.

146. Foley, W.D., Mallisee, T.A., Hohenwalter, M.D., Wilson, C.R., Quiroz, F.A., and Taylor, A.J., *Multiphase hepatic CT with a multirow detector CT scanner.* AJR Am J Roentgenol, 2000. **175**(3): p. 679-85.

147. Thacker, N.A., Jackson, A., Moriarty, D., and Vokurka, E., *Improved quality of re-sliced MR images using re-normalized sinc interpolation.* J Magn Reson Imaging, 1999. **10**(4): p. 582-8.

148. Nie, N.H. and Hull, C.H., in *SPSS update 7-9*. 1981, McGraw-Hill: New York. p. 234-5.
149. Bland, J.M. and Altman, D.G., *Measurement error and correlation coefficients.* BMJ, 1996. **313**(7048): p. 41-2.
150. Wastell, D.G. and Barker, G.R., *Intraclass correlations: A two-facet case study and some comments on the concept of reliability.* Bulletin of the Psychonometric Society, 1988. **26**(6): p. 583-6.
151. Brix, G., Bahner, M.L., Hoffmann, U., Horvath, A., and Schreiber, W., *Regional blood flow, capillary permeability, and compartmental volumes: measurement with dynamic CT--initial experience.* Radiology, 1999. **210**(1): p. 269-76.
152. Hawighorst, H., Knapstein, P.G., Knopp, M.V., Weikel, W., Brix, G., Zuna, I., Schonberg, S.O., Essig, M., Vaupel, P., and van Kaick, G., *Uterine cervical carcinoma: comparison of standard and pharmacokinetic analysis of time-intensity curves for assessment of tumor angiogenesis and patient survival.* Cancer Res, 1998. **58**(16): p. 3598-602.
153. Taylor, J.S., Tofts, P.S., Port, R., Evelhoch, J.L., Knopp, M., Reddick, W.E., Runge, V.M., and Mayr, N., *MR imaging of tumor microcirculation: promise for the new millennium.* J Magn Reson Imaging, 1999. **10**(6): p. 903-7.
154. Diesbourg, L.D., Prato, F.S., Wisenberg, G., Drost, D.J., Marshall, T.P., Carroll, S.E., and O'Neill, B., *Quantification of myocardial blood flow and extracellular volumes using a bolus injection of Gd-DTPA: kinetic modeling in canine ischemic disease.* Magn Reson Med, 1992. **23**(2): p. 239-53.
155. Tong, C.Y., Prato, F.S., Wisenberg, G., Lee, T.Y., Carroll, E., Sandler, D., Wills, J., and Drost, D., *Measurement of the extraction efficiency and distribution volume for Gd-DTPA in normal and diseased canine myocardium.* Magn Reson Med, 1993. **30**(3): p. 337-46.
156. Ellinger, R., et al. *The impact of the arterial input function (AIF) on quantitative evaluation of dynamic susceptibility contrast enhanced MR studies.* in *Proc Intl Soc Magn Reson Med*. 1997. Vancouver, British Columbia, Canada.
157. Parker, G.J.M., Tanner, S., and Leach, M. *Pitfalls in the measurement of tissue permeability over short time-scales using a low temporal resolution blood input function.* in *Proc Intl Soc Magn Reson Med*. 1998. Sydney, Australia.
158. Zhu, X.P., et al. *3D T_1 mapping by means of fast field echno technique.* in *Proc Intl Soc Magn Reson Med*. 1999. Philadelphia, Pennsylvania, USA.
159. Dempster, A., Laird, N.M., and Rubin, D., *Maximum likelihood from incomplete data via the EM algorithm.* J Roy Stat Soc, 1977. **B39**(1): p. 1-38.
160. Neufeld, G., Cohen, T., Gengrinovitch, S., and Poltorak, Z., *Vascular endothelial growth factor (VEGF) and its receptors.* FASEB J, 1999. **13**(1): p. 9-22.
161. Gordon, M.S., Margolin, K., Talpaz, M., Sledge, G.W., Jr., Holmgren, E., Benjamin, R., Stalter, S., Shak, S., and Adelman, D., *Phase I safety and pharmacokinetic study of recombinant human anti-vascular endothelial growth factor in patients with advanced cancer.* J Clin Oncol, 2001. **19**(3): p. 843-50.
162. Margolin, K., Gordon, M.S., Holmgren, E., Gaudreault, J., Novotny, W., Fyfe, G., Adelman, D., Stalter, S., and Breed, J., *Phase Ib trial of intravenous recombinant humanized monoclonal antibody to vascular endothelial growth factor in combination with chemotherapy in patients with advanced cancer: pharmacologic and long-term safety data.* J Clin Oncol, 2001. **19**(3): p. 851-6.
163. Asano, M., Yukita, A., and Suzuki, H., *Wide spectrum of antitumor activity of a neutralizing monoclonal antibody to human vascular endothelial growth factor.* Jpn J Cancer Res, 1999. **90**(1): p. 93-100.
164. Herbst, R.S., Hess, K.R., Tran, H.T., Tseng, J.E., Mullani, N.A., Charnsangavej, C., Madden, T., Davis, D.W., McConkey, D.J., O'Reilly, M.S., Ellis, L.M., Pluda, J.,

Hong, W.K., and Abbruzzese, J.L., *Phase I study of recombinant human endostatin in patients with advanced solid tumors.* J Clin Oncol, 2002. **20**(18): p. 3792-803.

165. Gruber, B.L., Marchese, M.J., and Kew, R., *Angiogenic factors stimulate mast-cell migration.* Blood, 1995. **86**(7): p. 2488-93.

166. Morgan, B., Thomas, A.L., Drevs, J., Hennig, J., Buchert, M., Jivan, A., Horsfield, M.A., Mross, K., Ball, H.A., Lee, L., Mietlowski, W., Fuxuis, S., Unger, C., O'Byrne, K., Henry, A., Cherryman, G.R., Laurent, D., Dugan, M., Marme, D., and Steward, W.P., *Dynamic contrast-enhanced magnetic resonance imaging as a biomarker for the pharmacological response of PTK787/ZK 222584, an inhibitor of the vascular endothelial growth factor receptor tyrosine kinases, in patients with advanced colorectal cancer and liver metastases: results from two phase I studies.* J Clin Oncol, 2003. **21**(21): p. 3955-64. Epub 2003 Sep 29.

167. Thomas, A.L., Morgan, B., Drevs, J., Unger, C., Wiedenmann, B., Vanhoefer, U., Laurent, D., Dugan, M., and Steward, W.P., *Vascular endothelial growth factor receptor tyrosine kinase inhibitors: PTK787/ZK 222584.* Semin Oncol, 2003. **30**(3 Suppl 6): p. 32-8.

168. Xiong, H.Q., Herbst, R., Faria, S.C., Scholz, C., Davis, D., Jackson, E.F., Madden, T., McConkey, D., Hicks, M., Hess, K., Charnsangavej, C.A., and Abbruzzese, J.L., *A phase I surrogate endpoint study of SU6668 in patients with solid tumors.* Invest New Drugs, 2004. **22**(4): p. 459-66.

169. Buckley, D.L., Haroon, H.A., and Jackson, A. *Blood Flow, Blood Volume and Microvascular Permeability in Cerebral Gliomas*. in *Proc Intl Soc Magn Reson Med Workshop on In Vivo Functional and Molecular Assessment of Cancer*. 2002. Santa Cruz, California, USA.

170. van Laarhoven, H.W., Rijpkema, M., Punt, C.J., Ruers, T.J., Hendriks, J.C., Barentsz, J.O., and Heerschap, A., *Method for quantitation of dynamic MRI contrast agent uptake in colorectal liver metastases.* J Magn Reson Imaging, 2003. **18**(3): p. 315-20.

171. Nakashige, A., Horiguchi, J., Tamura, A., Asahara, T., Shimamoto, F., and Ito, K., *Quantitative measurement of hepatic portal perfusion by multidetector row CT with compensation for respiratory misregistration.* Br J Radiol, 2004. **77**(921): p. 728-734.

172. Sobol, W.T. and Cure, J.K., *Can in vivo assessment of tissue hemodynamics with dynamic contrast-enhanced CT be used in the diagnosis of tumors and monitoring of cancer therapy outcomes?* Radiology, 2004. **232**(3): p. 631-2.

173. Dennis Cheong, L.H., Tchoyoson Lim, C.C., and Koh, T.S., *Dynamic contrast-enhanced CT of intracranial meningioma: comparison of distributed and compartmental tracer kinetic models--initial results.* Radiology, 2004. **232**(3): p. 921-30.

174. Yi, C.A., Lee, K.S., Kim, E.A., Han, J., Kim, H., Kwon, O.J., Jeong, Y.J., and Kim, S., *Solitary Pulmonary Nodules: Dynamic Enhanced Multi-Detector Row CT Study and Comparison with Vascular Endothelial Growth Factor and Microvessel Density*. Radiology, 2004.